

**Cavity Ring-down and Multi-Pass Spectroscopies for Methane Source
Attribution and Chemical Kinetics Studies**

Thesis by
Linhan Shen

In Partial Fulfillment of the Requirements for the degree of
Doctor of Philosophy



CALIFORNIA INSTITUTE OF TECHNOLOGY
Pasadena, California

2018
(Defended November 3rd 2017)

© 2017

Linhan Shen

ORCID: 0000-0003-3871-655X

All Rights Reserved

ACKNOWLEDGEMENTS

It has been a long but fun journey to get here. My years at Caltech has given me so much more than I ever hoped for. I have learnt so much from everybody I encountered during my time here. I could not have done this without the love, help, and support from my family, my friends, and my peers at Caltech. There is an old Chinese saying:

You rely on your parents at home, but have to rely on your friends when you are away.

I have been away from home for 10 years, since I started college in Montana. But everywhere I have been, I have been made at home, and for that I am eternally grateful.

Mitchio, I have learnt so much from you. Not only for the knowledge you have taught me, but also for your kindness and care for us. You are who I look up to as a great scientist. You taught me to have a critical mind, while having the utmost respect and appreciations for my peers and colleagues. You have joked that I should do as you say but not as you do. But what you do is what inspired me the most. You have taught me to be nice and kind to people around me no matter how stressful it is and how much pressure I am under.

My committee members, Geoff, Rudy, John, Lance, and Stan, you are who I look up to in my path and have given me all the guidance I could have hoped for. I have had the privilege of working directly with some of you and learnt from you. Your passion, enthusiasm, and dedication towards science and your work something I will keep close with me as the compass in my future journey.

My fellow Okumurons, you are not only my peers but also my friends. You are the ones there for me whenever I needed help at work for better for worse. Kana, Nathan, Matt, Aileen, Think, Leah, Kathryn, Laura, Matt, Lizzy, Luis, Gautam, Damien, Joey, Doug, Greg, and Nick,

thank you for all the discussions, group meetings, journal clubs, group camping trips, and random conversations I have ever had with all of you whether it is science related or not. Aileen, you taught me so much when I first started my graduate career. You taught me to be detail oriented and thorough. Most importantly, you reminded me to keep doing things I love outside of work. I would also like to give a special thanks to Think, who is my mentor and close friend. You have taught me most of the things I know in lab, gave me an option that changed my career when I had to decide what I wanted out of my graduate school career, and gave me honest critiques when I most needed them. Best of luck to your Texans. I have made a couple of very special friends from the Okumura group, Leah and Lizzy. The two of you have been very kind to me despite all of my flaws, shared long conversations with me about life in general, and carried me through hardships through my years here. Most importantly, you guys have opened your lovely families to me, from whom I have received love and care from your parents Bill, Joy, Tom, and Theresa. You and your families have accepted me as one of your own and have given me a sense of family away from my own, for that I am and always will be grateful to you.

Everybody I have worked with during my JPL days, Xu, Shuhui, Kyle, Mads, Yingdi, Fred, Brian, Keeyoon, and Fred, thanks for teaching me so many different aspects of atmospheric chemistry. I enjoyed the lunches, group meetings, and afternoon chats I have had with all of you. It was the best way anybody could have hoped to start their graduate school career.

All the undergraduate researchers I have worked with, Erin, Daniel, Jared, Karim, and Dan, it has been my pleasure working with all of you. The experience of working with you guys is what made me certain that I would like to pursue an academic career. Erin, you have inspired me so much and have become a great friend of mine ever since our time working together.

My collaborators, David, John, Sally, Patricia, Elle, and Victoria, you guys were the ones who made all of my research possible. Thanks for working with me and all your patience and encouragement towards me.

All the Caltech staff members, Mike, Steve, Rick, Joe, Steve, Elisa, Greg, Armando, Anne, Monica, Elisha, Nora, and Kathy, thank you so much for all of your help all these years. Mike, I have enjoyed all the conversations with you. Thank you for all you have taught me, my research would not have been possible without all of your great work.

Half of my graduate school career was supported by the NASA earth science and space fellowship (NESSF).

My friends, where do I even start? You guys are the ones who kept me sane and made these last 6 years fun and joyful. Thank you for doing everything I love with me, share the happiest moments of my life and yours with me, listen to my complaints and cries, and take care of me when I was unwell. Thank all of you: Minfeng, Kungyi, Ian, Lucas, Sunny, Katharine, Ada, Jin, Tung, Bassam, Karthik, and Anandh. My life would not have been whole without you.

Tim, you have been my advisor, my friend, and my family. You and Donna took me under your wings and believed in me when I was a 19-year-old girl coming to a strange country to study. You are the one who introduced me to the world of physical chemistry and have provided me guidance and help ever since. You made me take at least one English class every semester when I was in college, and told me that one day I would thank you for it. Today is that day. Thank you so much for all you have done for me. You are one of the reasons I got this far.

Finally, my dearest family, this thesis is for you. Thank you so much for your love, support, and everything a person could have ever wished for. Grandpa, you were the only one who had faith

in me and given me all the support when I decided to leave home to pursue my dream. You are who I wish I could become when I grow up. Mom and Dad, you are my anchor, my haven, and my destination. The ancient Chinese says that *you should not travel afar when your parents are still around*. I have been away from you for so long, for which I cannot apologize enough for. You made me who I am today. You gave me everything you can and everything I own, including your name, your knowledge, your support, and all the love in the world. The luckiest thing of my entire life is being your daughter. Thank you for making me who I am today. The best thing you have ever done for me was to provide me with the best education possible and give me the confidence and trust to make my own life decisions. I love you to the moon and back.

ABSTRACT

Methane is the most abundant hydrocarbon in the Earth atmosphere, is also an important greenhouse gas, energy source, and microbial metabolic energy source and product. With the rapid increase of atmospheric methane concentration, it has become very important to quantify methane emissions from different sources. This thesis describes the applications of cavity ring-down applications on atmospheric ethane measurements and measurements of doubly substituted methane for methane source attributions. We also present our work on chemical kinetics studies of an alkene ozonolysis intermediate, Criegee intermediate, using a multi-pass absorption technique.

In Chapter 2, we demonstrated the performance of a continuous-wave (cw) interband cascade laser (ICL) based mid-infrared cavity ring-down spectroscopy (CRDS) sensor for atmospheric ethane (C_2H_6) detection. A $3.36\ \mu\text{m}$ cw ICL with an was used to target two ethane absorption bands at $2976.788\ \text{cm}^{-1}$ and $2983.383\ \text{cm}^{-1}$. This technique utilizes the long effective pathlength ($\sim 4.5\ \text{km}$) of CRDS to increase sensitivity of atmospheric ethane detection. Our spectrometer can measure atmospheric ethane concentration as low as 200 pptv at standard temperature and pressure. We have used this instrument to measure the atmospheric ethane composition in ambient air collected in Pasadena, California. We have utilized this instrument to aid in the study of soil microbial response post the Porter Ranch gas leak. Results were shown in Chapter 3.

In Chapter 4, we demonstrate high sensitivity measurements of both $^{13}\text{CH}_3\text{D}$ and $^{12}\text{CH}_2\text{D}_2$ isotopologues using a high precision and high resolution spectroscopy technique, frequency stabilized cavity ring-down spectroscopy (FS-CRDS). Measurements of the abundances of doubly-substituted methane isotopologues ($^{13}\text{CH}_3\text{D}$ and $^{12}\text{CH}_2\text{D}_2$) are important in methane source attributions. Currently, methods developed for $^{13}\text{CH}_3\text{D}$ and $^{12}\text{CH}_2\text{D}_2$ measurements have been

mostly focused on the use of isotope ratio mass spectrometry (IRMS), which faces the challenges of mass resolutions. In this work, we focus on measuring these low abundant methane isotopologues optically, taking advantage of the distinct absorption features of them. This technique can be used as a potential complement to IRMS measurements for its ability to measure abundances of rare methane isotopologues with a short time average (~1 hour average per isotope ratio measurement). In Chapter 5, we utilized our IR kinetic spectroscopy (IRKS) apparatus to study the formation of HCO radicals from the smallest Criegee Intermediate (CH_2OO), which is an important intermediate from ozonolysis of the smallest alkene.

TABLE OF CONTENTS

Acknowledgements.....	iii
Abstract	vi
Table of Contents.....	ix
Chapter 1: Introduction: Atmospheric Methane and Its Chemistry	1
METHANE ON EARTH	2
METHANE ON MARS.....	3
METHANE SOURCE AND SINK ATTRIBUTION.....	5
REFERENCES	6
FIGURES	13
Chapter 2: Mid-Infrared Cavity Ring-down Spectroscopy Measurements of Atmospheric Ethane Abundance.....	17
ABSTRACT.....	18
INTRODUCTION	18
EXPERIMENTAL.....	21
RESULTS AND DISCUSSION	25
CONCLUSION.....	31
ACKNOWLEDGMENTS.....	31
REFERENCES	32
FIGURES AND TABLES.....	38
SUPPORTING INFORMATION	45
Chapter 3: Soil Microbial Response to A Massive Natural Gas Leak: Case Study of the Porter Ranch Gas Leak	69
ABSTRACT.....	70
INTRODUCTION	71
RESULTS AND DISCUSSION	73
MATERIALS AND METHODS	85
CONCLUSIONS AND BROADER CONEXT	91
REFERENCES	94
FIGURES AND TABLES.....	103
SUPPORTING INFORMATION	108
Chapter 4: Measurements of Doubly-Substituted Methane Isotopologues by Frequency Stabilized Mid-IR Cavity Ring-Down Spectroscopy	121
ABSTRACT.....	122
INTRODUCTION	123
METHODS	125
RESULTS AND DISCUSSION	128

CONCLUSION.....	133
ACKNOWLEDGMENTS.....	134
REFERENCES	134
FIGURES AND TABLES.....	140
SUPPORTING INFORMATION	146

Chapter 5: Infrared Kinetic Spectroscopy Studies on HO₂ Radicals Produced from Criegee Intermediate (CH₂OO)155

ABSTRACT.....	156
INTRODUCTION	157
METHODS	159
RESULTS AND DISCUSSION	161
CONCLUSION.....	164
REFERENCES	165
FIGURES AND TABLES.....	168

Chapter 1: Introduction: Atmospheric Methane and Its Chemistry

METHANE ON EARTH

Methane is the most abundant hydrocarbon in the Earth atmosphere, is also an important greenhouse gas, energy source, and microbial metabolic energy source and product.(Ferry, 1998; Hinrichs et al., 1999; Ramaswamy, 2001; Thauer, 1998; Wuebbles, 2002) Measurements of air trapped in the polar ice caps has proved evidence that there has been a significance increase in the atmospheric methane concentration over the last centuries. These ice core record revealed that present day average global methane concentration is the highest in the last 420,000 years and has increased for a factor of 2.5 since industrialization.(Etheridge et al., 1998; Petit et al., 1999) Atmospheric methane monitoring since 1983 has provided us more understanding of its dynamics. As we can see from Fig 1.1, the methane growth rate slowly decreased since the beginning of the direct monitoring of the atmosphere, until it reached a relative plateau in the early 2000 s. However, methane concentration has started increase rapidly since 2007 at more than 10 times the rate between 2000 and 2006.(Butler and Montzka, 2017; Dlugokencky et al., 2011; Saunio et al., 2016b) Despite its environmental and economic importance, much of the formation and destruction mechanisms remains poorly constrained. It was suggested that this recent rapid rise is mostly biogenics with smaller contributions from fossil fuel uses and wetland contributions.(Saunio et al., 2016b) This rapid change in the last decay calls for response in methane source identifications and possibilities of emission control.

Main sources of methane include biogenic (wetlands, lakes, agriculture, and landfills), thermogenic (oil and natural gas industries, and natural seeps), pyrogenic (biomass and biofuel burning) and abiotic (hydrates, geological) sources. Fig 1.2 shows the global methane budget in the decade of 2003 – 2012 reported based on sources and sinks.(Saunio et al., 2016a) Methane

sinks may also contribute in the rapid rise in the atmosphere. Compare to carbon dioxide, methane has a significantly shorter steady state lifetime (~ 9 years). The most important sinks of atmospheric methane are the oxidation by the hydroxyl radical (OH) and other radicals in the atmosphere, such as Cl and O(¹D), and methane consuming microbes, methanotrophy, in the soil. Tropospheric OH oxidation accounts for about 90% of the total methane sink.(Kirschke et al., 2013) Due to the strong temperature of the reaction with OH, as well as the global distribution of OH radicals, methane oxidation by OH mainly occurs in the lower to middle tropical troposphere during high sunlight.(Dlugokencky et al., 2011) Chlorine radicals also remove methane in the troposphere, but mostly in the marine boundary layer.(Allan et al., 2005; Allan et al., 2007; Platt et al., 2004)

METHANE ON MARS

Methane is not only an important trace gas on Earth atmosphere but also plays an important role in the atmosphere of other planets or moons in the solar system, especially on Mars. Studies on sources and sinks of methane on Mars can provide us important information on the planet's formation process, climate history, geological activities, and possibilities of life emerging on the planet. Recent *in situ* detection of methane on Mars by NASA's MSL Curiosity rover has raised important question about the sources and sinks of Martian methane.(Leshin et al., 2013; Webster et al., 2013; Webster et al., 2015) Figure 1. 3 shows possible methane sources and sinks of Martian methane.(Atreya et al., 2007; Chassefière and Leblanc, 2011) In the Earth atmosphere, more than 90% of the methane molecules come from biological activities. These recent detections of methane plumes in the Martian northern hemisphere sparked great interest for its possibilities of potential Martian biological origin. Based on photochemical models and

the current understanding of the composition of the Martian atmosphere, the predicted methane photochemical lifetime is ~ 300 years, which is very short on geological time scales. Recent measurements by Webster et al. detected a significantly shorter lifetime of a methane plume (< 1 year).(Webster et al., 2015) These short lifetimes indicate methane detected today have been injected into the atmosphere recently. Also, the detected short lifetime indicates methane sinks which might be unknown to the Earth atmospheric chemistry. More importantly, sources of these current day methane still remains a mystery.

Martian methane sources can be either be biological or abiotic. By analogy to Earth, biological methane could come from the existence of microbes known as methanogens existing deep under the surface and producing methane as a result of their metabolism.(Etiope and Lollar, 2013; Fu et al., 2007; Oze et al., 2012; Oze and Sharma, 2005) Abiotic Martian methane can be produced through geochemical processes.(Lyons et al., 2005; McCollom, 2016) It can be formed by oxidation of iron, similar to what happens in terrestrial hot springs or active volcanoes. Serpentinization is low temperature geological process possible to produce methane with the presence of water, carbon dioxide, and some catalysts.(Edwards and Ehlmann, 2016; Mayhew et al., 2013) It occurs when olivine reacts with water, forming serpentine mineral and molecular hydrogen. With the presence of certain catalysts, H₂ can reduce carbon dioxide to form methane through a Fischer-Tropsch-type (FTT) synthesis.(Abrajano et al., 1990; Berndt et al., 1996; Neubeck et al., 2011)

On the other hand, sinks of Martian methane are also not well constraint. Just like what happens to the Earth atmosphere, the main proposed Martian removal is photooxidation by OH and O(¹D) radicals. However, that was not sufficient enough as it estimates the methane lifetime more than 2 orders of magnitude longer than observed by Curiosity. Recent research has

proposed that heterogeneous reactions on Martian surface and dust can also act as methane sinks. Thus, laboratory studies of methane production and consumption reactions under Martian conditions has become very important.

METHANE SOURCE AND SINK ATTRIBUTION

The methods of methane source attribution include isotopic composition measurement and methane coemitting gas measurement. Isotope composition measurements uses the correlation between the $\delta^{13}\text{C}$ and δD of the methane to identify methane sources, shown in Fig. 1.3.(Schoell, 1980; Whiticar, 1999) The carbon and hydrogen isotope ratios of CH_4 generated are fundamental parameters for interpreting gas origins in natural settings, including abiotic methane and biotic methane.(Etiope and Lollar, 2013; McCollom, 2013; Stolper et al., 2015) In general, more negative $\delta^{13}\text{C}$ and δD values indicate biogenic sources, while more positive $\delta^{13}\text{C}$ and δD values indicate thermogenic sources.(Bernard et al., 1976; Douglas et al., 2016; Schoell, 1983; Whiticar, 1999) On the other hand, the biogenic methane produced by methanogens contains only pure methane while many thermogenic gases contain not only methane, but larger hydrocarbons such as ethane, propane, and butane.(Bernard et al., 1976; Claypool and Kvenvolden, 1983) Complimentary analysis of both the methane isotope and higher order hydrocarbon compositions were used when detailed methane source attribution is needed. Chapter 2 of this thesis demonstrated a cavity ring-down spectroscopy technique used to measure atmospheric ethane concentration for methane source attribution.

However, there have been examples in which both these parameters fail. Thus, an additional parameter to distinguish biogenic and thermogenic methane from each other is needed. One method is to differentiate them by their formation temperature, biogenic sources

produce methane with temperatures significantly lower. The formation temperature of the methane could be determined with measurement of the abundance of the doubly substituted methane isotopologues, $^{13}\text{CH}_3\text{D}$ and $^{12}\text{CH}_2\text{D}_2$. (Stolper et al., 2014; Yeung et al., 2012; Young et al., 2017; Young et al., 2016) However, these methane isotopologues have been challenging to measure mostly due to their very low abundance compare to the singly substituted isotopologues. Currently, methods developed for $^{13}\text{CH}_3\text{D}$ and $^{12}\text{CH}_2\text{D}_2$ measurements have been mostly focused on the use of isotope ratio mass spectrometry (IRMS), which faces the challenges of mass resolutions. In Chapter 4 of this thesis, I talk about the results from our frequency stabilized cavity ring-down spectrometer to measure abundance of $^{12}\text{CH}_2\text{D}_2$ in a naturally abundant methane sample for methane source attribution.

REFERENCES

- Abrajano, T.A., Sturchio, N.C., Kennedy, B.M., Lyon, G.L., Muehlenbachs, K. and Bohlke, J.K. (1990) GEOCHEMISTRY OF REDUCED GAS RELATED TO SERPENTINIZATION OF THE ZAMBALES OPHIOLITE, PHILIPPINES. *Appl. Geochem.* 5, 625-630.
- Allan, W., Lowe, D.C., Gomez, A.J., Struthers, H. and Brailsford, G.W. (2005) Interannual variation of C-13 in tropospheric methane: Implications for a possible atomic chlorine sink in the marine boundary layer. *Journal of Geophysical Research-Atmospheres* 110, 8.
- Allan, W., Struthers, H. and Lowe, D.C. (2007) Methane carbon isotope effects caused by atomic chlorine in the marine boundary layer: Global model results compared with Southern Hemisphere measurements. *Journal of Geophysical Research-Atmospheres* 112, 10.
- Atreya, S.K., Mahaffy, P.R. and Wong, A.S. (2007) Methane and related trace species on Mars: Origin, loss, implications for life, and habitability. *Planet Space Sci.* 55, 358-369.

- Bernard, B.B., Brooks, J.M. and Sackett, W.M. (1976) Natural gas seepage in the Gulf of Mexico. *Earth and Planetary Science Letters* 31, 48-54.
- Berndt, M.E., Allen, D.E. and Seyfried, W.E. (1996) Reduction of CO₂ during serpentinization of olivine at 300 degrees C and 500 bar. *Geology* 24, 351-354.
- Butler, J.H. and Montzka, S.A. (2017) The NOAA Annual Greenhouse Gas Index (AGGI).
- Chassefière, E. and Leblanc, F. (2011) Methane release and the carbon cycle on Mars. *Planet Space Sci.* 59, 207-217.
- Claypool, G.E. and Kvenvolden, K.A. (1983) METHANE AND OTHER HYDROCARBON GASES IN MARINE SEDIMENT. *Annu. Rev. Earth Planet. Sci.* 11, 299-327.
- Dlugokencky, E.J., Nisbet, E.G., Fisher, R. and Lowry, D. (2011) Global atmospheric methane: budget, changes and dangers. *Philosophical Transactions of the Royal Society A: Mathematical, Physical and Engineering Sciences* 369, 2058-2072.
- Douglas, P.M.J., Stolper, D.A., Smith, D.A., Anthony, K.M.W., Paull, C.K., Dallimore, S., Wik, M., Crill, P.M., Winterdahl, M., Eiler, J.M. and Sessions, A.L. (2016) Diverse origins of Arctic and Subarctic methane point source emissions identified with multiply-substituted isotopologues. *Geochim. Cosmochim. Acta* 188, 163-188.
- Edwards, C.S. and Ehlmann, B.L. (2016) Carbon sequestration on Mars. *Geology* 44, E389-E389.
- Etheridge, D.M., Steele, L.P., Francey, R.J. and Langenfelds, R.L. (1998) Atmospheric methane between 1000 A.D. and present: Evidence of anthropogenic emissions and climatic variability. *Journal of Geophysical Research: Atmospheres* 103, 15979-15993.
- Etiopé, G. and Lollar, B.S. (2013) ABIOTIC METHANE ON EARTH. *Rev. Geophys.* 51, 276-299.

Ferry, J.G. (1998) Enzymology of one-carbon metabolism in methanogenic pathways. *Microbiology Reviews* 23, 13-38.

Fu, Q., Lollar, B.S., Horita, J., Lacrampe-Couloume, G. and Seyfried, W.E. (2007) Abiotic formation of hydrocarbons under hydrothermal conditions: Constraints from chemical and isotope data. *Geochim. Cosmochim. Acta* 71, 1982-1998.

Hinrichs, K.-U., Hayes, J.M., Sylva, S.P., Brewer, P.G. and DeLong, E.F. (1999) Methane-consuming archaeobacteria in marine sediments. *Nature* 398, 802-805.

Kirschke, S., Bousquet, P., Ciais, P., Saunois, M., Canadell, J.G., Dlugokencky, E.J., Bergamaschi, P., Bergmann, D., Blake, D.R., Bruhwiler, L., Cameron-Smith, P., Castaldi, S., Chevallier, F., Feng, L., Fraser, A., Heimann, M., Hodson, E.L., Houweling, S., Josse, B., Fraser, P.J., Krummel, P.B., Lamarque, J.-F., Langenfelds, R.L., Le Quéré, C., Naik, V., O'Doherty, S., Palmer, P.I., Pison, I., Plummer, D., Poulter, B., Prinn, R.G., Rigby, M., Ringeval, B., Santini, M., Schmidt, M., Shindell, D.T., Simpson, I.J., Spahni, R., Steele, L.P., Strode, S.A., Sudo, K., Szopa, S., van der Werf, G.R., Voulgarakis, A., van Weele, M., Weiss, R.F., Williams, J.E. and Zeng, G. (2013) Three decades of global methane sources and sinks. *6*, 813.

Leshin, L.A., Mahaffy, P.R., Webster, C.R., Cabane, M., Coll, P., Conrad, P.G., Archer, P.D., Atreya, S.K., Brunner, A.E., Buch, A., Eigenbrode, J.L., Flesch, G.J., Franz, H.B., Freissinet, C., Glavin, D.P., McAdam, A.C., Miller, K.E., Ming, D.W., Morris, R.V., Navarro-Gonzalez, R., Niles, P.B., Owen, T., Pepin, R.O., Squyres, S., Steele, A., Stern, J.C., Summons, R.E., Sumner, D.Y., Sutter, B., Szopa, C., Teinturier, S., Trainer, M.G., Wray, J.J., Grotzinger, J.P. and Team, M.S.L.S. (2013) Volatile, Isotope, and Organic Analysis of Martian Fines with the Mars Curiosity Rover. *Science* 341, 9.

Lyons, J.R., Manning, C. and Nimmo, F. (2005) Formation of methane on Mars by fluid-rock interaction in the crust. *Geophysical Research Letters* 32, 4.

Mayhew, L.E., Ellison, E.T., McCollom, T.M., Trainor, T.P. and Templeton, A.S. (2013) Hydrogen generation from low-temperature water-rock reactions. *Nat. Geosci.* 6, 478-484.

McCollom, T.M. (2013) Laboratory Simulations of Abiotic Hydrocarbon Formation in Earth's Deep Subsurface. *Reviews in Mineralogy and Geochemistry* 75, 467-494.

McCollom, T.M. (2016) Abiotic methane formation during experimental serpentinization of olivine. *Proc. Natl. Acad. Sci. U. S. A.* 113, 13965-13970.

Neubeck, A., Duc, N.T., Bastviken, D., Crill, P. and Holm, N.G. (2011) Formation of H₂ and CH₄ by weathering of olivine at temperatures between 30 and 70 degrees C. *Geochem. Trans.* 12, 10.

Oze, C., Jones, L.C., Goldsmith, J.I. and Rosenbauer, R.J. (2012) Differentiating biotic from abiotic methane genesis in hydrothermally active planetary surfaces. *Proc. Natl. Acad. Sci. U. S. A.* 109, 9750-9754.

Oze, C. and Sharma, M. (2005) Have olivine, will gas: Serpentinization and the abiogenic production of methane on Mars. *Geophysical Research Letters* 32, 4.

Petit, J.R., Jouzel, J., Raynaud, D., Barkov, N.I., Barnola, J.M., Basile, I., Bender, M., Chappellaz, J., Davis, M., Delaygue, G., Delmotte, M., Kotlyakov, V.M., Legrand, M., Lipenkov, V.Y., Lorius, C., Pepin, L., Ritz, C., Saltzman, E. and Stievenard, M. (1999) Climate and atmospheric history of the past 420,000 years from the Vostok ice core, Antarctica. *Nature* 399, 429-436.

Platt, U., Allan, W. and Lowe, D. (2004) Hemispheric average Cl atom concentration from C-13/C-12 ratios in atmospheric methane. *Atmos. Chem. Phys.* 4, 2393-2399.

Ramaswamy, V., Boucher, O., Haigh, J., Hauglustine, D., Haywood, J., Myhre, G., Nakajima, T., Shi, G., Solomon, S. (2001) Radiative forcing of climate. *Climate Change*, 349-416.

Saunio, M., Bousquet, P., Poulter, B., Peregón, A., Ciais, P., Canadell, J.G., Dlugokencky, E.J., Etiope, G., Bastviken, D., Houweling, S., Janssens-Maenhout, G., Tubiello, F.N., Castaldi, S., Jackson, R.B., Alexe, M., Arora, V.K., Beerling, D.J., Bergamaschi, P., Blake, D.R., Brailsford, G., Brovkin, V., Bruhwiler, L., Crevoisier, C., Crill, P., Covey, K., Curry, C., Frankenberg, C., Gedney, N., Höglund-Isaksson, L., Ishizawa, M., Ito, A., Joos, F., Kim, H.S., Kleinen, T., Krummel, P., Lamarque, J.F., Langenfelds, R., Locatelli, R., Machida, T., Maksyutov, S., McDonald, K.C., Marshall, J., Melton, J.R., Morino, I., Naik, V., O'Doherty, S., Parmentier, F.J.W., Patra, P.K., Peng, C., Peng, S., Peters, G.P., Pison, I., Prigent, C., Prinn, R., Ramonet, M., Riley, W.J., Saito, M., Santini, M., Schroeder, R., Simpson, I.J., Spahni, R., Steele, P., Takizawa, A., Thornton, B.F., Tian, H., Tohjima, Y., Viovy, N., Voulgarakis, A., van Weele, M., van der Werf, G.R., Weiss, R., Wiedinmyer, C., Wilton, D.J., Wiltshire, A., Worthy, D., Wunch, D., Xu, X., Yoshida, Y., Zhang, B., Zhang, Z. and Zhu, Q. (2016a) The global methane budget 2000–2012. *Earth Syst. Sci. Data* 8, 697-751.

Saunio, M., Jackson, R.B., Bousquet, P., Poulter, B. and Canadell, J.G. (2016b) The growing role of methane in anthropogenic climate change. *Environmental Research Letters* 11, 120207.

Schoell, M. (1980) THE HYDROGEN AND CARBON ISOTOPIC COMPOSITION OF METHANE FROM NATURAL GASES OF VARIOUS ORIGINS. *Geochim. Cosmochim. Acta* 44, 649-661.

Schoell, M. (1983) GENETIC-CHARACTERIZATION OF NATURAL GASES. *AAPG Bull.-Am. Assoc. Petr. Geol.* 67, 2225-2238.

Stolper, D.A., Martini, A.M., Clog, M., Douglas, P.M., Shusta, S.S., Valentine, D.L., Sessions, A.L. and Eiler, J.M. (2015) Distinguishing and understanding thermogenic and biogenic sources of methane using multiply substituted isotopologues. *Geochim. Cosmochim. Acta* 161, 219-247.

Stolper, D.A., Sessions, A.L., Ferreira, A.A., Neto, E.V.S., Schimmelmann, A., Shusta, S.S., Valentine, D.L. and Eiler, J.M. (2014) Combined C-13-D and D-D clumping in methane: Methods and preliminary results. *Geochim. Cosmochim. Acta* 126, 169-191.

Thauer, R.K. (1998) Biochemistry of methanogenesis: a tribute to Marjory Stephenson:1998 Marjory Stephenson Prize Lecture. *Microbiology* 144, 2377-2406.

Webster, C.R., Mahaffy, P.R., Atreya, S.K., Flesch, G.J., Farley, K.A. and Team, M.S.L.S. (2013) Low Upper Limit to Methane Abundance on Mars. *Science* 342, 355-357.

Webster, C.R., Mahaffy, P.R., Atreya, S.K., Flesch, G.J., Mischna, M.A., Meslin, P.Y., Farley, K.A., Conrad, P.G., Christensen, L.E., Pavlov, A.A., Martin-Torres, J., Zorzano, M.P., McConnochie, T.H., Owen, T., Eigenbrode, J.L., Glavin, D.P., Steele, A., Malespin, C.A., Archer, P.D., Sutter, B., Coll, P., Freissinet, C., McKay, C.P., Moores, J.E., Schwenger, S.P., Bridges, J.C., Navarro-Gonzalez, R., Gellert, R., Lemmon, M.T. and Team, M.S.L.S. (2015) Mars methane detection and variability at Gale crater. *Science* 347, 415-417.

Whiticar, M.J. (1999) Carbon and hydrogen isotope systematics of bacterial formation and oxidation of methane. *Chem. Geol.* 161, 291-314.

Wuebbles, D.J., Hayhoe, K. (2002) Atmospheric methane and global change. *EarthScience Reviews* 57, 177-210.

Yeung, L.Y., Young, E.D. and Schauble, E.A. (2012) Measurements of (OO)-O-18-O-18 and (OO)-O-17-O-18 in the atmosphere and the role of isotope-exchange reactions. *Journal of Geophysical Research-Atmospheres* 117.

Young, E.D., Kohl, I.E., Lollar, B.S., Etiope, G., Rumble, D., Li, S., Haghnegahdar, M.A., Schauble, E.A., McCain, K.A., Foustoukos, D.I., Sutcliffe, C., Warr, O., Ballentine, C.J., Onstott, T.C., Hosgormez, H., Neubeck, A., Marques, J.M., Perez-Rodriguez, I., Rowe, A.R., LaRowe, D.E., Magnabosco, C., Yeung, L.Y., Ash, J.L. and Bryndzia, L.T. (2017) The relative abundances of resolved (CH₂D₂)-C-12 and (CH₃D)-C-13 and mechanisms controlling isotopic bond ordering in abiotic and biotic methane gases. *Geochim. Cosmochim. Acta* 203, 235-264.

Young, E.D., Rumble, D., Freedman, P. and Mills, M. (2016) A large-radius high-mass-resolution multiple-collector isotope ratio mass spectrometer for analysis of rare isotopologues of O-2, N-2, CH₄ and other gases. *International Journal of Mass Spectrometry* 401, 1-10.

FIGURES

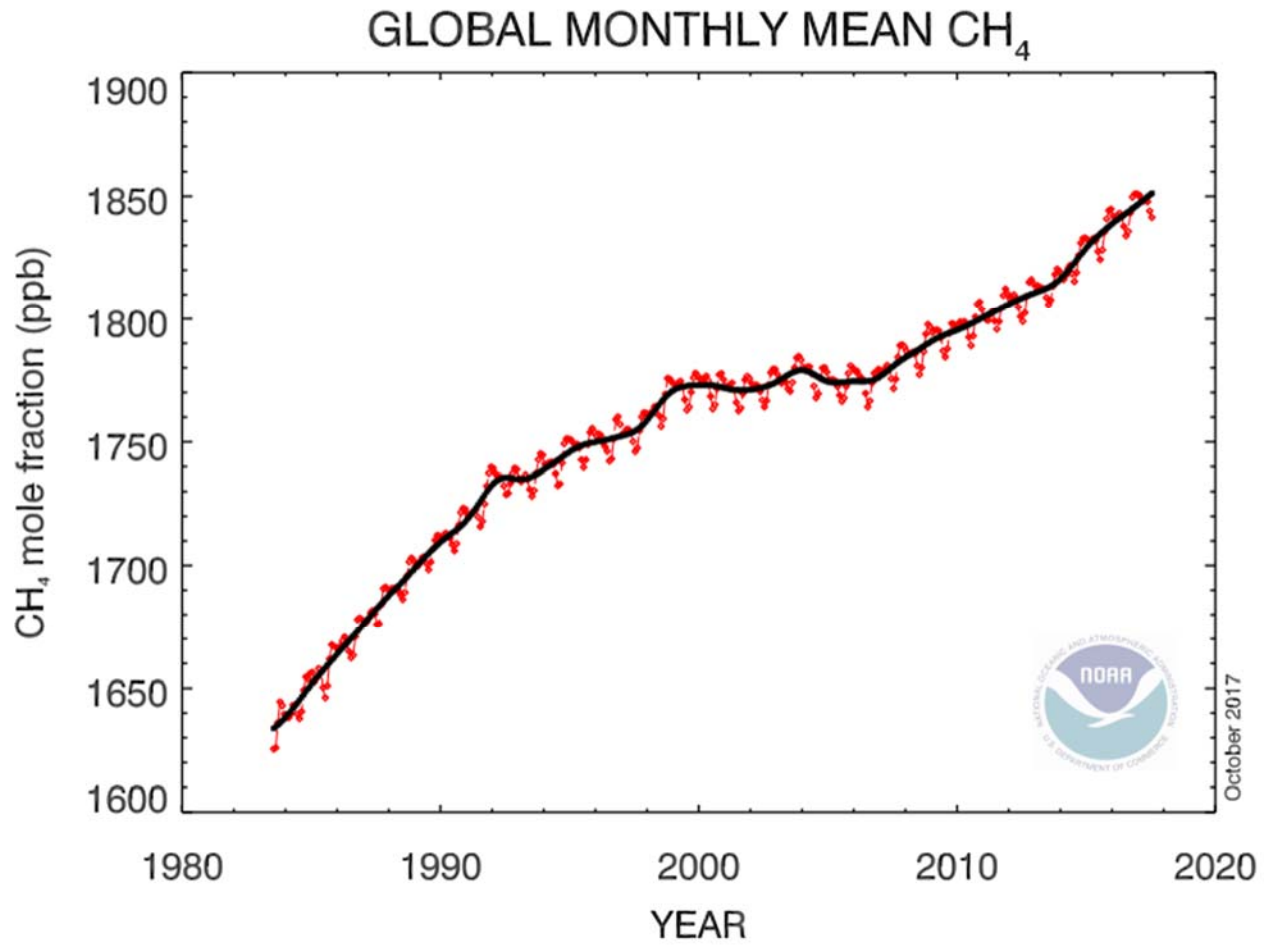


Figure. 1. 1. Global monthly mean atmospheric methane concentration reported in (Dlugokencky et al., 2011; Saunois et al., 2016a).

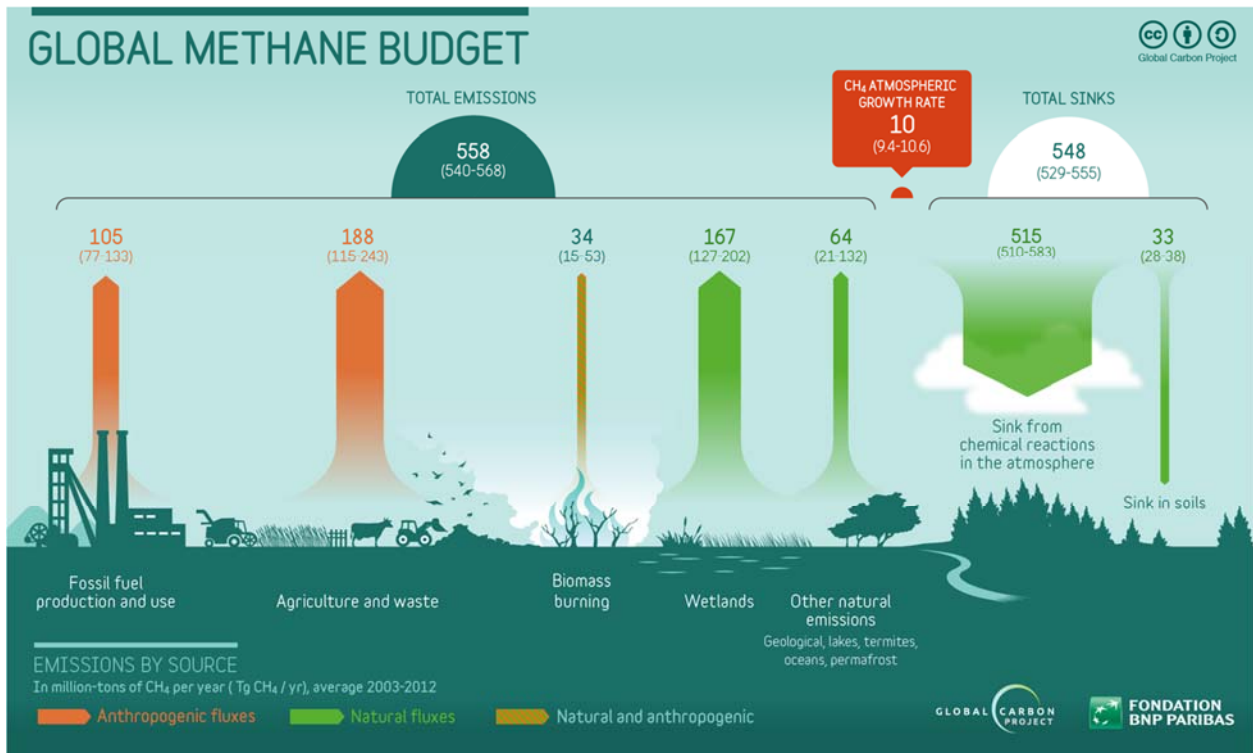


Figure. 1. 2. Global methane budget reported in (Dlugokencky et al., 2011; Saunois et al., 2016a).

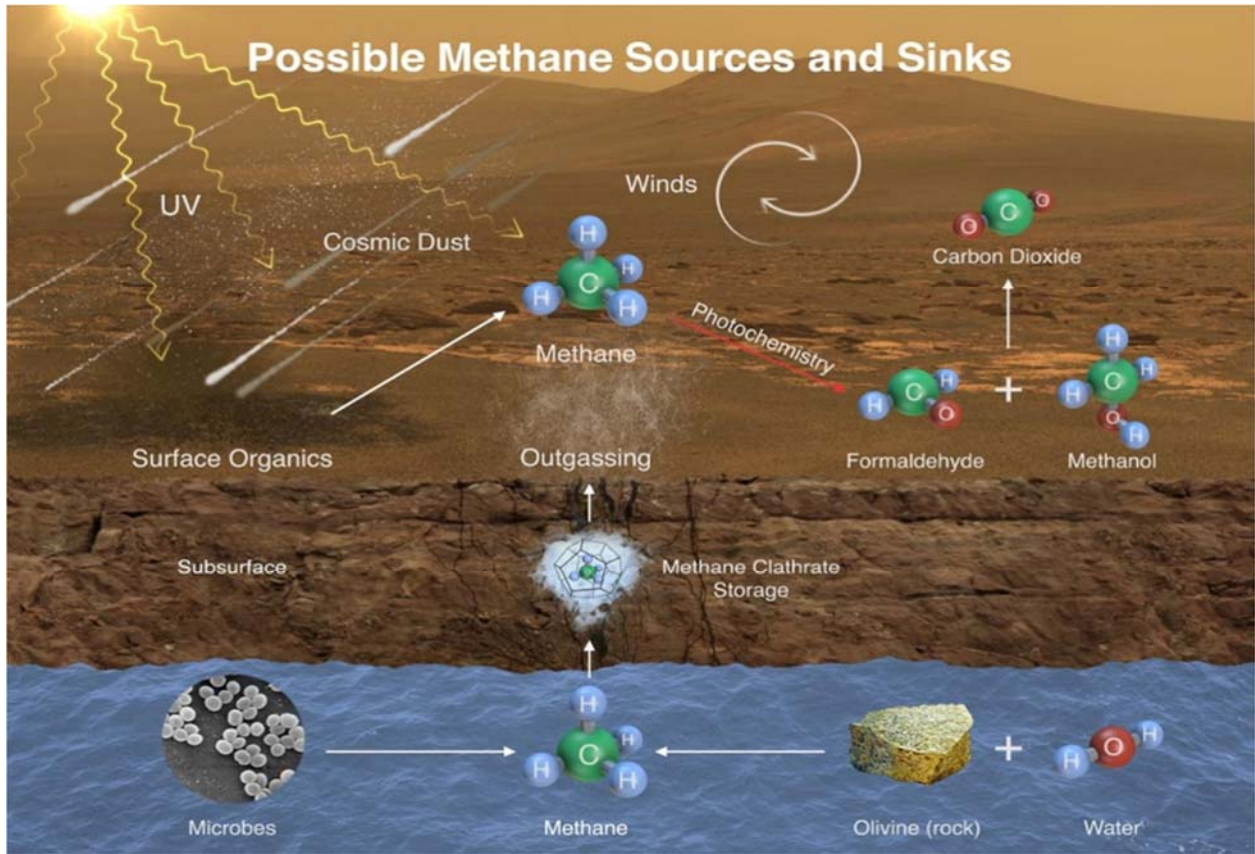


Figure 1. 3. Taken from NASA. Possible Martian methane sources and sinks.

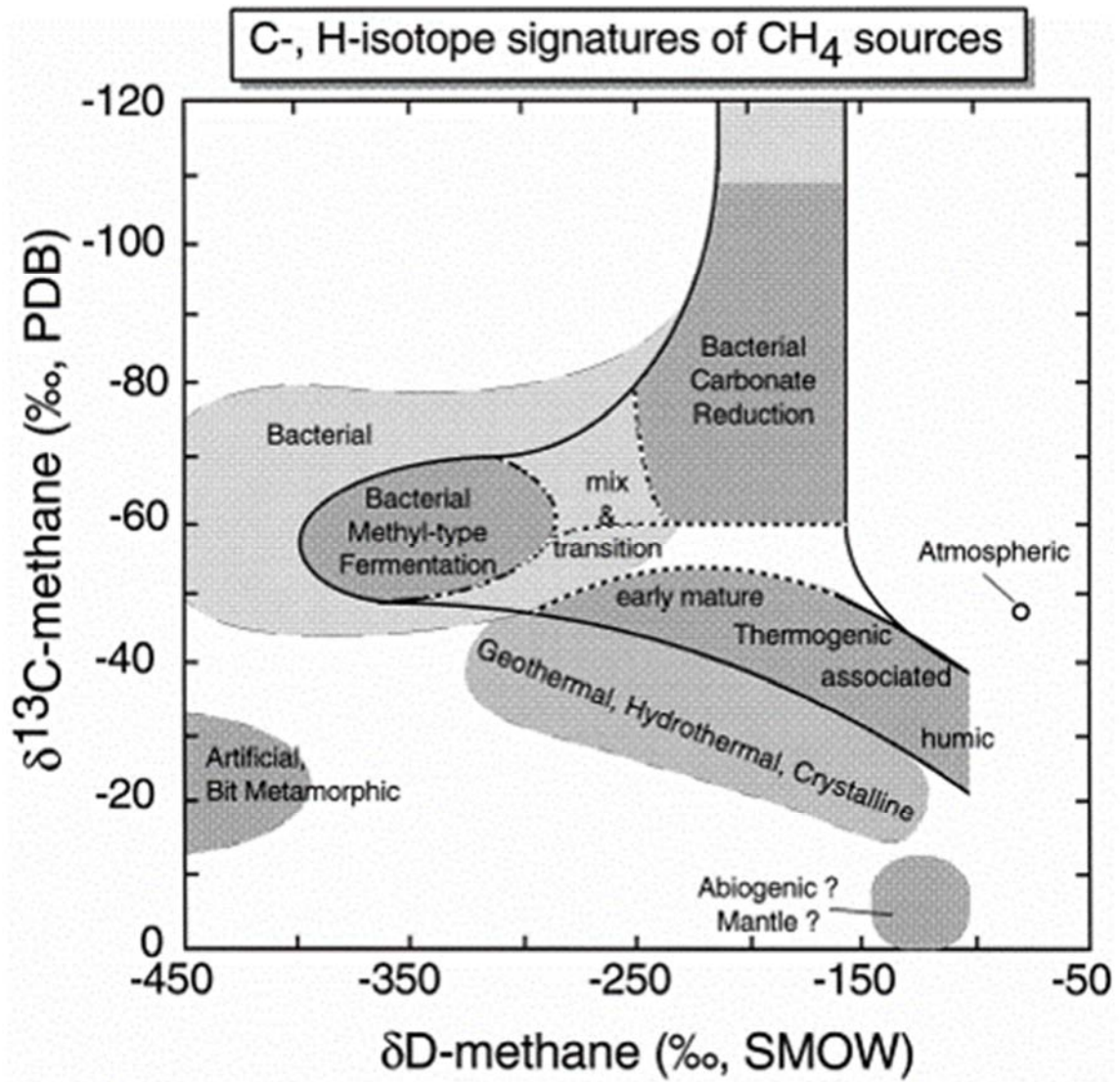


Figure 1. 4. Taken from (Whiticar, 1999). Isotopic map of methane sources.

**Chapter 2: Mid-Infrared Cavity Ring-down Spectroscopy Measurements
of Atmospheric Ethane Abundance**

ABSTRACT

Atmospheric methane is a very important greenhouse gas. Sources of methane plumes could be attributed using isotopic composition measurements and methane co-emitting gas (ethane, propane, and butane) detections. Since isotopic source attribution process requires sensitive detection of more than three methane isotopologues ($^{12}\text{CH}_4$, $^{13}\text{CH}_4$, and $^{12}\text{CH}_2\text{D}$), we chose to measure the highest abundant co-emitting gas, ethane. Ethane to methane ratio from biogenic and thermogenic sources have known to vary from 0.1% to 30%. In this work, we demonstrated the performance of a continuous-wave (cw) interband cascade laser (ICL) based mid-infrared cavity ring-down spectroscopy (CRDS) sensor for atmospheric ethane (C_2H_6) detection. A $3.36\ \mu\text{m}$ cw ICL with an was used to target two ethane absorption bands at $2976.788\ \text{cm}^{-1}$ and $2983.383\ \text{cm}^{-1}$. This technique utilizes the long effective pathlength (~ 4.5 km) of CRDS to increase sensitivity of atmospheric ethane detection. Our spectrometer can measure atmospheric ethane concentration as low as 200 pptv at standard temperature and pressure. We have used this instrument to measure the atmospheric ethane composition in ambient air collected in Pasadena, California.

INTRODUCTION

Methane, the primary component of natural gas, is an important greenhouse gas and has ~ 25 times more effective at trapping heat in the atmosphere.(Ramaswamy, 2001; Wuebbles, 2002) As the second highest emitted greenhouse gas from human activities, it contributes to $\sim 10\%$ of the anthropogenic greenhouse gas emission in 2015. From the pre-industrial era, atmospheric ethane concentration has increased by 162% globally.(Ferretti et al., 2005; Thauer, 1998) Although methane occurs naturally mostly through methane producing microbes known as

methanogens (Ferry, 1998), human activities have significantly changed its atmospheric concentration. Anthropogenic sources of methane include natural gas and petroleum systems, agricultural activities, landfills, coal mining, manure management, waste water treatment, and combustion. Among these methane emission sources, natural gas and petroleum systems contribute to ~ 29 % of anthropogenic methane emission, including a large contribution from fugitive emissions. It has been estimated that ~ 1.5 % of the natural gas production was lost through fugitive emissions, resulting in ~ 28 million tons of methane emission per year.(Solomon et al., 2007; Stocker et al., 2013) Methane emission from natural gas and petroleum systems has decreased significantly since 1990 due to the control of fugitive emissions, flaring, and gas venting. Thus, observing and locating atmospheric methane plumes near production, transportation, and delivery areas of natural gas becomes extremely important and effective in the control of anthropogenic methane emissions.

However, thermogenic methane emission sources such as natural gas and petroleum systems are often collocated with biogenic sources of methane such as livestock, landfills, or wetlands. One of the biggest challenges of atmospheric methane source identification is to be able to distinguish between different methane source types to quantify their contributions to ambient methane levels. The methods of methane source attribution include isotopic composition measurement and methane coemitting gas measurement. Isotope composition measurements uses the correlation between the $\delta^{13}\text{C}$ and δD of the methane to identify methane sources.(Schoell, 1980) In general, more negative $\delta^{13}\text{C}$ and δD values indicate biogenic sources, while more positive $\delta^{13}\text{C}$ and δD values indicate thermogenic sources.(Bernard et al., 1976; Douglas et al., 2016; Schoell, 1983; Whiticar, 1999) On the other hand, the biogenic methane produced by methanogens contains only pure methane while many thermogenic gases contain

not only methane, but larger hydrocarbons such as ethane, propane, and butane.(Bernard et al., 1976; Claypool and Kvenvolden, 1983) Complimentary analysis of both the methane isotope and higher order hydrocarbon compositions were used when detailed methane source attribution is needed. However, for instantaneous and small sample atmospheric sample analysis, high order hydrocarbon analysis is more suitable due to their higher absolute concentrations than $^{12}\text{CH}_3\text{D}$ and larger variation due to different sources. The most commonly analyzed higher order hydrocarbon is ethane. The typical range of ethane/methane enhancement ratio known of biogenic sources is $< 0.2\%$ (Oremland, 1981), while that of thermogenic sources are $> 6\%$ with some sources as high as 45% .(Yacovitch et al., 2014) Thus, trace ethane abundance measurements can be very beneficial to the source attribution of atmospheric methane. Compare to mass spectrometry and gas chromatography methods, optical methods based on laser spectroscopy are more suitable for these analysis for the advantages such as compact size, lower cost, and no pretreatment or purification process require.(Fischer and Sigrist, 2002; Lancaster and Dawes, 1996; Lancaster et al., 2000; Petrov et al., 1997; Richter et al., 1998; Zhao et al., 2002)

Spectroscopic analysis of ethane has been explored extensively not only for the application in atmospheric trace gas analysis, but also for medical applications of breath analysis.(Parameswaran et al., 2009) These trace ethane abundance observation methods have been mostly focusing on measurements of the ethane ro-vibrational transitions in the mid-infrared region ($\sim 3.3\ \mu\text{m}$), taking advantage of the large absorption cross sections in this spectral region.(Brown et al., 1987; Coffey et al., 1985; Gordon et al., 2017; Harrison et al., 2010; Zhao et al., 2002) The most widely used optical trace gas analysis methods used for atmospheric alkanes include tunable diode laser absorption spectroscopy (TDLAS), frequency modulated

TDLAS (Patterson et al., 2007; Wysocki et al., 2007), integrating cavity output spectroscopy (ICOS) (Parameswaran et al., 2009; von Basum et al., 2004), and cavity ring-down spectroscopy (CRDS) (Ngai et al., 2006). (Hodgkinson and Tatam, 2013) Among these techniques, CRDS is a more sensitive technique due to its enhancement in light molecule interaction pathlength and immunity to laser light intensity noise. (Romanini et al., 1997; Zalicki and Zare, 1995) However, CRDS requires a more powerful laser source and sensitive photon detection, which limits the application of the technique. Recent improvement in the manufacturing of high power lasers in the 3.3 μm region, especially interband cascade lasers, has made it possible for CRDS measurements of trace gases in this spectral region. (Meyer and Vurgaftman, 2010; Parameswaran et al., 2009; Sonnenfroh et al., 2010; Vurgaftman et al., 2010; Wysocki et al., 2007)

In this work, we demonstrated a prototype continuous wave cavity ring-down spectrometer for atmospheric ethane abundance measurements. This spectrometer utilizes the application of a newly developed interband cascade laser to measure ethane in the 3.36 μm region. Our spectrometer can measure atmospheric ethane concentration as low as 200 pptv at standard temperature and pressure. We have used this instrument to measure the atmospheric ethane composition in ambient air collected in Pasadena, California.

EXPERIMENTAL

Spectrometer

The spectrometer as shown in Fig 2.1 is constructed of five main parts, light source, optical shutter, cavity, detector, and beam manipulation optics. The light source is a single-mode high-power interband cascade (IC) laser designed and manufactured by the JPL Micro-devices

Laboratory.(Borgentun et al., 2015) The line center of the laser is at 2977 cm^{-1} with a tunable range between 2972 cm^{-1} and 2984 cm^{-1} . The laser linewidth was measured to be 3 MHz with a heterodyne beat note experiment. The TEC tuning range of the laser is $5\text{ }^{\circ}\text{C}$ to $15\text{ }^{\circ}\text{C}$ and the threshold drive current is 175 mA. When driving at maximum current (375 mA), the optical output power of the laser peaks at 16 mW with 25 dB side-mode attenuation. The laser is mounted on an actively temperature stabilized aluminum block. Temperature stabilization is achieved using a temperature controller from Wavelength Electronics (HTC-1500). The temperature of the aluminum block is monitored with a stick on surface-mounted thermistor sensor. A water cooled peltier thermoelectric cooler is attached to the laser mounting block for active cooling to maintain it at $20\text{ }^{\circ}\text{C}$. The laser output is collimated with an anti-reflective (AR) coated aspheric lens (Lightpath 390036-IR4) with a focal length of 3.05 mm.

The collimated laser beam is then coupled into an acousto-optic modulator (AOM), which acts as an optical shutter. An AOM was chosen instead of other optical shutters due to its short rise time (110 ns). The AOM (Brimrose GEM-60-5-3330) is made with a germanium substrate AR coated to operate at $3330 \pm 50\text{ nm}$ with transmission of 85%. In order to achieve maximum coupling efficiency, the collimated laser beam is focused to be smaller than the active aperture (1 mm diameter) of the AOM at the position of the AOM crystal. The AOM is aligned to optimize diffraction efficiency (70%) to the first order diffracted beam. The first order beam from the AOM is then coupled into the cavity.

The cavity is designed to have a geometry of a confocal resonator with two mirrors (Los Gatos Research) with equal curvature (1 meter) and reflectivity ($R = 99.98\%$) placed coaxial from each other, yielding a cavity finesse of 15000. The cavity length, physical distance between the two reflecting mirrors, is 82.2 cm, resulting in the free spectral range (FSR) of the

cavity resonator to be 182.5 MHz and effective pathlength of 4000 meters. The mirrors are submerged in a vacuum environment enclosed with AR coated windows on both ends. The pressure of the cavity is monitored with a 1000 Torr Baratron absolute capacitance manometer (MKS 626C13TBE).

The transmitted light from the cavity is focused and detected by a thermoelectric cooled mercury cadmium telluride detector (Vigo, PVI-4TE-3.4) with a paired preamplifier (MIPDCv2-F-10) with a cut-off frequency of 10 MHz. When the laser frequency is not on resonance with a cavity mode, there is no light transmitted out of the cavity. When on resonance, small amount of light is transmitted from the cavity and detected by the photodetector. The detected signal is then sent into a low-noise voltage preamplifier (Stanford Research Systems, SR560) set with 50 gain. The amplified signal was then sent into both a digitizer and a digital delay generator (DDG, Stanford Research Systems, DG535). The signal at the DDG triggers a simultaneous generation of two TTL pulses, one to shut off the AOM, the other to trigger the digitizer. The digitizer then observes the decay of light intensity from the time when AOM was turned off, which is the ring-down signal.

In order to scan for a spectrum, TEC temperature of the laser is tuned to step through consecutive cavity modes. Laser resonance with a cavity mode is maintained by slowly modulate the laser current with a triangular waveform of 1 Hz and 0.05 mA, which results in a modulation depth of 65 MHz on the laser frequency. The amplified detector signal is also sent to another DDG (BNC, Model 575), triggering it to generate a TTL pulse every time the signal level exceeds a preset threshold. Probability distribution triangular waveform to maintain the peak of the distribution at the center, thus keeps the laser on resonance. When on resonance, the average ring-down acquisition rate is 100 Hz.

Sample Preparation

Two different types of gas samples were measured to demonstrate the capability of this instrument: (i) diluted methane and ethane samples in zero air, (ii) dry ambient air sample. Samples were expanded into the cavity, which was evacuated to $\sim 10^{-4}$ Torr, until pressures inside the cavity and sample cells or flasks reached an equilibrium.

The diluted samples were mixed in a stainless steel tank and individual measurements were done by filling a 2 L Pyrex cell with the well mixed tank content using a stainless steel gas line. The tank and gas lines were first pumped down to $\sim 10^{-6}$ Torr with a diffusion pump. Methane (Spectra Gases, research grade pure methane), ethane (Sigma Aldrich, 295392-110G), or methane ethane mixture (Matheson Tri Gas, Gravimetric mixture, 0.5% ethane balanced in methane) sample was first filled into the tank to the desired pressure measured with a 100 Torr Baratron (MKS, 626C1212TDE); zero air gas was then filled to the high pressure target measured with a 10,000 Torr Baratron (MKS, 722B14TCD2FJ). The mixed tank was then left to equilibrate for more than 24 hours prior to use. When tank content was used, the Pyrex cell and gas line were pumped down with a diffusion pump before slowly expanding gas from the well mixed tank to the cell to the desired pressure. The total pressure of the cell was measured with either the 100 Torr or 10,000 Torr Baratron depending on the desired total pressure of the cell.

The dry ambient air samples were collected from two different locations. The urban air samples were collected on Caltech campus located in the city of Pasadena, about 14 km northeast of downtown Los Angeles. To compare data from the urban location with nominally “clean” environment in the same region, two sets of samples were collected near a southwest facing beach in San Pedro on the Palos Verdes peninsula (PV site) ~ 50 km SSW of Pasadena. The PV site is far removed from industrial emissions and could be considered as characteristic of the

local background. All of the ambient air samples were collected during daytime. Samples were collected into 2 L Pyrex flasks. These flasks were first evacuated to $\sim 10^{-4}$ Torr and then filled with dry air samples till ambient pressure. All air samples were dried by passing through a trap filled with $\text{Mg}(\text{ClO}_4)_2$ before entering the flask. Detailed sample collection procedure was described by Newman et al. (Newman et al., 2008) Each sample was collected with a duplicate filled 2 – 5 minutes later.

Measurement Procedure

The premixed and ambient air samples are measured by expanding the gas samples from the Pyrex flasks into the cavity until equilibrium is reached. For each sample, two spectra are collected, one scanned between 2976.4 cm^{-1} and 2977.4 cm^{-1} , the other scanned between 2983.1 cm^{-1} and 2983.7 cm^{-1} . Each measurement is done by stepping through the laser frequency with intervals of the cavity FSR (182.5 MHz). At each frequency, 100 ringdown time measurements (τ) are collected to report an average cavity loss. With an empty cavity, the typical ringdown time is $\sim 16 \mu\text{s}$, resulting in an empty cavity loss of $\sim 166 \text{ ppm}$. Scanning speed of the spectrometer is $\sim 45 \text{ min/cm}^{-1}$.

RESULTS AND DISCUSSION

Spectrometer Sensitivity

Figure 2.2 shows the Allan deviation plot of the baseline losses at 2976.788 cm^{-1} , collected for up to 20,000 ring-down decay acquisitions at a rate of $\sim 20 \text{ Hz}$. The Allan deviation displays a power law relationship with respect to the number of ring-down acquisitions, where the fitted slope is -0.551. It can be shown in the Allan deviation plot that

white noise dominates up to ~ 1000 ring-down decays, which corresponds to approximately 50 seconds of ring-down time averaging. We achieved a typical detectable absorbance of $\alpha_{\min} \sim 2.85 \times 10^{-9} \text{ cm}^{-1}$, which translates to the noise equivalent absorption (NEA) of $2.02 \times 10^{-8} \text{ cm}^{-1} \text{ Hz}^{-1/2}$.

Premixed Sample Measurements

The most accurate determinations of concentration require measuring integrated line intensities by fitting observed lines to an appropriate spectral lineshape model, rather than simply measuring peak heights of each transition. For the case of the ethane concentration measurements, the line parameters are complicated, which makes the absolute concentration retrieval difficult. Since the obtained ambient samples have complicated gas compositions with a wide variety of ethane abundance and total pressure, it is very important for us to carefully characterize the spectrometer.

We first measured a methane sample diluted in zero air (~ 50 ppm methane in air) at different pressures. The $^{12}\text{CH}_4$ transition at 2978.644 cm^{-1} was measured between 2 Torr and 81.9 Torr with 3 spectra at each pressure. This transition was chosen for its minimal interference from nearby transitions and well known line parameters from the HITRAN database.(Gordon et al., 2017) Measurements were started at 81.9 Torr total pressure sample, with gases pumped out to reach desired pressure. This pressure range was chosen to avoid interference from nearby transitions at high pressure conditions. The spectra were each then fitted with a Galatry profile to integrate the area under each transition.(Dufour et al., 2003; Hubbert and Troup, 1977) Figure 2.3 shows a sample spectrum at 30 Torr with the black dots in the upper panel as measured data, red solid line as the fit profiles, and the bottom panel as the residual between the data and the fit. The signal to noise ratio (SNR) of the fit reported for each spectrum is defined as the peak

absorption divided by the root mean square (RMS) noise of the residual. The reported SNR for this spectrum was $\sim 720:1$. The Galatry profile is used because the commonly used Voigt profile is often inadequate for modeling infrared methane spectra, because it neglects other collisional effects such as Dicke (collisional) narrowing.(Dicke, 1953) The fitted results showed a linear dependence of the integrated area and pressure broadened linewidth component as a function of pressure and approaching zero when pressure approaches zero. At 2 Torr total pressure, the SNR of the fit was $\sim 55:1$. Thus, our detection limit for $^{12}\text{CH}_4$ at this line is ~ 2 ppt STP assuming 1:1 SNR.

We then proceeded to demonstrate the performance of the instrument with measurements of the ethane in zero air samples. First, a pressure dependence study of a 100 ppb ethane in zero air sample was done similar to the methane experiments discussed above between 0.5 Torr and 34.2 Torr. Although the laser tuning range covers three ethane bands centered at 2976.788 cm^{-1} , 2980.073 cm^{-1} , and 2983.383 cm^{-1} , only the first and last bands were measured due to large water absorption interference near the 2980.073 cm^{-1} band. The 2976.788 cm^{-1} band was measured between 2976.30 cm^{-1} and 2977.30 cm^{-1} , while the 2983.383 cm^{-1} was measured between 2983.05 cm^{-1} and 2983.70 cm^{-1} . Starting and end frequencies of the laser were measured using a Bristol wavemeter. Line intensity of individual ethane band was integrated with a multiple Voigt profile spectral fit. The simpler Voigt profile was chosen due to the complicated absorption profiles of the ethane transitions. The HITRAN database assigned 372 transitions in the 2976.788 cm^{-1} scan range and 48 transitions in the 2983.383 cm^{-1} scan range.(Gordon et al., 2017) Thus, rigorous line shape studies of these two bands with the more complicated Galatry profile is not possible. Integrated areas of both bands were shown to be linearly dependent to the total pressure, which corresponds to the number density of ethane, with zero intercept.

To simulate pressure and ethane abundance conditions similar to the ones of an ambient sample, spectra of a ~ 10 ppb ethane in 250 Torr zero air sample were studied within the two spectral windows chosen above (Fig 2.4). The spectrum collected between 2976.30 cm^{-1} and 2977.30 cm^{-1} was fitted as a sum of two Voigt profiles with a linear baseline, while the spectrum collected between 2983.05 cm^{-1} and 2983.70 cm^{-1} was fitted with a single Voigt profile with a linear baseline. The SNR of the fitted results were $\sim 25:1$ and $\sim 42:1$, respectively. The higher SNR for the 2983.383 cm^{-1} arise from the larger peak height despite the lower integrated line strength of ethane transitions in this spectral window. The two spectra shown in Fig 2.4 were measured back and forth for 6 times within a total of 12 hours to test the reproducibility of the ethane measurement. The standard error for each spectrum was reported as 0.29 % and 0.27 %, respectively. Although measurements of either of these two ethane bands has been proven to be reproducible, ethane abundances calculated from each integrated area when using the integrated line strength reported in the HITRAN database ($S_{2976.788} = 4.050 \times 10^{-19}\text{ cm}^{-1}/\text{molecule cm}^{-2}$, $S_{2983.383} = 3.969 \times 10^{-19}\text{ cm}^{-1}/\text{molecule cm}^{-2}$) yield different results: 9.98 (3) ppb and 10.89 (3) ppb.(Gordon et al., 2017) Thus, a careful calibration of the ethane measurement with a known standard is needed.

Since a known calibrated ethane standard is rare, we designed a set of standardization experiments to approach more accurate ethane concentration measurements by utilizing the more well-known methane line parameters and the easier access methane standard. These standardization experiments were carried out by measuring methane and ethane abundance of a gravimetrically mixed 0.5% ethane in methane sample diluted in zero air. The ethane in methane mixture was first diluted to ~ 2 ppm methane in zero air and filled to the 2 L Pyrex cell to ~ 760 Torr total pressure. Methane abundance of the diluted sample was then measured using a Picarro

gas concentration analyzer, which was calibrated with a NOAA trace gas standard.

Standardization process of the Picarro instrument used has been used and documented previously by Newman et al. (Newman et al., 2008) Ethane concentration of the diluted gas sample was then measured at both of the selected spectral window for 3 times. The spectral window for the 2976.788 cm^{-1} band was extended to 2976.20 cm^{-1} on the low frequency end in order to retrieve methane concentration. Methane concentration of the diluted sample was measured by integrating methane transitions centered at 2976.343 cm^{-1} and 2976.455 cm^{-1} . The calibration experiments were repeated 3 times with a fresh gas fill each time. Results of these calibrated experiments were shown in Table 1. The ethane abundances reported in the table were calculated from the HITRAN reported integrated line strength in each spectral window. Thus, the corrected integrated line strength for the two bands are $S_{2976.788} = 4.341 (16) \times 10^{-19} \text{ cm}^{-1}/\text{molecule cm}^{-2}$, $S_{2983.383} = 3.887 (9) \times 10^{-19} \text{ cm}^{-1}/\text{molecule cm}^{-2}$.

Ambient Air Sample Measurements

The calibrated instrument was then used to measure atmospheric ethane abundance in ambient air samples collected at either the Caltech sample collection site and the PV site. The sample contents were first measured using the Picarro analyzer to obtain methane abundance, carbon dioxide abundance, and $^{13}\text{CO}_2$ abundance ($\delta^{13}\text{C}$). The remaining of the samples were then expanded into the cavity and equilibrated to measure the ethane abundance. Ethane was measured once within each spectral window. For the Caltech site samples, the ethane concentrations were high enough to be observed in both spectral windows and the reported ethane abundance is an average of the measured results from these two spectra. However, ethane concentrations in the PV site samples were too low to be observed in the 2976.788 cm^{-1} band due to small signal and interference from nearby methane and water transitions. Thus, the reported

ethane results for these samples were from measurements of the 2983.383 cm^{-1} band only. Table 2.2 is a list of the results from the ambient air sample measurements. The errors included in the reported ethane data include, uncertainty in the corrected line strength and uncertainty reported in the integrated area of each spectrum.

The scatter plot of ethane vs. methane measurements (Fig. 2.5(a)) is a determination of the ethane/methane enhancement ratio in the well mixed urban atmosphere. Our results show a linear correlation between the ethane and methane abundance in the atmosphere at different time of the day, indicating a relatively similar methane source. Within the 8 samples collected at the Caltech site one can observe that although methane abundance only increased $\sim 13.5\%$, the ethane abundance in the atmosphere increased by more than 5.5 times. This shows that ethane content is a great tracer for changes of atmospheric methane content.

Further analysis of these data is to investigate correlation between the ethane content and isotope content of carbon dioxide from the same sample. The ethane contents were then expressed as a percentage of emitted methane ($\text{ppb/ppb} \cdot 100\%$) and plotted against the $\delta^{13}\text{C}$ of CO_2 in the atmospheric air sample (Fig. 2.5(b)). The linear correlation between the ethane to methane ratio and $\delta^{13}\text{C}_{\text{CO}_2}$ can be further investigated to study the relationship between methane emission and consumption pathways within a possible methane plume.

Future work on the development of our spectrometer include: (1) decrease the spectrum scan time by a factor of 2 by scanning the laser frequency with a spacing of $2 \cdot \text{FSR}$; (2) implement gas flow system to allow real-time atmospheric sample measurement to replace flask sample measurements; (3) frequency stabilize the IC laser with a known molecular transition to increase precision of the spectrometer, and (4) utilize a different laser centered at 2996.87 cm^{-1} ,

which has proven to be a more well characterized and interference free transition for ethane concentration measurement. (Harrison et al., 2010; Yacovitch et al., 2014; Ye et al., 2016)

CONCLUSION

We have demonstrated a mid-IR (3.3 μm) cw cavity ring-down spectrometer capable of measuring atmospheric ethane abundance. This technique utilizes the long effective pathlength (~ 4.5 km) of cavity ring-down spectroscopy to increase sensitivity of atmospheric ethane detection. Single wavelength Allan variation measurement shows that our spectrometer can measure atmospheric ethane concentration as low as 200 ppt at standard temperature and pressure. We have also shown that we can reach a precision of 0.3 % with ~ 5 hours of averaging of a single ethane band measurement. We have used this instrument to measure the atmospheric ethane abundance in ambient air in Pasadena, California and shown linear correlations between ethane and methane concentrations, and between ethane to methane ratio and $\delta^{13}\text{C}$ of CO_2 in the same samples.

ACKNOWLEDGMENTS

This work was supported by the Caltech and JPL President's and Director's Fund (PDF). L. S. and T. Q. B were supported by NASA Earth and Space Science Fellowships (NESSF). E. M. L was supported by the NSF graduate research fellowship program (GRFP).

REFERENCES

- Bernard, B.B., Brooks, J.M. and Sackett, W.M. (1976) Natural gas seepage in the Gulf of Mexico. *Earth and Planetary Science Letters* 31, 48-54.
- Borgentun, C., Frez, C., Briggs, R.M., Fradet, M. and Forouhar, S. (2015) Single-mode high-power interband cascade lasers for mid-infrared absorption spectroscopy. *Opt. Express* 23, 2446-2450.
- Brown, L.R., Farmer, C.B., Rinsland, C.P. and Toth, R.A. (1987) MOLECULAR LINE PARAMETERS FOR THE ATMOSPHERIC TRACE MOLECULE SPECTROSCOPY EXPERIMENT. *Appl. Optics* 26, 5154-5182.
- Claypool, G.E. and Kvenvolden, K.A. (1983) METHANE AND OTHER HYDROCARBON GASES IN MARINE SEDIMENT. *Annu. Rev. Earth Planet. Sci.* 11, 299-327.
- Coffey, M.T., Mankin, W.G., Goldman, A., Rinsland, C.P., Harvey, G.A., Devi, V.M. and Stokes, G.M. (1985) INFRARED MEASUREMENTS OF ATMOSPHERIC ETHANE (C₂H₆) FROM AIRCRAFT AND GROUND-BASED SOLAR ABSORPTION-SPECTRA IN THE 3000 CM⁻¹ REGION. *Geophysical Research Letters* 12, 199-202.
- Dicke, R.H. (1953) The Effect of Collisions upon the Doppler Width of Spectral Lines. *Physical Review* 89, 472-473.
- Douglas, P.M.J., Stolper, D.A., Smith, D.A., Anthony, K.M.W., Paull, C.K., Dallimore, S., Wik, M., Crill, P.M., Winterdahl, M., Eiler, J.M. and Sessions, A.L. (2016) Diverse origins of Arctic and Subarctic methane point source emissions identified with multiply-substituted isotopologues. *Geochim. Cosmochim. Acta* 188, 163-188.

Dufour, G., Hurtmans, D., Henry, A., Valentin, A. and Lepère, M. (2003) Line profile study from diode laser spectroscopy in the 12CH_4 $2\nu_3$ band perturbed by N_2 , O_2 , Ar, and He. *Journal of Molecular Spectroscopy* 221, 80-92.

Ferretti, D.F., Miller, J.B., White, J.W.C., Etheridge, D.M., Lassey, K.R., Lowe, D.C., Meure, C.M.M., Dreier, M.F., Trudinger, C.M., van Ommen, T.D. and Langenfelds, R.L. (2005) Unexpected changes to the global methane budget over the past 2000 years. *Science* 309, 1714-1717.

Ferry, J.G. (1998) Enzymology of one-carbon metabolism in methanogenic pathways. *Microbiology Reviews* 23, 13-38.

Fischer, C. and Sigrist, M.W. (2002) Trace-gas sensing in the 3.3- μm region using a diode-based difference-frequency laser photoacoustic system. *Applied Physics B-Lasers and Optics* 75, 305-310.

Gordon, I.E., Rothman, L.S., Hill, C., Kochanov, R.V., Tan, Y., Bernath, P.F., Birk, M., Boudon, V., Campargue, A., Chance, K.V., Drouin, B.J., Flaud, J.M., Gamache, R.R., Hodges, J.T., Jacquemart, D., Perevalov, V.I., Perrin, A., Shine, K.P., Smith, M.A.H., Tennyson, J., Toon, G.C., Tran, H., Tyuterev, V.G., Barbe, A., Császár, A.G., Devi, V.M., Furtenbacher, T., Harrison, J.J., Hartmann, J.M., Jolly, A., Johnson, T.J., Karman, T., Kleiner, I., Kyuberis, A.A., Loos, J., Lyulin, O.M., Massie, S.T., Mikhailenko, S.N., Moazzen-Ahmadi, N., Müller, H.S.P., Naumenko, O.V., Nikitin, A.V., Polyansky, O.L., Rey, M., Rotger, M., Sharpe, S.W., Sung, K., Starikova, E., Tashkun, S.A., Auwera, J.V., Wagner, G., Wilzewski, J., Wcisło, P., Yu, S. and Zak, E.J. (2017) The HITRAN2016 molecular spectroscopic database. *Journal of Quantitative Spectroscopy and Radiative Transfer*.

Harrison, J.J., Allen, N.D.C. and Bernath, P.F. (2010) Infrared absorption cross sections for ethane (C₂H₆) in the 3 μ m region. *J. Quant. Spectrosc. Radiat. Transf.* 111, 357-363.

Hodgkinson, J. and Tatam, R.P. (2013) Optical gas sensing: a review. *Meas. Sci. Technol.* 24, 59.

Hubbert, R.G. and Troup, G.J. (1977) Single-mode 3.39 μ m laser study of methane absorption lineshape. *Physics Letters A* 61, 33-34.

Lancaster, D.G. and Dawes, J.M. (1996) Methane detection with a narrow-band source at 3.4 μ m based on a Nd:YAG pump laser and a combination of stimulated Raman scattering and difference frequency mixing. *Appl. Optics* 35, 4041-4045.

Lancaster, D.G., Weidner, R., Richter, D., Tittel, F.K. and Limpert, J. (2000) Compact CH₄ sensor based on difference frequency mixing of diode lasers in quasi-phasematched LiNbO₃. *Opt. Commun.* 175, 461-468.

Meyer, J. and Vurgafman, I. (2010) Quantum and Interband Cascade Lasers. *Opt. Eng.* 49, 2.

Newman, S., Xu, X., Affek, H.P., Stolper, E. and Epstein, S. (2008) Changes in mixing ratio and isotopic composition of CO₂ in urban air from the Los Angeles basin, California, between 1972 and 2003. *Journal of Geophysical Research: Atmospheres* 113, n/a-n/a.

Ngai, A.K.Y., Persijn, S.T., Von Basum, G. and Harren, F.J.M. (2006) Automatically tunable continuous-wave optical parametric oscillator for high-resolution spectroscopy and sensitive trace-gas detection. *Applied Physics B-Lasers and Optics* 85, 173-180.

Oremland, R.S. (1981) MICROBIAL FORMATION OF ETHANE IN ANOXIC ESTUARINE SEDIMENTS. *Appl. Environ. Microbiol.* 42, 122-129.

Parameswaran, K.R., Rosen, D.I., Allen, M.G., Ganz, A.M. and Risby, T.H. (2009) Off-axis integrated cavity output spectroscopy with a mid-infrared interband cascade laser for real-time breath ethane measurements. *Appl. Optics* 48, B73-B79.

Patterson, C.S., McMillan, L.C., Longbottom, C., Gibson, G.M., Padgett, M.J. and Skeldon, K.D. (2007) Portable optical spectroscopy for accurate analysis of ethane in exhaled breath. *Meas. Sci. Technol.* 18, 1459-1464.

Petrov, K.P., Waltman, S., Dlugokencky, E.J., Arbore, M., Fejer, M.M., Tittel, F.K. and Hollberg, L.W. (1997) Precise measurement of methane in air using diode-pumped 3.4- μ m difference-frequency generation in PPLN. *Applied Physics B-Lasers and Optics* 64, 567-572.

Ramaswamy, V., Boucher, O., Haigh, J., Hauglustine, D., Haywood, J., Myhre, G., Nakajima, T., Shi, G., Solomon, S. (2001) Radiative forcing of climate. *Climate Change*, 349-416.

Richter, D., Lancaster, D.G., Curl, R.F., Neu, W. and Tittel, F.K. (1998) Compact mid-infrared trace gas sensor based on difference-frequency generation of two diode lasers in periodically poled LiNbO₃. *Applied Physics B-Lasers and Optics* 67, 347-350.

Romanini, D., Kachanov, A.A., Sadeghi, N. and Stoeckel, F. (1997) CW cavity ring down spectroscopy. *Chemical Physics Letters* 264, 316-322.

Schoell, M. (1980) THE HYDROGEN AND CARBON ISOTOPIC COMPOSITION OF METHANE FROM NATURAL GASES OF VARIOUS ORIGINS. *Geochim. Cosmochim. Acta* 44, 649-661.

Schoell, M. (1983) GENETIC-CHARACTERIZATION OF NATURAL GASES. *AAPG Bull.-Am. Assoc. Petr. Geol.* 67, 2225-2238.

Solomon, S., Qin, D., Manning, M., Chen, Z., Marquis, M., Averyt, K.B., Tignor, M. and Miller, H.L. (2007) *Climate Change 2007: The Physical Science Basis. Contribution of Working Group*

I to the Fourth Assessment Report of the Intergovernmental Panel on Climate Change. Cambridge University Press. Cambridge, United Kingdom, 996.

Sonnenfroh, D.M., Wainner, R.T., Allen, M.G. and Varner, R.K. (2010) Interband cascade laser-based sensor for ambient CH₄. *Opt. Eng.* 49, 10.

Stocker, T.F., Qin, D., Plattner, G.-K., M. Tignor, S.K. Allen, J. Boschung, A. Nauels, Y. Xia, Bex, V. and Midgley, P.M. (2013) *Climate Change 2013: The Physical Science Basis. Contribution of Working Group I to the Fifth Assessment Report of the Intergovernmental Panel on Climate Change.* Cambridge University Press, Cambridge, United Kingdom and New York, NY, USA, 1535.

Thauer, R.K. (1998) Biochemistry of methanogenesis: a tribute to Marjory Stephenson. *Microbiology-Uk* 144, 2377-2406.

von Basum, G., Halmer, D., Hering, P., Murtz, M., Schiller, S., Muller, F., Popp, A. and Kuhnemann, F. (2004) Parts per trillion sensitivity for ethane in air with an optical parametric oscillator cavity leak-out spectrometer. *Opt. Lett.* 29, 797-799.

Vurgaftman, I., Kim, M., Kim, C.S., Bewley, W.W., Canedy, C.L., Lindle, J.R., Abell, J. and Meyer, J.R. (2010) Challenges for mid-IR interband cascade lasers, in: Belyanin, A.A., Snowton, P.M. (Eds.), *Novel in-Plane Semiconductor Lasers IX.* Spie-Int Soc Optical Engineering, Bellingham.

Whiticar, M.J. (1999) Carbon and hydrogen isotope systematics of bacterial formation and oxidation of methane. *Chem. Geol.* 161, 291-314.

Wuebbles, D.J., Hayhoe, K. (2002) Atmospheric methane and global change. *EarthScience Reviews* 57, 177-210.

Wysocki, G., Bakhirkin, Y., So, S., Tittel, F.K., Hill, C.J., Yang, R.Q. and Fraser, M.P. (2007) Dual interband cascade laser based trace-gas sensor for environmental monitoring. *Appl. Optics* 46, 8202-8210.

Yacovitch, T.I., Herndon, S.C., Roscioli, J.R., Floerchinger, C., McGovern, R.M., Agnese, M., Petron, G., Kofler, J., Sweeney, C., Karion, A., Conley, S.A., Kort, E.A., Nahle, L., Fischer, M., Hildebrandt, L., Koeth, J., McManus, J.B., Nelson, D.D., Zahniser, M.S. and Kolb, C.E. (2014) Demonstration of an Ethane Spectrometer for Methane Source Identification. *Environ. Sci. Technol.* 48, 8028-8034.

Ye, W.L., Li, C.G., Zheng, C.T., Sanchez, N.P., Gluszek, A.K., Hudzikowski, A.J., Dong, L., Griffin, R.J. and Tittel, F.K. (2016) Mid-infrared dual-gas sensor for simultaneous detection of methane and ethane using a single continuous-wave interband cascade laser. *Opt. Express* 24, 16973-16985.

Zalicki, P. and Zare, R.N. (1995) CAVITY RING-DOWN SPECTROSCOPY FOR QUANTITATIVE ABSORPTION-MEASUREMENTS. *J. Chem. Phys.* 102, 2708-2717.

Zhao, Y., Strong, K., Kondo, Y., Koike, M., Matsumi, Y., Irie, H., Rinsland, C.P., Jones, N.B., Suzuki, K., Nakajima, H., Nakane, H. and Murata, I. (2002) Spectroscopic measurements of tropospheric CO, C₂H₆, C₂H₂, and HCN in northern Japan. *Journal of Geophysical Research-Atmospheres* 107.

Figures and Tables

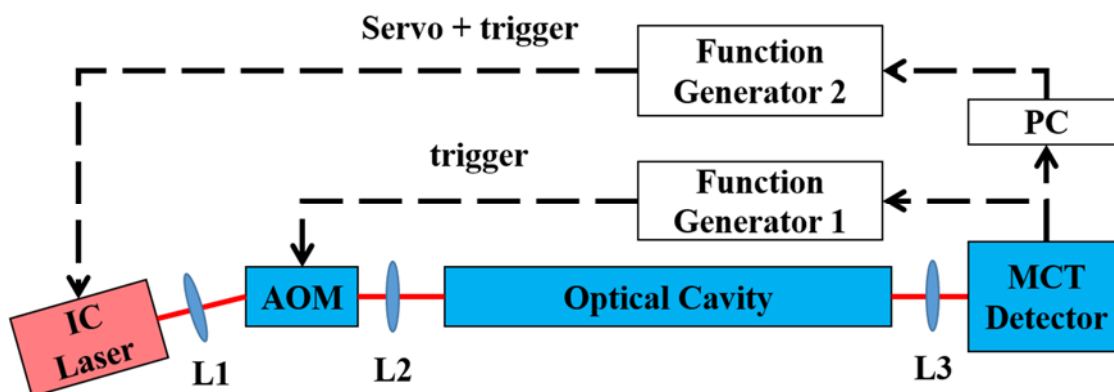


Figure 2.1. Schematic of the cavity ring-down spectrometer for the atmospheric ethane measurements. The instrument is comprised of a interband cascade laser (ICL), an acousto-optic modulator (AOM), lenses (L1 – L3), the optical cavity, a thermal electrically cooled mercury cadmium telluride (MCT) detector, 2 function generators, and a personal computer (PC). Signal from function generator 1 is triggered by the transmitted signal from the MCT detector and controls the fast optical switching of AOM. The PC digitizes and fits the cavity decays and controls the laser servo and frequency adjustments through function generator 2.

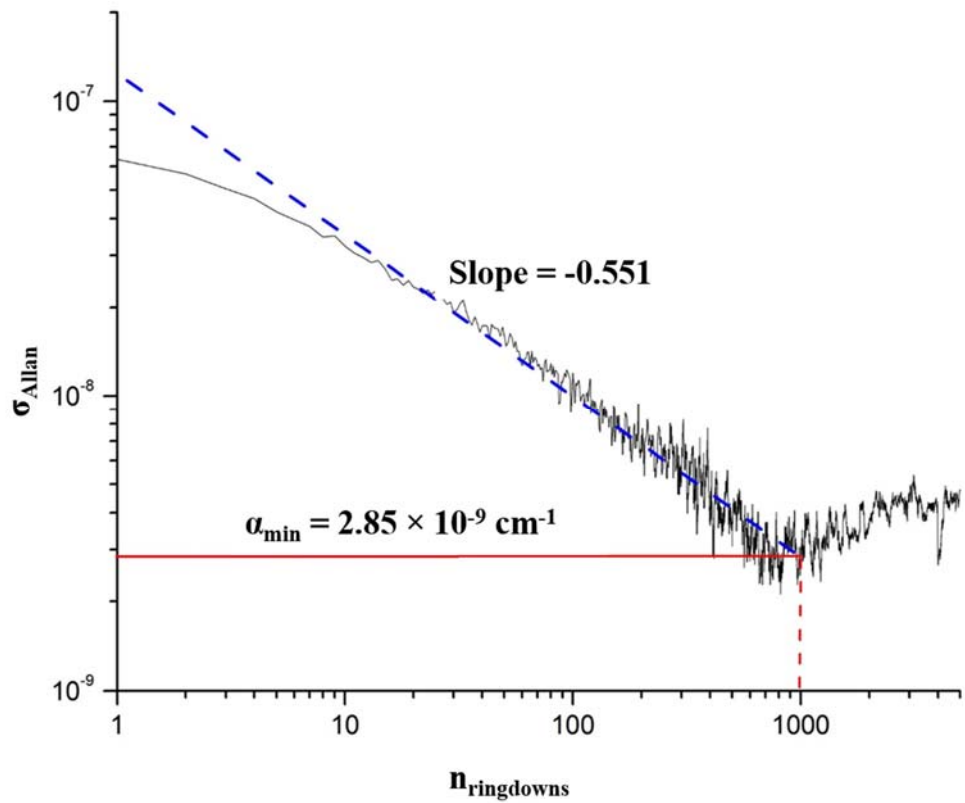


Figure 2.2. Allan deviation plot for the ringdown decays of vacuum baseline losses at 2976.788 cm^{-1} . The acquisition rate is ~ 20 Hz with the estimated minimum detectable absorbance of the spectrometer as $2.85 \times 10^{-9} \text{ cm}^{-1}$.

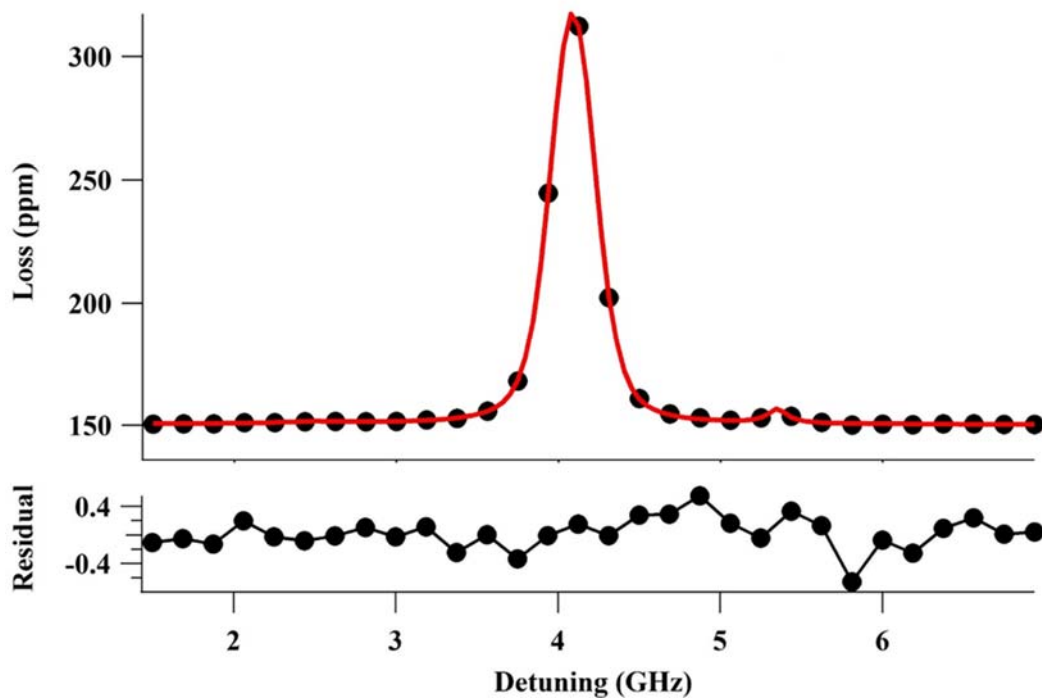


Fig 2.3. Spectrum measured of a 50 ppb methane sample diluted in 30 Torr zero air with transition centered at 2978.644 cm^{-1} . In the upper panel, the measured data are shown as black dots and the galatry profile fit is shown in red solid line. In the bottom panel, the connected black dots shown the residual between the data and the fit. The signal to noise ratio of the fit for the spectral fit, defined as the peak absorption divided by the RMS of the residual, is reported to be $\sim 720 : 1$.

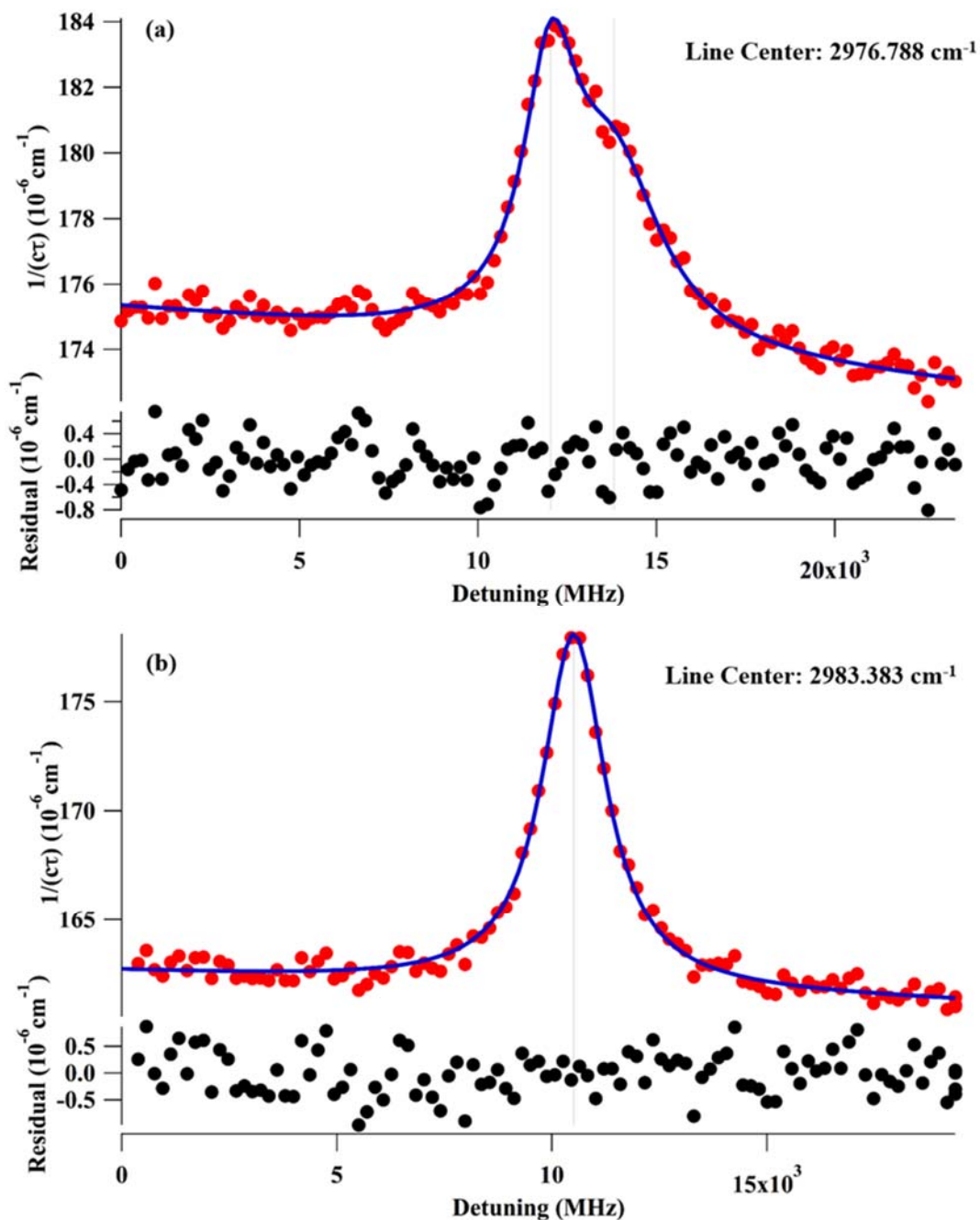


Figure 2.4. Spectra measured with a ~ 10 ppb ethane in 250 Torr zero air. (a) The 2976.788 cm^{-1} band was measured between 2976.30 cm^{-1} and 2977.30 cm^{-1} with the spectrum fitted as a sum of two Voigt profiles with a linear baseline. The signal to noise ratio (SNR) of the fit was $\sim 24:1$. (b) The 2983.383 cm^{-1} was measured between 2983.05 cm^{-1} and 2983.70 cm^{-1} and fitted with a single Voigt profile. The reported SNR of this spectrum was $\sim 42:1$.

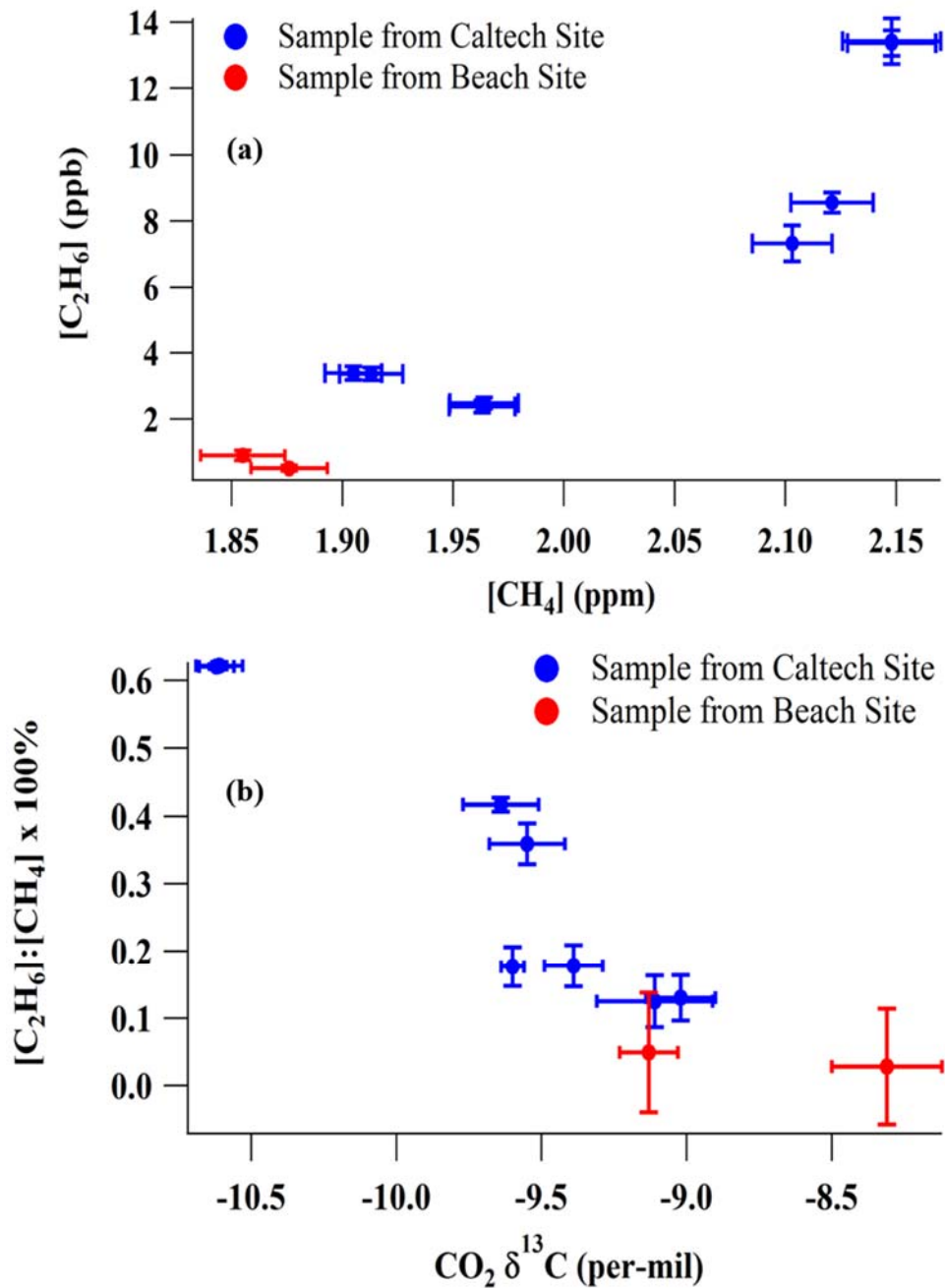


Figure 2.5. Results from measurements of 10 ambient air samples, including 8 of the Caltech site samples and 2 of the beach site (PV site) samples. (a) Ethane abundance as a function of methane. (b) Ethane to methane ratio as a function of the isotope content of the carbon dioxide in the same sample.

Calibration Number	Ethane from 2976.788 cm⁻¹	Ethane from 2983.383 cm⁻¹	Methane from CRDS	Methane from Picarro
1	9.95	10.88	2.131	2.112
2	9.84	10.80	2.125	2.114
3	9.93	10.85	2.133	2.113

Table 2.1: Results from the ethane accuracy calibration experiment. Ethane and methane from CRDS measurements were performed using the instrument described in this work. Methane abundance of each measurement was calibrated with a Picarro instrument, which was standardized with a known NOAA trace gas standard.

Site Location	Sample ID	CO₂ (ppm)	δ¹³C of CO₂ (‰)	CH₄ (ppm)	C₂H₆ (ppb)
Caltech	1	426.56 ± 0.03	-9.64 ± 0.13	2.055 ± 0.004	8.56 ± 0.03
Caltech	2	428.25 ± 0.02	-9.55 ± 0.13	2.041 ± 0.003	7.33 ± 0.05
Caltech	3	417.08 ± 0.01	-9.02 ± 0.12	1.903 ± 0.002	2.48 ± 0.02
Caltech	4	417.67 ± 0.03	-9.11 ± 0.20	1.905 ± 0.004	2.38 ± 0.02
Caltech	5	462.27 ± 0.04	-10.62 ± 0.06	2.154 ± 0.005	13.37 ± 0.04
Caltech	6	461.80 ± 0.03	-10.61 ± 0.08	2.159 ± 0.004	13.42 ± 0.07
Caltech	7	417.72 ± 0.02	-9.60 ± 0.04	1.903 ± 0.003	3.36 ± 0.02
Caltech	8	417.85 ± 0.02	-9.39 ± 0.10	1.902 ± 0.004	3.38 ± 0.02
PV	1	399.73 ± 0.10	-8.31 ± 0.19	1.864 ± 0.005	0.52 ± 0.01
PV	2	405.70 ± 0.04	-9.13 ± 0.10	1.830 ± 0.004	0.90 ± 0.01

Table 2.2. Results from the ambient air flask sample measurements. Measurements of CO₂, δ¹³CO₂, and CH₄ were obtained with the Picarro trace molecule analyzer. Measurements of C₂H₆ came from the average of the spectra collected in the spectral window reported in this work.

Supporting Information

Laser Linewidth Measurement

The IC laser used for these measurements were manufactured by the JPL Micro-devices laboratory. As part of the laser characterization, it is important to measure the linewidth of the laser to ensure that it is much smaller than that of the cavity modes. In order to measure the laser linewidth, a heterodyne beat note measurement was conducted with two IC lasers with overlapping lasing frequencies (Fig. S2.1). To set up a beat note experiment, the two lasers have to be spatially overlapped at the photodetector and have optical frequencies close to each other to have a beat note signal within the detector bandwidth. Since the laser beams are in the mid-IR range, spatial overlapping of these lasers can become challenging to achieve. Both of the MIR lasers were then co-aligned with a visible laser (633 nm DBR laser from Eagleyard Photonics) beam with the use of a dichroic mirror (reflect 633 nm and transmit 3.3 μm) to simplify the alignment process. The four laser beams were then combined with a pellicle beam splitter centered at 3.36 μm before entering the detector. The detector signal was first sent through a low pass filter (BBLP-30+) and a bias tee (ZFBT-492GW+) to get rid of higher harmonics and the DC component in the signal before amplified (ZFL-500LN+) and observed on an oscilloscope. The beat note signal was maximized by optimizing the co-alignment of the two lasers and fine tuning of the laser frequencies. Average of 16 scans over 2 minutes were recorded to obtain Fig. S2.2, with 128 traces per scan. The measurement time was limited to 2 minutes because long time fluctuation of the laser frequency becomes significant after this time. The data was fitted to a Voigt profile with the full-width at half maximum (FWHM) of 6.06 MHz. Since the observed linewidth is a convolution of both lasers, it is not possible to determine the linewidth of one

without the knowledge of the other. Assuming the two lasers have similar linewidths, the estimated linewidth of the laser used for the reported laser is $\sim 3\text{MHz}$.

Beam Profile Measurement

In order for efficient coupling and maximum transmission of the laser beam through the high-finesse cavity, the beam needs to be mostly Gaussian and the Gaussian beam TEM₀₀ mode waist and curvature needs to match the location and size of the cavity beam waist and curvature. The mathematical derivation of the complex Gaussian beam parameter has been described in details by previous students from our group. A simple approach to measure the laser beam shape is to utilize a commercially available beam profiler, which provides a real time image of the beam. Prior to injecting into the cavity, the laser beam needs to be well collimated, aligned through the AOM, and mode matched to the cavity beam with additional mode matching lens. The beam profile after initial collimation and the AOM are reported below from measurements using the Ophir-Spiricon Pyrocam III. Figure S2.3 shows the beam profile after initial collimation taken 57 inches away from the laser. The top and bottom images are the 2D (XY) and 3D (XYZ) beam profile images, with Z dimension as the beam intensity. The beam profile of the laser output appears to be very circular, $(X, Y) = (2.16 \text{ mm}, 2.22 \text{ mm})$, and well behaved. The laser beam was then manipulated to be smaller than the active area of the AOM crystal prior to the AOM. With the help of the beam profiler, the intensity of the first order diffracted beam from the AOM was maximized, since the first order beam is the one used for cavity ring-down measurements. Figure S2.4 shows the beam profile after passing through the AOM take 5 inches from the AOM output, with the more intense beam as the first order diffracted beam. As shown in the right panels, the laser beam is distorted to be less circular, $(X, Y) = (0.37 \text{ mm}, 0.25 \text{ mm})$.

Since the distortion is not severe, it did not result in significant intensity loss of transmission through the cavity.

Cavity Length Measurement

In order to retrieve absolute concentration of the observed molecule, it is very important to know the length between the two cavity mirrors (L). For a Fabry-Perot type cavity, which is the one used in this work, the cavity free spectral range (FSR) can be expressed as a function of the speed of light, c , the mirror spacing, L , and the refractive index, n .

$$FSR = \frac{c}{2nL} \quad (\text{Eq S2.1})$$

FSR is the frequency spacing between resonant cavity modes. Thus, laser frequency needs to be on resonance with these cavity modes for transmitted light to be observed. We can take advantage of this property to measure the cavity length by measuring the cavity FSR.

In order to measure the cavity FSR, 81.4 Torr of 50 ppb methane in N₂ sample was measured between 2978.4 cm⁻¹ and 2979.2 cm⁻¹. The spectrum was collected by tuning the laser frequency to be on resonance of each consecutive cavity modes. The result is a spectrum of cavity loss as a function of number of resonances. Since this spectral range covers 4 ¹²CH₄ transitions with known line parameters in the HITRAN database, the spectrum can be fitted to the HITRAN model with the x-axis multiplication factor as the FSR. Figure S2. 5 shows the observed methane spectrum and the fitted HITRAN model. The calculated FSR with this method is 182.5 MHz, yielding the cavity length to be 82.2 cm.

Methane Spectroscopy

Figure S2. 6 shows the integrated area of the ¹²CH₄ (centered at 2978.644cm⁻¹) line intensity of the 50 ppb methane in zero air sample as a function of the total pressure. Line intensities were integrated with a Galatry profile fit mentioned in the main text. The

measurements were done by filling the cavity with 81.9 Torr of 50 ppb methane in zero air and pump down to each desired lower pressure. Measurements were done between 2 Torr and 81.9 Torr with three individual spectra collected at each pressure within 45 min. Ideally, the line intensity should be linear as a function of the total pressure and approaching zero as pressure approaches zero. The black solid line in Fig S2.6 is a linear regression fit of the results from all of the 48 spectra. One can observe that (1) the overall trend of the pressure dependence is linear; (2) the linearity breaks down at low pressure; and (3) the interception of the linear regression line is non-zero. The breakdown of the linearity and the non-zero intercept are results of the fractionation from sample pump out. It was observed that, although methane is relatively volatile, it does appear to have some memory effect during pump out. Thus, the relative abundance of methane increases as the total pressure decreases. When the pump out fractionation is corrected, the $^{12}\text{CH}_4$ line intensity becomes linear as a function of pressure and approaches zero as pressure approaches zero.

Ethane Transition Selection

HITRAN database has shown that within the tuning range of the laser, three different ethane bands could be measured (Fig S2.7). However, not all of these three bands are clear of interferences from other highly abundant molecules in the atmosphere. Among these interferences, the most prominent are interferences from water absorption lines. In the simulated spectra shown in Fig S2.7, the simulation conditions for the different molecules are 5 ppb ethane, 5 ppb methane, and 20 ppm water in 230 Torr air sample. Although both the water and methane abundances are much lower than those of in the atmosphere (~ 2 ppm methane and $\sim 0.6\%$ assuming 20% RH at 25 °C), one can observe that the interference of water to the ethane band center around 2980.07 cm^{-1} is not negligible. Drying agents and cold bathes were used to strip

the water from samples. The water abundance can only be decreased to ~ 10 ppm, which is still significant enough to retrieve precise ethane measurements with the 2980.07 cm^{-1} transition, shown in Fig S2.8. As for the case of the interference of methane transitions with the band centered around 2976.788 cm^{-1} , the interferences were much smaller and not directly overlapping. Also, since the line parameters of methane absorption lines in this region are well known, we can subtract methane absorptions in the 2976.788 cm^{-1} band scanning range by integrating individual known methane transitions. Thus, the bands centered at 2976.788 cm^{-1} and 2983.38 cm^{-1} were used for ethane concentration retrieval.

Reproducibility of Ethane Measurements

As mentioned in the main text, the two targeted ethane spectral were measured back and forth for 6 times within 12 hours to demonstrate the reproducibility of the spectrometer. Figure S2.9 shows the statistics of the integrated area of the two spectral windows. The standard error for both sets of measurements were reported. The error bar of each measurement arises from the error reported in individual area integration.

Figures

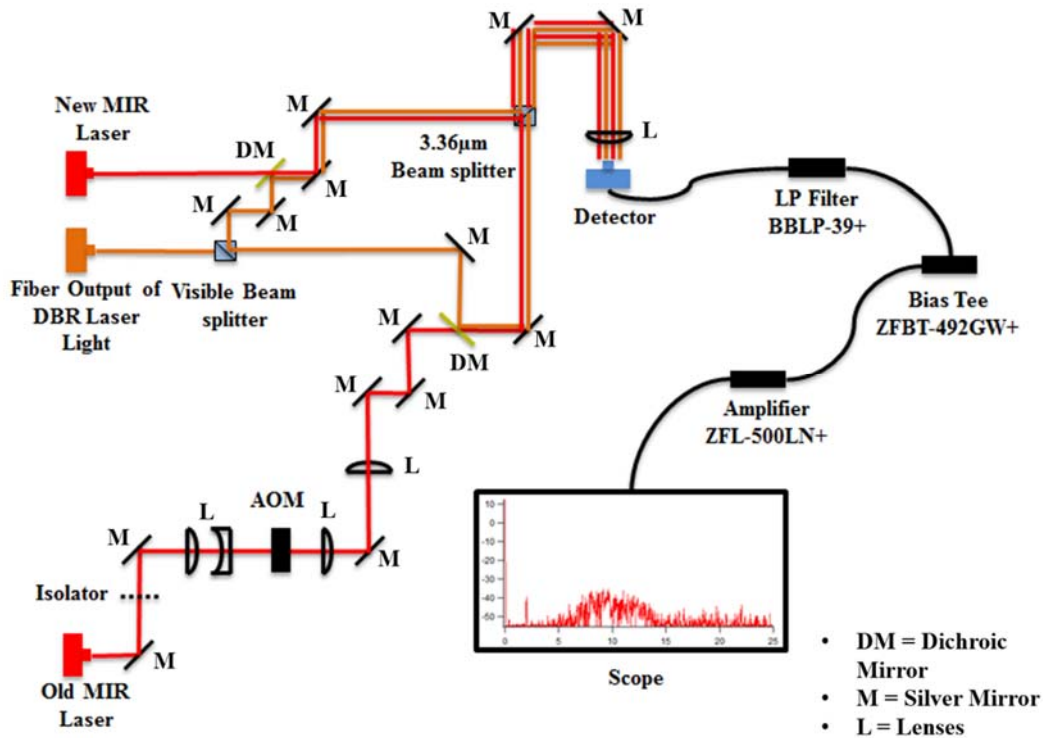


Figure S2.1. Schematic of the experimental set-up of the beat note experiment for the mid-IR laser linewidth measurement. The two MIR lasers used were both manufactured by the JPL microdevices laboratory. Old MIR laser serial number: NRL30_4A_19-20_61. New MIR Laser serial number: NRL30_4A_19-20_56. The visible beam (orange beam) is from a 633 nm DBR laser, which was coupled into an optical fiber. The dichroic mirrors used reflects the red light and is AR coated for the 3.3 μm MIR light. The detector used was the Vigo 4TE cooled MCT detector peaking at 3.4 μm.

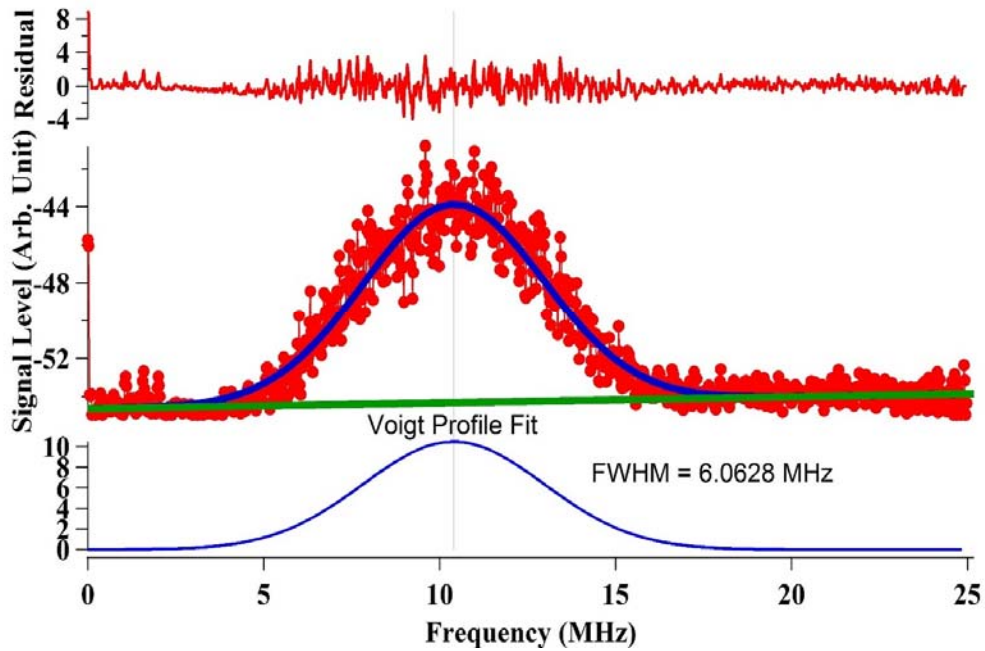


Figure S2.2. Beat note measurement of the MIR IC laser linewidth. The profile is an average of 16 scans over 2 min, with an average of 128 traces per scan. The observed line profile was fitted with a Voigt profile with a linear baseline. In the middle panel, the red connected dots are the data, the blue trace is the overall fit, the green trace is the linear baseline. The top panel is the fit residual, the bottom panel is the fitted Voigt profile. The full width at half maximum of the fitted Voigt profile is 6.06 MHz. Assuming the two laser have the same linewidth, the linewidth of individual laser is ~ 3 MHz.

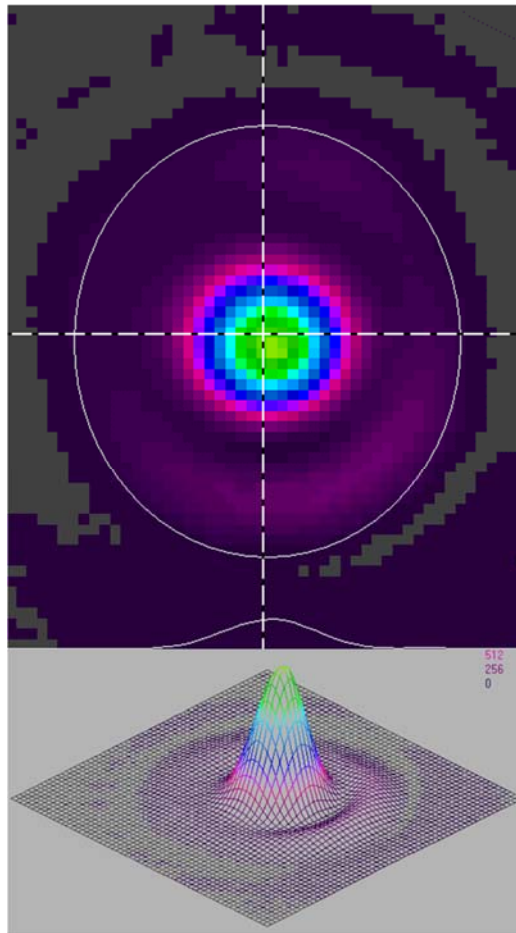


Figure S2.3. Beam profile of the collimated laser beam measured 57 inches away from the laser, with only an anti-reflective (AR) coated aspheric lens (Lightpath 390036-IR4) with a focal length of 3.05 mm. The beam diameters in the X and Y dimensions are 2.16 mm and 2.22 mm, respectively

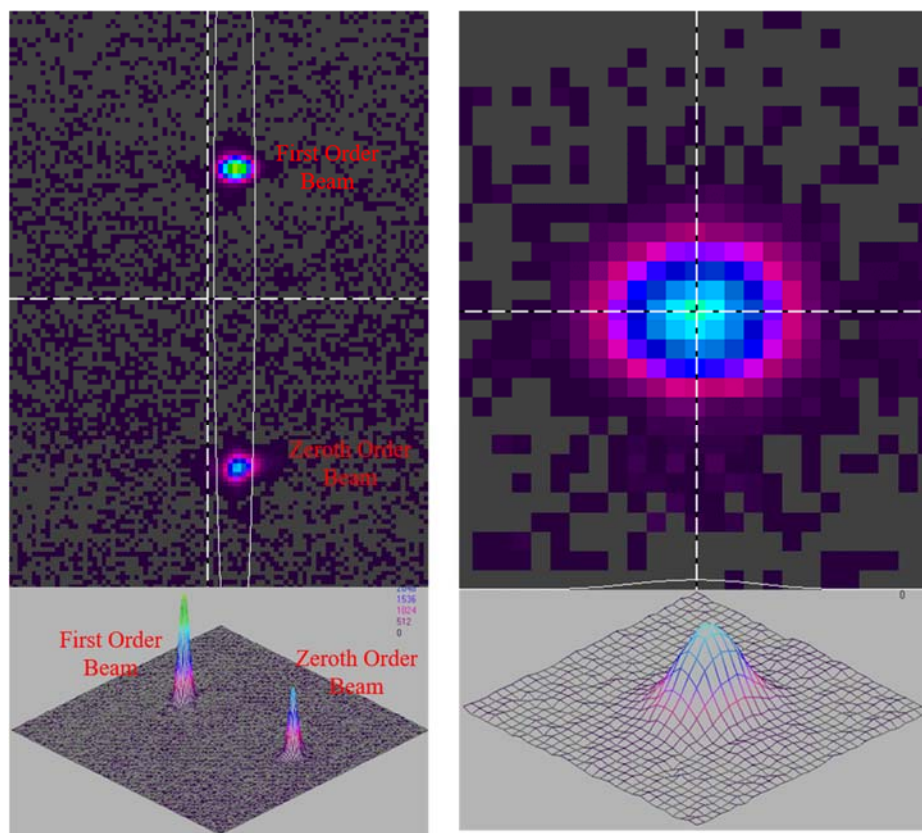


Figure S2.4. Beam profile of the beams through the AOM measured 5 inches away from the AOM output. The left panels include both the zeroth order (transmitted) and the first order diffracted beam, with the more intense beam as the first order beam. The right panels are the zoomed in observation of the first order beam. The beam diameters in the X and Y dimensions are 0.37 mm and 0.25 mm, respectively.

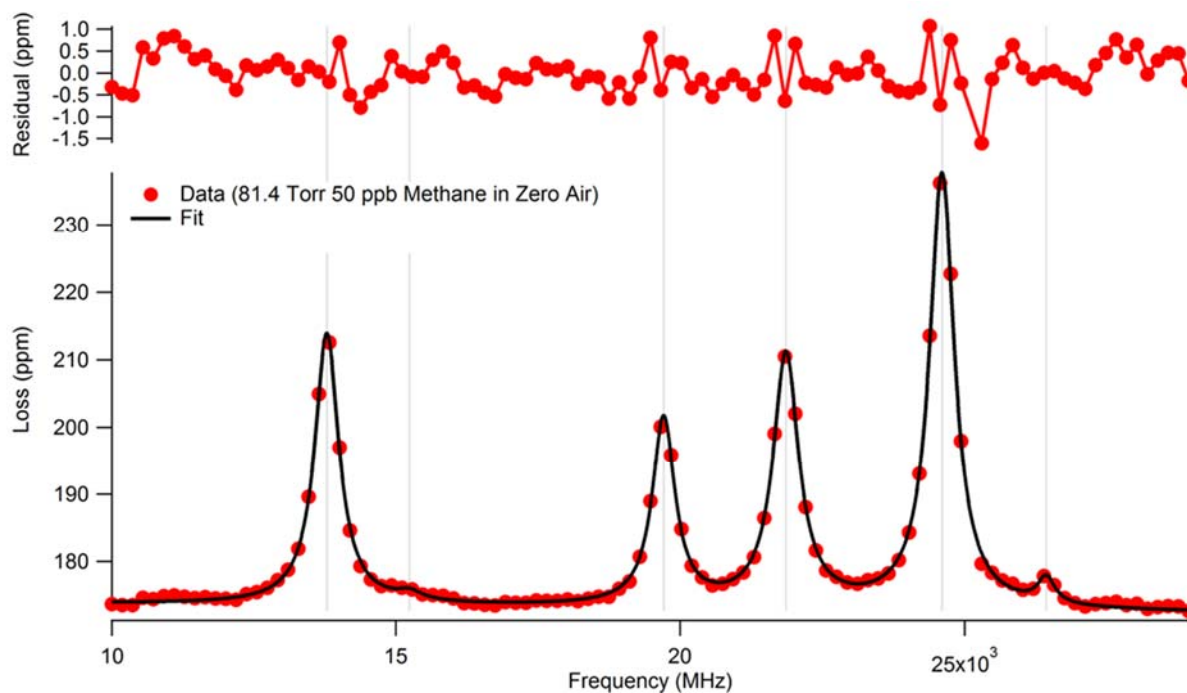


Figure S2.5. Measurement of 50 ppb methane between 2978.4 cm^{-1} and 2979.2 cm^{-1} . Total pressure of the cavity was 81.4 Torr. The cavity FSR was varied to fit the data (red dots) to the HITRAN simulated spectrum (black trace). The top panel is the residual between the data and the fit. The calculated FSR is 182.5 MHz, resulting in a calculated cavity length of 82.2 cm.

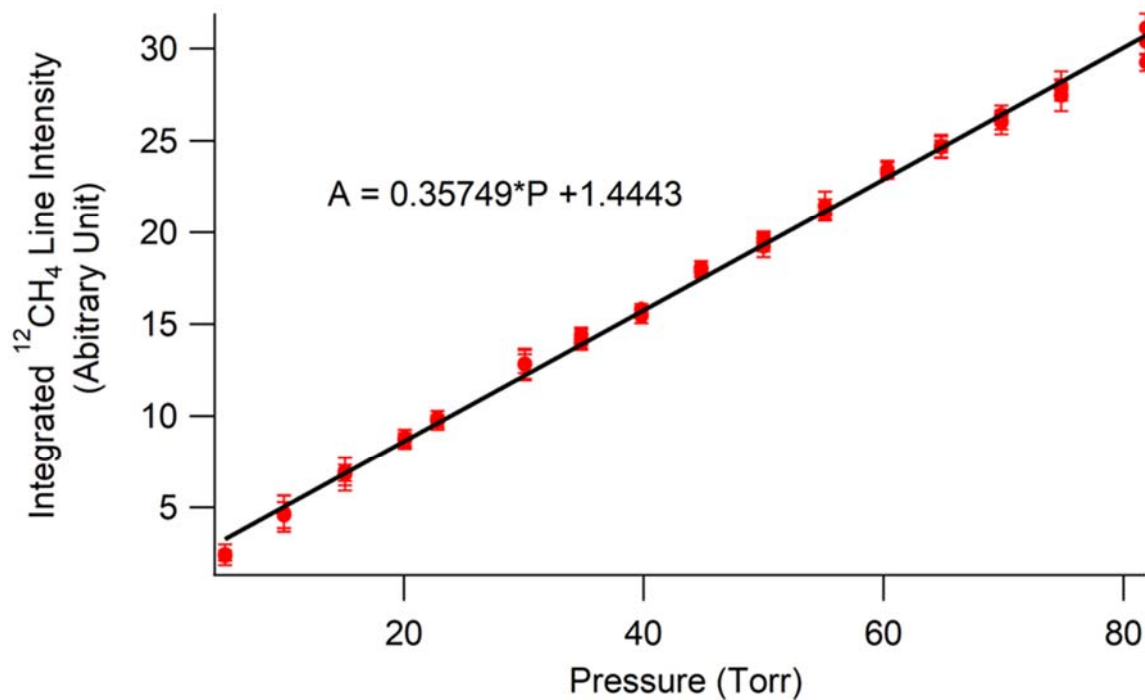


Figure S2.6. Pressure dependence of the integrate ¹²CH₄ line intensity from measurements done with a 50 ppb methane in zero air sample. Measurements were done between 2 Torr and 81.9 Torr with 3 measurements at each pressure. The red dots are the data and the black solid line is a linear regression fit of the area as a function of pressure. One can observe that the linear dependence holds at higher pressures but breaks down at pressures lower than 20 Torr. Also, the intercept of the linear fit is non-zero. This is due to the fractionation of the sample from pumping down to the desired measurement pressures. This can be corrected by calculating the fractionation factor at each pressure. Once corrected, the integrated line intensity becomes linearly dependent to the total pressure, which corresponds to the molecular density of methane, with zero intercept.

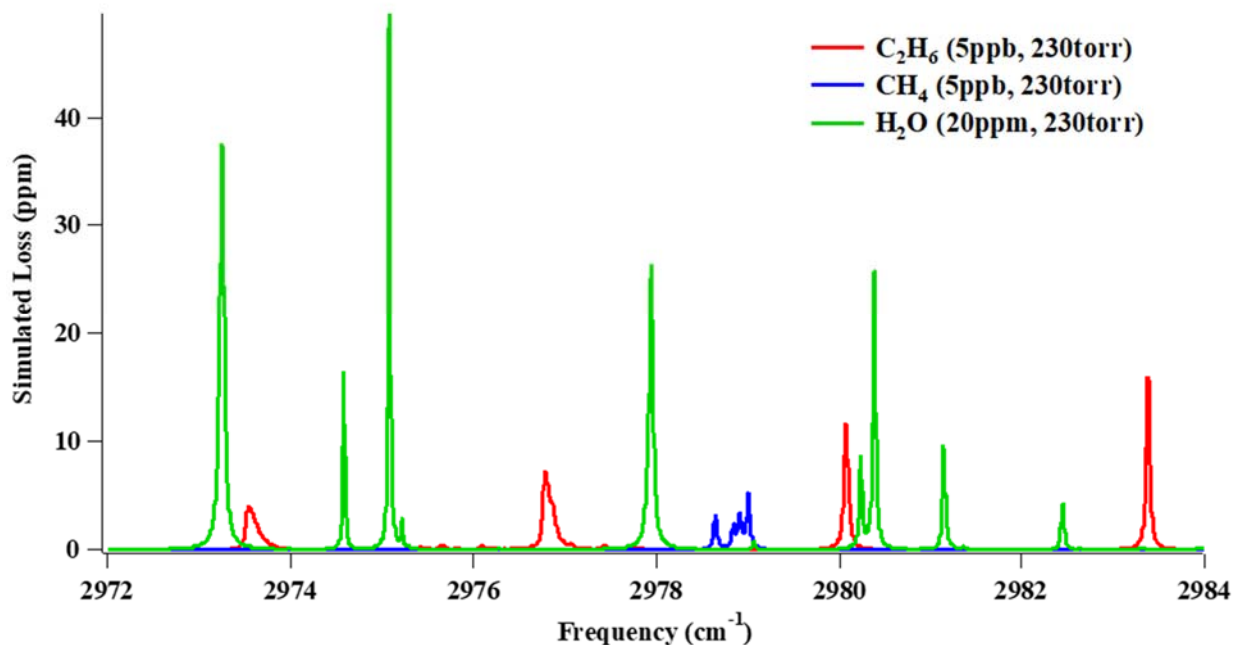


Figure S2.7. HITRAN simulation of spectral lines of ethane, methane, and water in the tuning range of the laser. The simulation conditions were 5 ppb C₂H₆, 5 ppb CH₄, and 20 ppm H₂O in 230 Torr air. These simulations shown that although the tuning range of the laser covers 3 intense absorption bands of the ethane molecule, only two of them, the bands centered at 2976.788 cm⁻¹ and 2983.38 cm⁻¹, could be used for ethane concentration retrieval due to large water interferences in this spectral window.

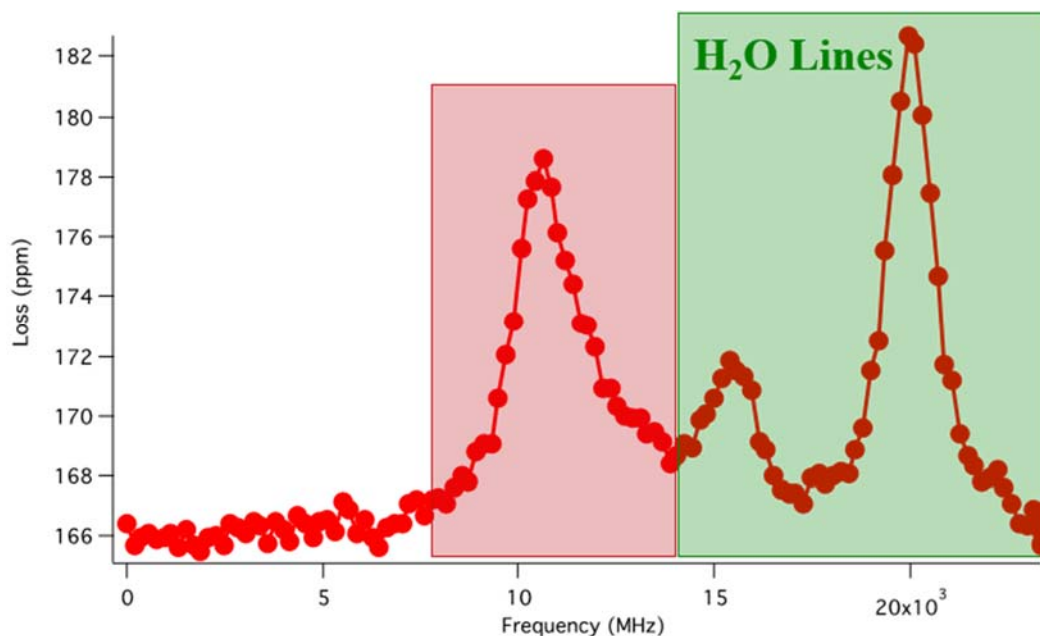


Figure S2.8. Spectrum of a ~ 6 ppb ethane in 250 Torr zero air sample scanned between 2979.67 cm^{-1} and 2980.47 cm^{-1} . Air sample used for this spectrum went through a drying unit packed with $\text{Mg}(\text{ClO}_4)_2$ before entering the cavity to strip off as much water as possible. This spectrum demonstrates that, even after sample draying process, water interference in the scanning window of the 2980.07 cm^{-1} band is not negligible. Thus, this band is not suitable for atmospheric ethane concentration retrieval.

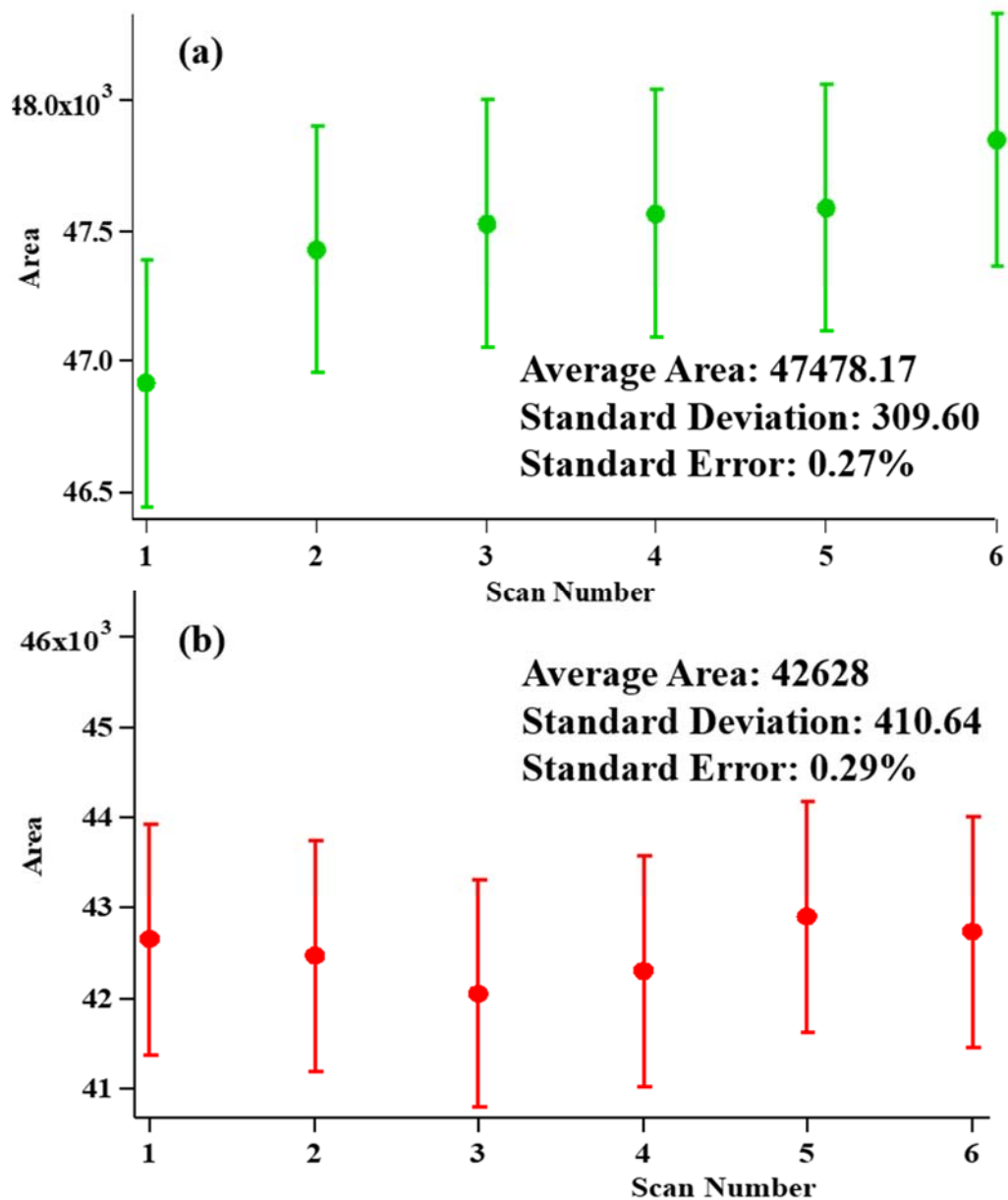


Figure S2.9. Statistics of the integrated area of the two spectral windows (a) centered at 2976.788 cm^{-1} and (b) centered at 2983.383 cm^{-1} . Results came from 12 hours of measurements of the $\sim 10 \text{ ppb}$ ethane in 150 Torr zero air sample. The standard error for both sets of measurements were reported as the standard deviation divided by the square root of the scan number. The error bar of each measurement arises from the error reported in individual area integration.

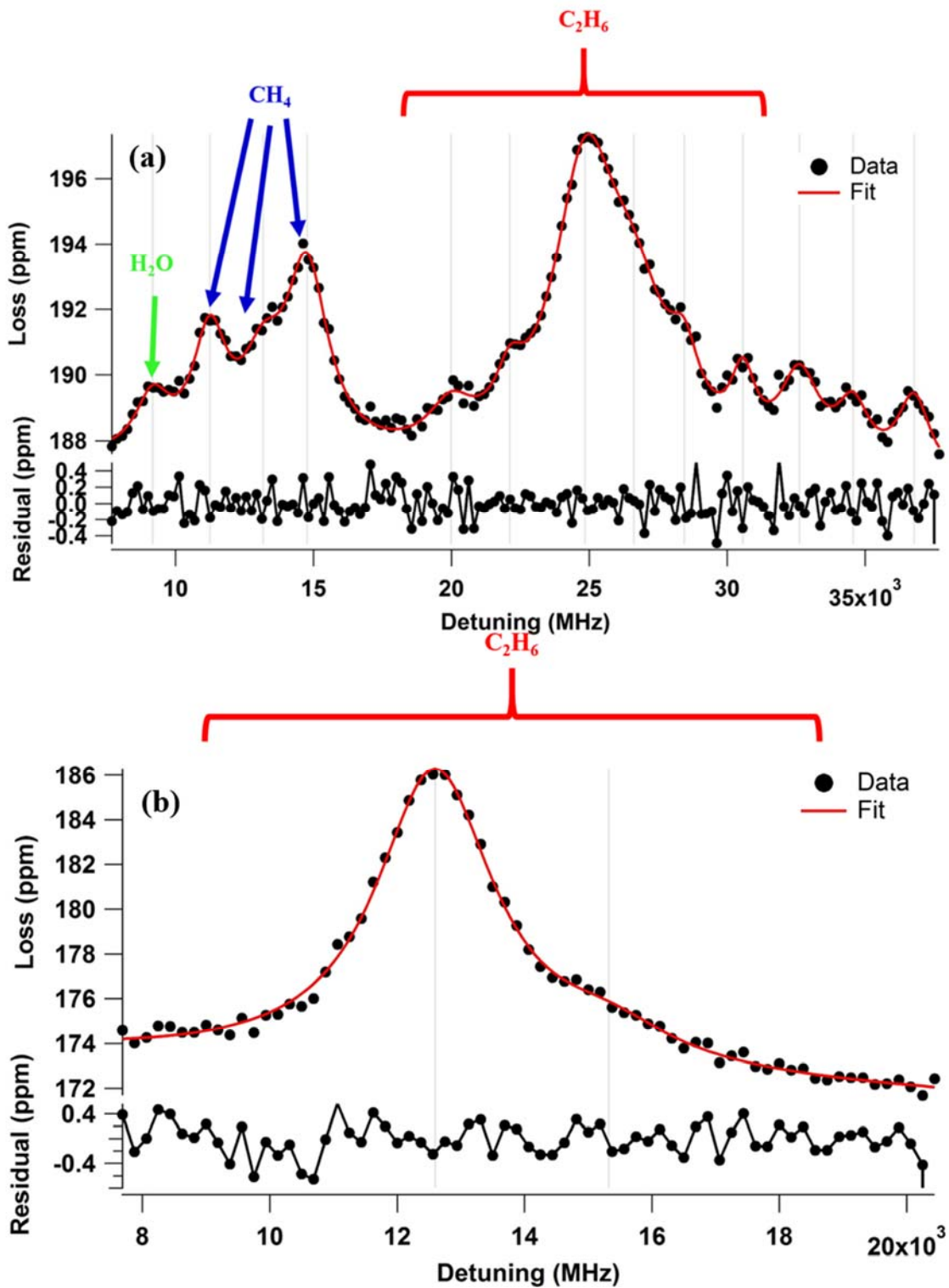


Figure S2.10. Sample spectra of ambient air sample measurements.

Instrument Pictures and CAD Drawings

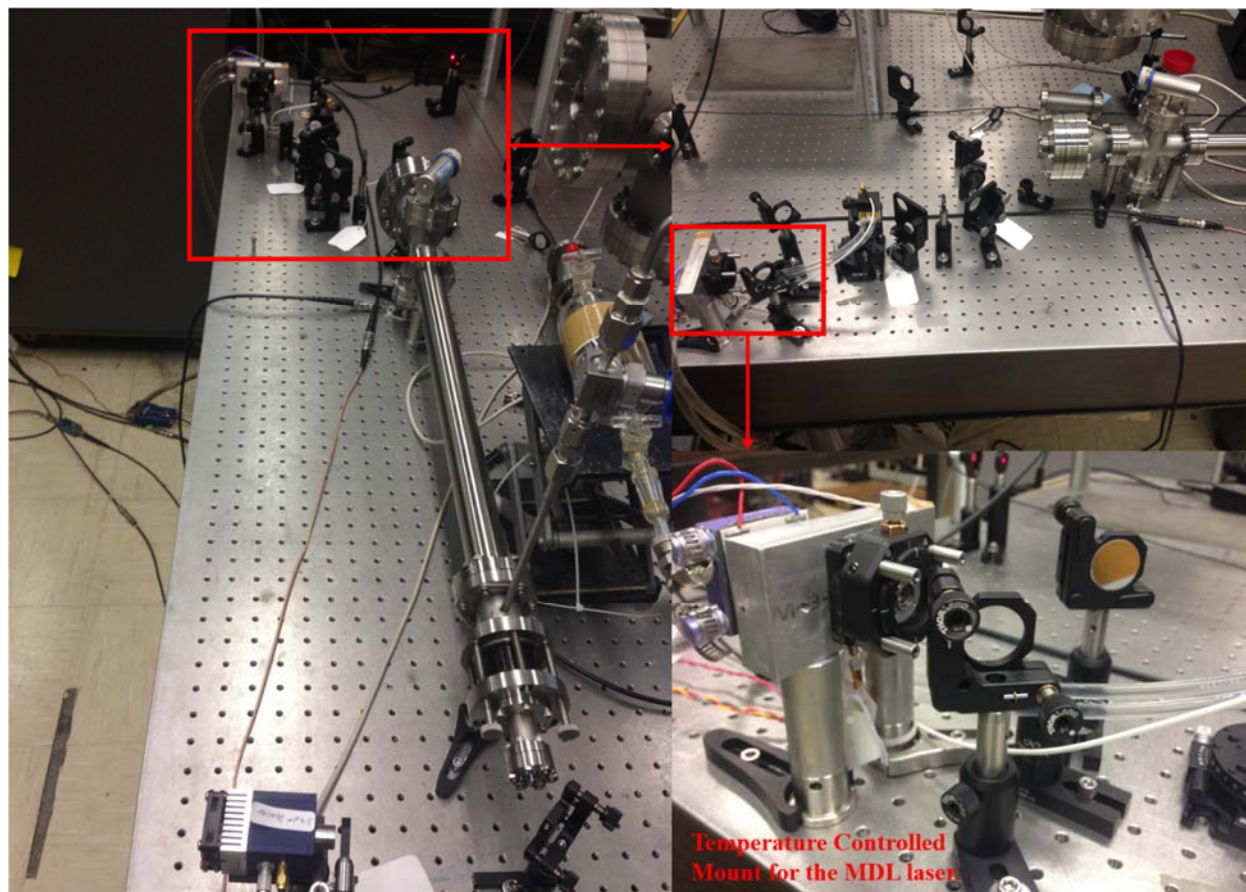


Figure S2.11. Picture of the CRDS cavity spectrometer and the zoomed in view of the temperature controlled ICL mount.

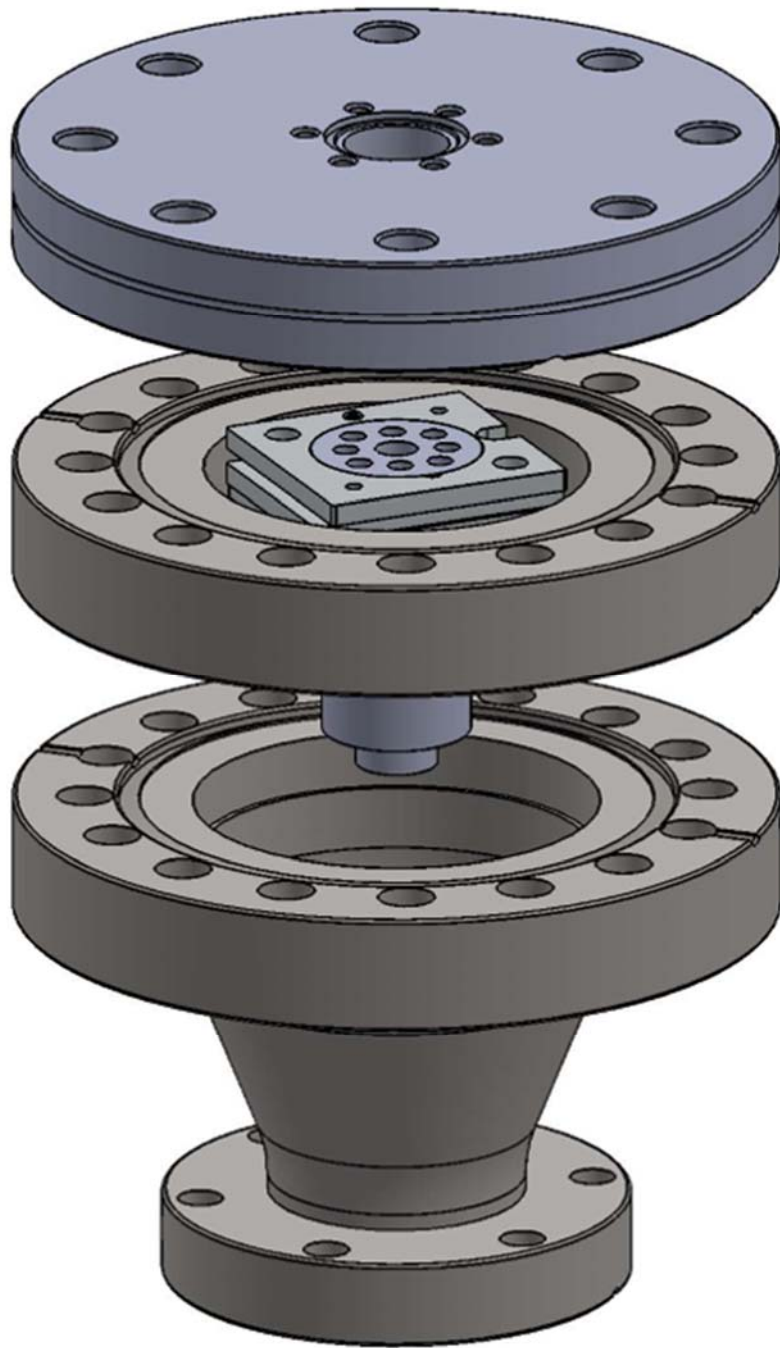


Figure S2.12. Laser side ring-down mirror mount detail.

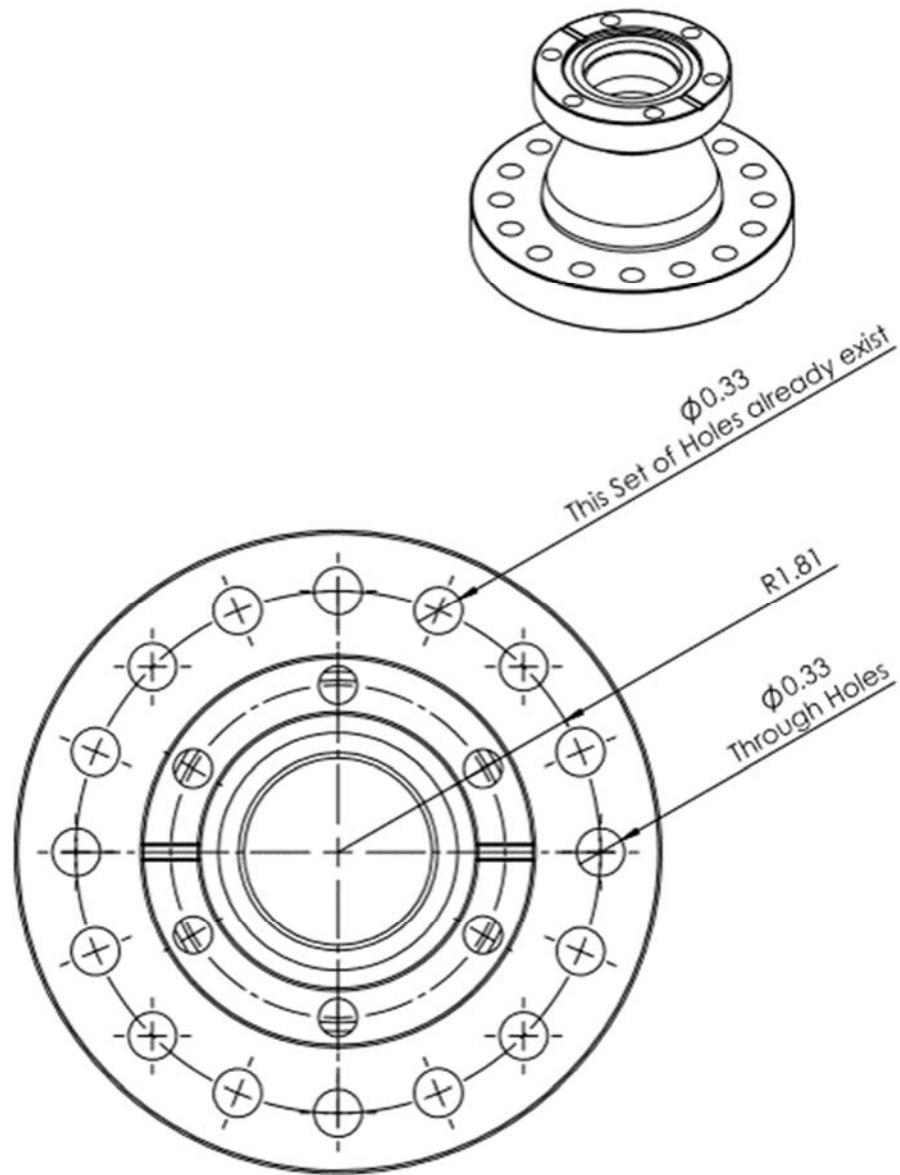


Figure S2.13. Modified 2.75 inch CF to 4.5 inch CF conical reducer detail.

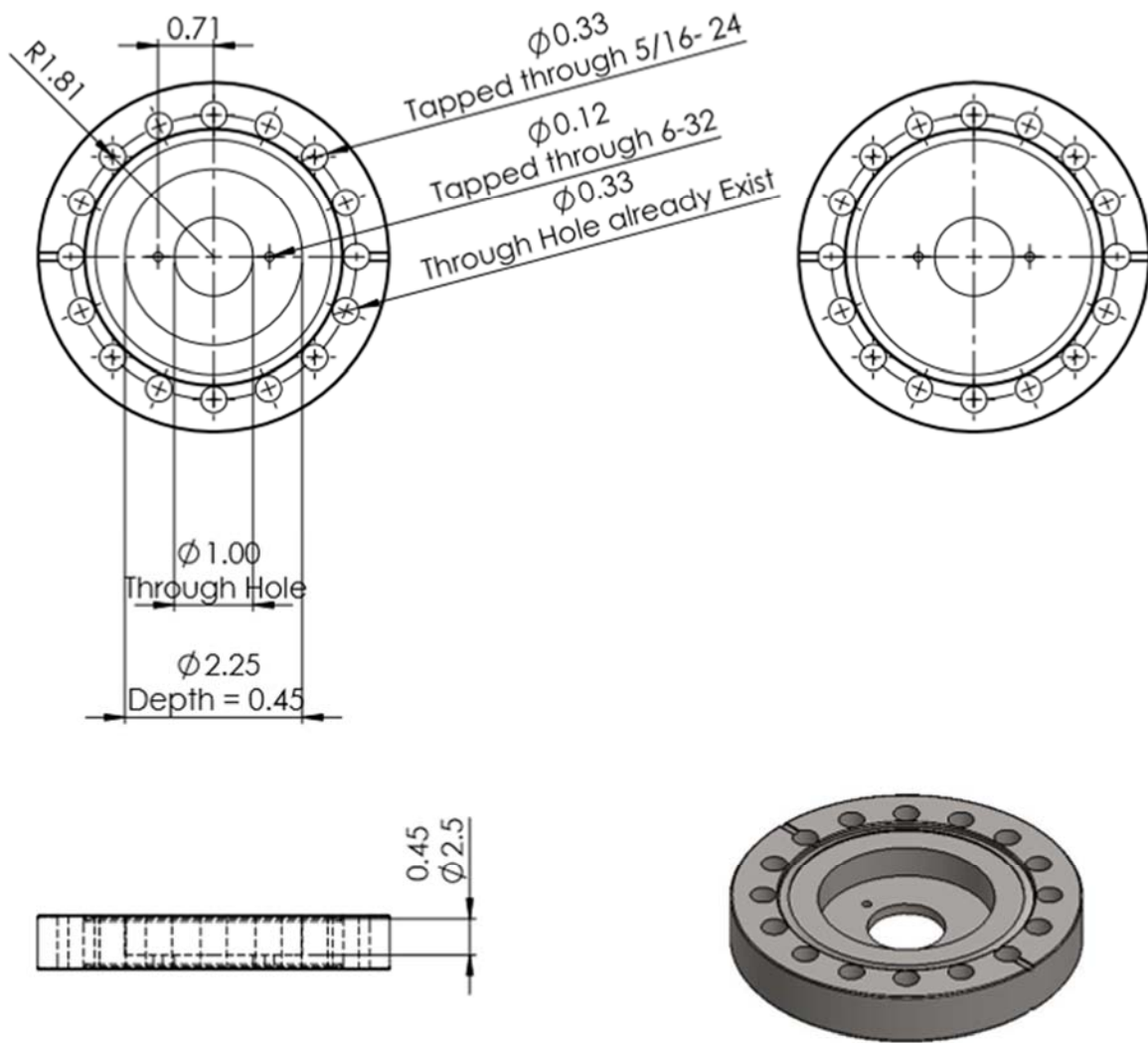


Figure S2.14. Modified 4.5 inch double sided flange for flexure mount mounting.

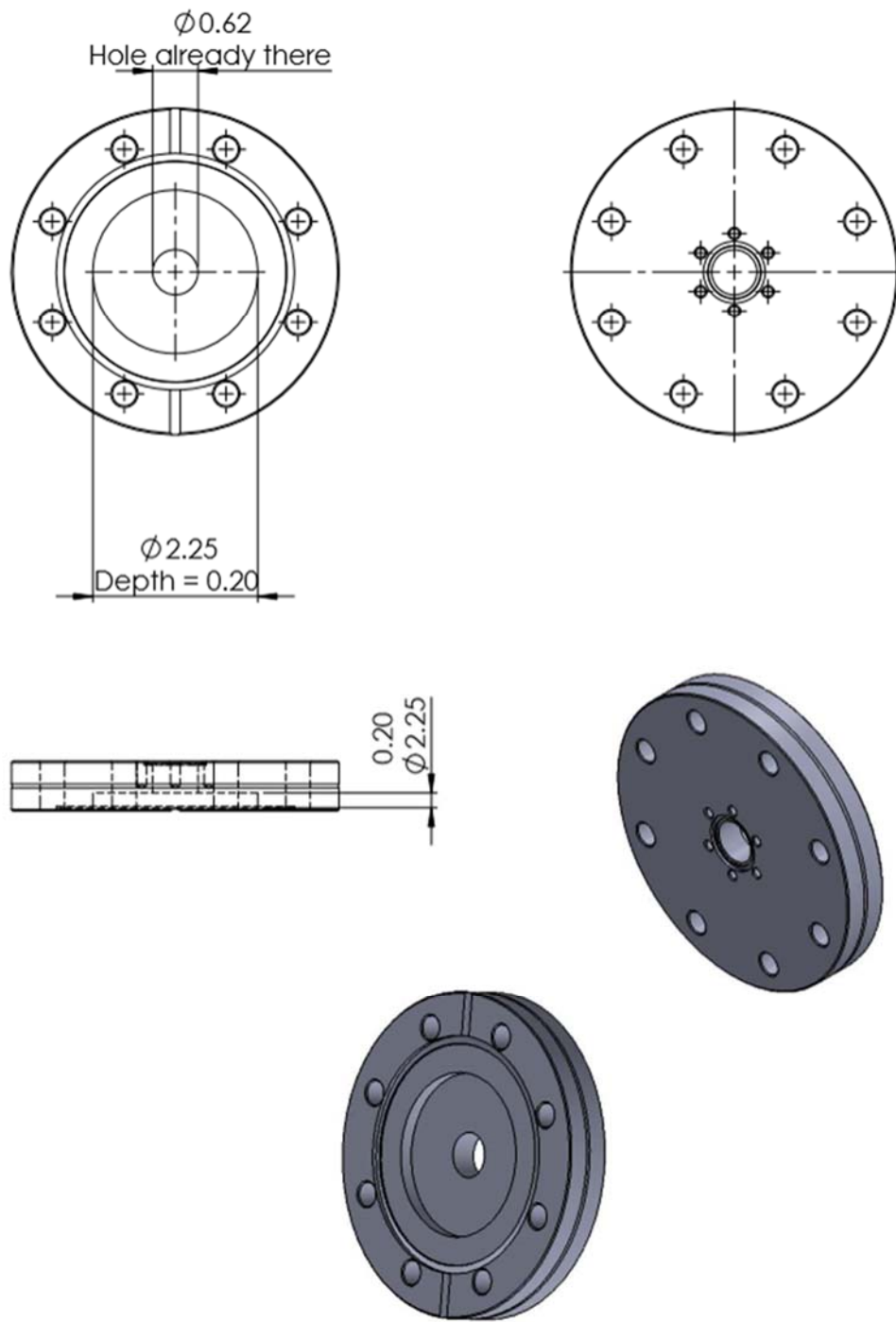


Figure S2.15. Modified zero length 4.5 inch CF to 1 inch reducer.

Material: SS 304

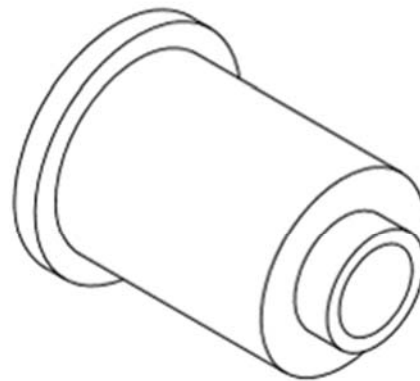
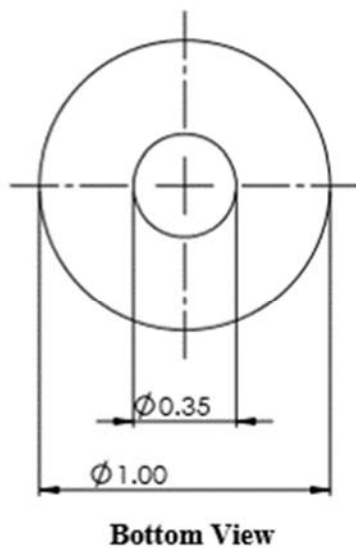
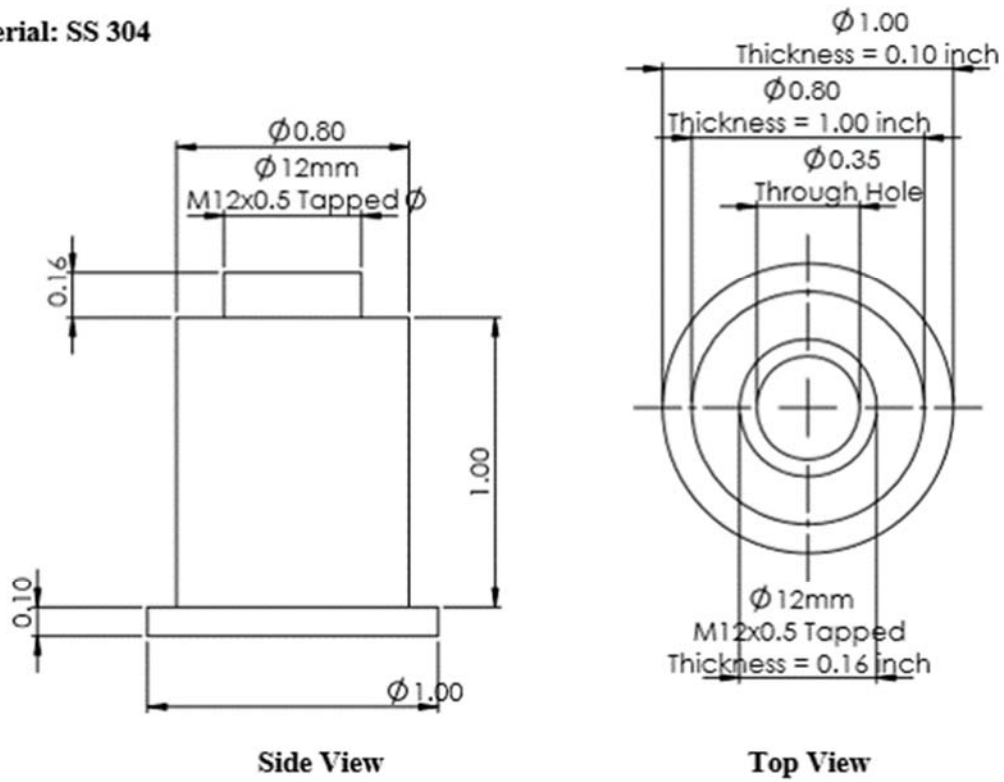
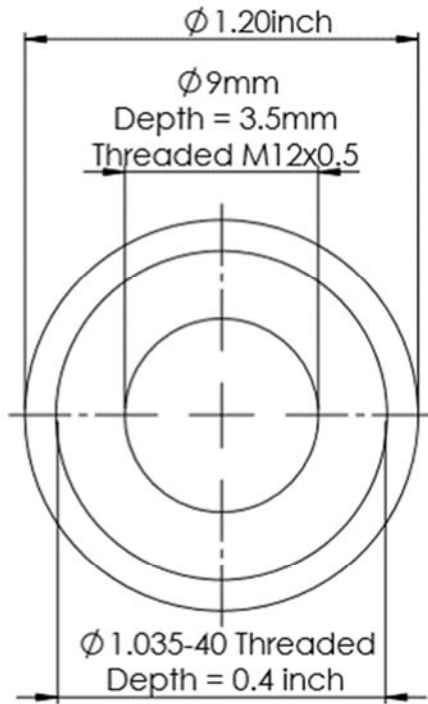
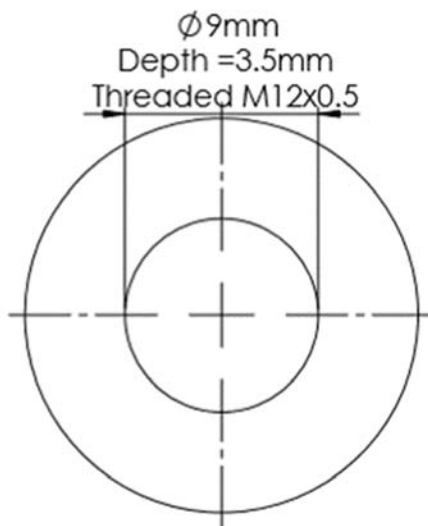
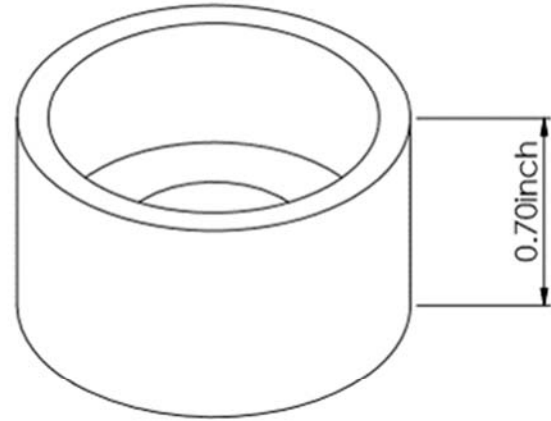


Figure S2.16. Flexure mount to mirror mount extension mount. This was designed to replace a Piezo which was originally used for an FS-CRDS design.



Top View



Bottom View

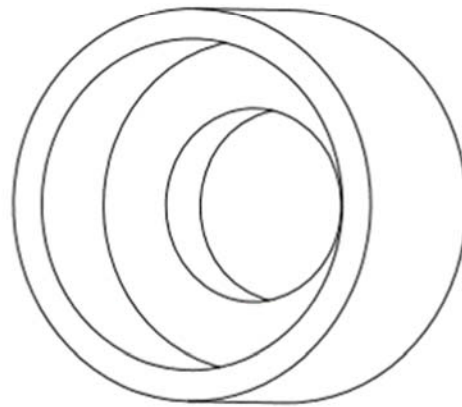
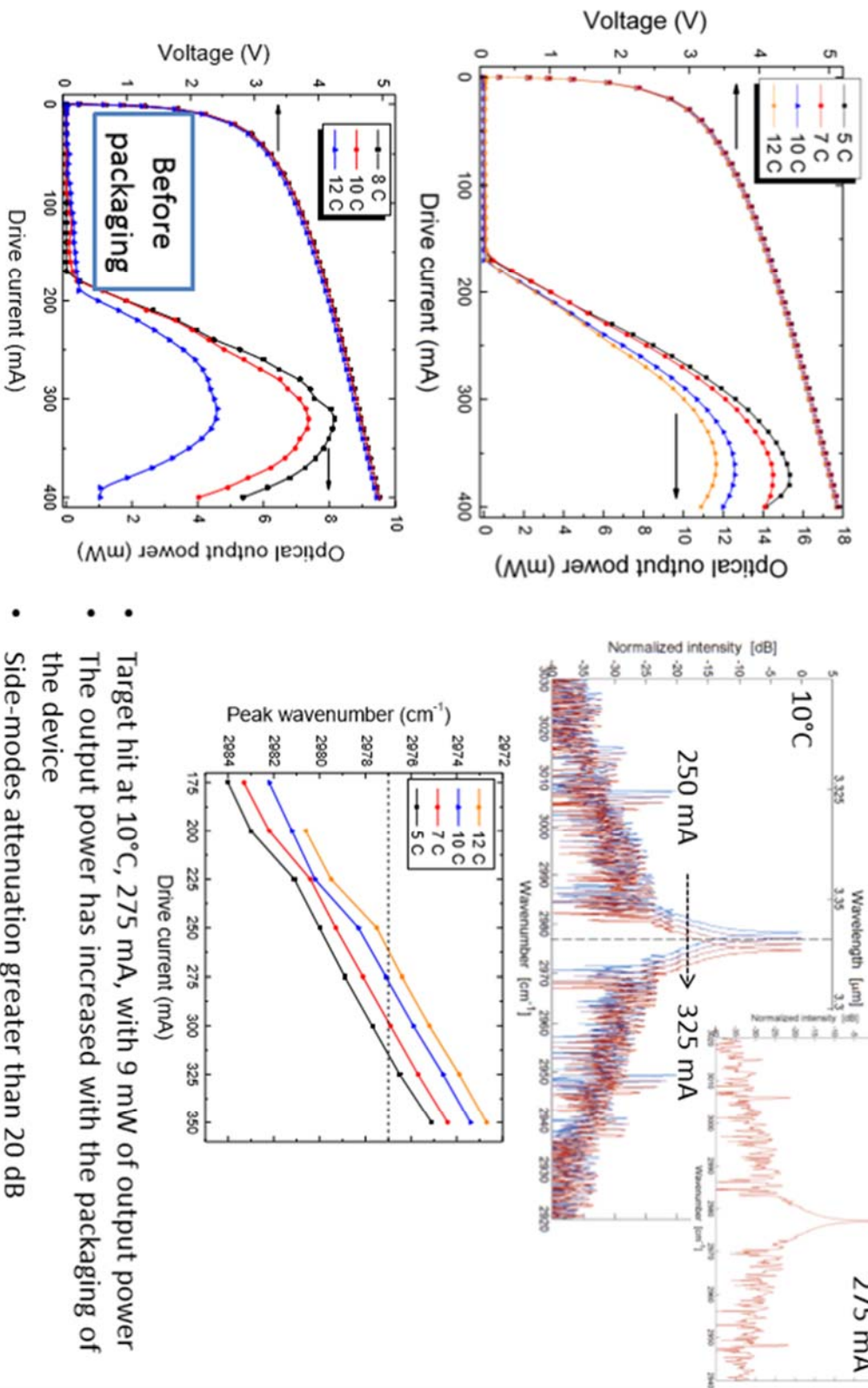


Figure S2.17. 1 inch mirror mount detail.

NRL30_4A_19-20_61, 2 mm, AR/Pass, 3.36 μm



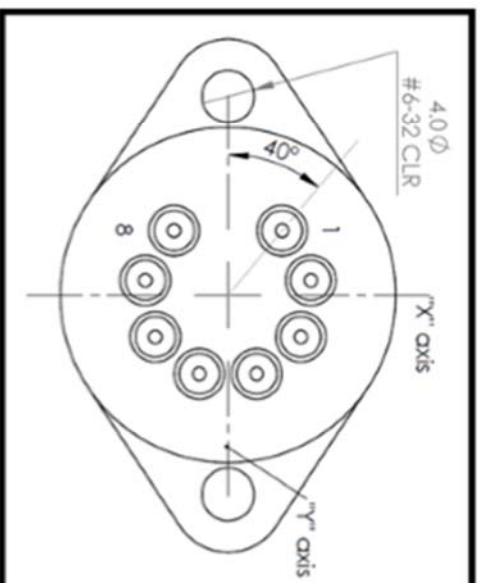
- Target hit at 10°C, 275 mA, with 9 mW of output power
- The output power has increased with the packaging of the device
- Side-modes attenuation greater than 20 dB

Figure S2.18. 3.36 μm IC laser detail.

Intense TO3 packages specifications

TEC	
DT _{max}	68 °C
U _{max}	3.78 V
I _{max}	1.75 A
Q _{cmax}	4.16 W
Thermomonic TEFC1-03120	

Thermistor	
R @ 25 °C	10 kΩ
C1	0.830 e-3
C2	2.651 e-4
C3	1.089 e-7
QTI QT0805Y-103	



Maximum allowed full divergence angle: 122°
 With 0.2 mm center tolerance: 116°

- Pin-out (as seen from the back):
- 1: TEC +
 - 2: Thermistor
 - 3: Thermistor
 - 4: LD +
 - 5: LD -
 - 6: Detector +
 - 7: Detector -
 - 8: TEC -

Figure S2.19. 3.36 μm IC laser intense TO3 package specifications.

Chapter 3: Soil Microbial Response to A Massive Natural Gas Leak: Case Study of the Porter Ranch Gas Leak

Patricia L. Tavormina¹, Sally Newman¹, Linhan Shen², Riley Duren³, Alexander Safian⁴, Allison Teunis⁴, Mitchio Okumura², Yuk L. Yung¹, and Victoria J. Orphan¹

1. Division of Geological and Planetary Sciences, California Institute of Technology, 1200 E. California Blvd, Pasadena, CA 91125, USA.
2. Division of Chemical Physics, California Institute of Technology, 1200 E. California Blvd, Pasadena, CA 91125, USA.
3. Jet Propulsion Laboratory, 4800 Oak Grove Dr, Pasadena, CA 91109, USA
4. Biology Department, California State University, Channel Islands, 1 University Dr., Camarillo CA, 93012, USA

ABSTRACT

The Porter Ranch gas leak released approximately 100,000 metric tons of natural gas directly into the atmosphere over 117 days between October 23rd, 2015, and February 17th, 2016. Additional natural gas was trapped in the soil around SS-25 after the leak was plugged, where the potential for biological mitigation exists. We investigated this possibility by tracking soil microbial populations and soil gas contents during and following the Porter Ranch gas leak. Our overarching goal was the identification natural mechanisms of alkane remediation during natural gas leaks. A secondary goal was to probe for similarities and differences in microbial dynamics during terrestrial and marine-based hydrocarbon emission events. Our results demonstrate that a member of *Spingobium* tracked closely with actively venting gas, accounting for as much as 20% of the microbial community. This lineage encodes genes for alkane oxidation, and consumes ethane in pure culture. A member of *Methylobacter* also enriched in numerous locations proximal to the leak, accounting for 5 – 12 % of the total microbial community. The enrichment of *Methlobacter* was only notable after SS-25 was repaired. Methane DNA stable isotope probing (DNA-SIP) of soils also identified *Methylobacter*, supporting an interpretation that this organism consumed methane in soils surrounding SS-25 following the gas leak. Additionally, cavity ring-down spectroscopic analysis of soil air measured elevated methane and carbon dioxide concentrations for at least 11 months following SS-25 well repair, suggesting that trapped or slowly outgassing methane may have been metabolized *in situ*. These data demonstrate that soils surrounding SS-25 provided a barrier for a portion of natural gas released during the Porter Ranch gas leak, and that a diverse assemblage of bacteria responded to this event for at least 11 months following repair. These results parallel microbial dynamics reported

at the Deepwater Horizon oil spill, and demonstrate that diverse microbial assemblages help to mitigate massive alkane emissions over time scales of months to years.

INTRODUCTION

The 2015 – 2016 Porter Ranch natural gas leak (“Aliso Canyon gas leak”) released approximately 100,000 metric tons of natural gas into the atmosphere from a 62-year-old well (Standard Sesnon 25, SS-25; operated by Southern California Gas, SoCal Gas) between October 23rd, 2015 and February 17th, 2016.(Conley et al., 2016; Safety, 2016) Additionally, approximately 4000 metric tons of ethane and less quantities of propane, tert-butyl mercaptan, tetrahydrothiophene, methyl mercaptan, and benzene were released. Gas initially escaped from a casing breach roughly 140 m underground and diffused through multiple routes to the soil surface. Ground level accumulation of methane and mercaptans was recorded by SoCal Gas on October 23rd, 2015. Eight “top kill” attempts between October and December damaged the shaft of SS-25, increasing the flow of gas directly to the atmosphere. Construction of a relief well began on December 4th to seal SS-25 at its base, “bottom kill”. SoCal Gas and California state officials declared the well successfully sealed on February 18th, 2016.

Natural gas (NG) is an attractive energy source because its combustion released fewer CO₂ equivalents to the atmosphere than oil. Additionally, newer extraction technologies including hydraulic fracturing make NG production economically competitive with oil. However, the NG industry, which includes functioning and abandoned wells, pipelines, and distribution points, experiences methane emission into the atmosphere throughout its delivery structure, fugitive emissions. These leaks offset the benefit of gas over oil.(Brandt et al., 2014) Estimates of the scale of NG leaks are highly variable. In the Uintah Valley, Utah, as much as

6.2 % – 11.7 % of extracted NG may be escaping from production lines.(Karion et al., 2013) Hydraulic fracturing of shale gas loses between 3.6 % and 7.9 % of methane over the lifetimes of wells.(Howarth et al., 2011) On the other hand, some estimates place leakage rates throughout the industry at 1.5 % of production.(Littlefield et al., 2017) Also, instrumentation based leak estimates differ from atmospheric estimates by at least an order of magnitude, and high and super emitters contribute disproportionately to atmospheric inventories.(Brandt et al., 2014; Kang et al., 2016) The Porter Ranch leak represents a NG super emitter event, and provides a unique opportunity to identify natural constraints on emission of NG to the atmosphere. Methane released during the leak permeated soil around SS-25, where the possibility for biological consumption exists. To our knowledge, biological remediation during super emitter events has not previously been reported, although methane oxidizing microorganisms associated with oil and gas infrastructure have been described.(Yang et al., 2016; Zhang et al., 2014) Identifying biological mechanisms of NG remediation during leaks may contribute to better modelling of instrumentation based estimations, particularly in situations where leaks permeate soils, and may also lead to novel mitigation strategies.

Methane is removed from the environment through photochemical and biological processes, and bacterial methane consumption contributes significantly to the sink strength of different soils.(Conrad, 2009; Le Mer and Roger, 2001) Methane oxidizing bacteria (MOB) represent the main biological sink for methane in aerobic soils. MOB oxidize methane using two distinct biochemical pathways. One pathway involves a cytoplasmic methane monooxygenase (soluble MMO; sMMO); the second involves a membrane bound methane monooxygenase (particulate MMO; pMMO).(Hanson and Hanson, 1996) The substrate ranges of sMMO and pMMO include not only methane but also hydrocarbons up to 8 carbons in length, and some

MMO enzyme variants prefer longer chains.(Sayavedra-Soto et al., 2011; Van Beilen and Funhoff, 2007) The ability to survive on methane as sole carbon and energy source (methanotrophy) is usually an obligate lifestyle, but some MOB are able to use methane facultatively.(Semrau et al., 2011) Different strategies via methane consumption directly pertain to microbial population dynamics, especially in environments where gas concentrations fluctuate.

Ecologically, Porter Ranch and Aliso Canyon are characterized by scrub and chaparral, with a Mediterranean climate and semi-arid soils. Literature describing MOB in semi-arid soils is limited, despite the documented role of semi-arid soils as methane sinks, and that 20 % of land mass is comprised of such soils.(Aronson et al., 2013) Moisture content, pH, and temperature drive biological methane oxidation in these soils, which host both cultivated and uncultivated MOB.(Angel and Conrad, 2009; Horz et al., 2005; Hou et al., 2012; Judd et al., 2016; Smith et al., 2000) The scale of the Porter Ranch natural gas leak and its localization to a chaparral biome provides a unique opportunity to study natural mechanisms of alkane cycling in semi-arid soils, and also to gain better understanding of methane consumption pathways during leaks. We tracked microbial populations and soil trace gas concentrations during and following the Porter Ranch leak towards this end. Our results add new perspective to the current understanding of nascent biological mechanisms that reduce natural gas loading in soils.

RESULTS AND DISCUSSION

We sampled soils at two depths (0 – 5 cm and 23 – 28 cm) throughout and surrounding the Aliso Canyon storage field between January 2016 and January 2017. In total, 71 soil cores were collected on 14 sampling trips spanning 13 months (Fig 3.1, Table S3.1) Cored soils were

binned into one of three groups: background soils surrounding the SoCal Gas property (Bkg_surr), background soils sampled on SoCal Gas property but over 150 m from SS-25 (Bkg_prop), and soils collected within a 150 m radius of SS-25 (SS-25_well).

Relationships between microbial communities and the impact of natural gas loading was assessed using four complementary approaches. First, iTag sequencing was applied to all samples to profile prokaryotic communities during the following the gas leak. Second, soils were probed directly for methane oxidizers with $^{13}\text{CH}_4$ DNA-SIP. Third, a lineage whose abundance spiked during the leak was isolated for pure culture analysis. Fourth, trace gas concentrations at ground level and in below-ground soil air were measured on a subset of cores.

iTag: General Microbial Community Comments

In samples throughout the dataset, *Archaea* accounted for 0.1 – 11.0 % of iTag reads. *Archaea* were more prevalent in the 23 – 28 cm horizon, and most sequences affiliated with soil *Crenarcheota* including the ammonia oxidizers *Candidatus Nitrosocosmicus oleophilus* MY3 (99 % identity, accession CP012850 and *Candidatus Nitrososphaera gargensis* Ga9.2 (96 % identity, accession CP002408). An *amo* sequence 78 % identical to the *amo* of *Ca. N. oleophilus* MY3 and 84 % identical to the *amo* of *Ca. N. gargensis* was also present in soils throughout the study area.

Within *Bacteria*, common taxa throughout the dataset typically affiliated with uncultured soil microorganisms within *Acidobacteria* (up to 30 % of reads in some samples), *Actinobacteria* (up to 58% of reads), *Nitrosomonadaceae* (up to 15 % of reads), and *Bacteroidetes* (up to 15 % of reads). In SS-25_well soils, a shift in the bacterial community towards *Gammaproteobacteria* (“gamma shift”) was detected. (Hamamura et al., 2006; Kabelitz et al., 2009; Margesin et al.,

2003; Militon et al., 2010; Popp et al., 2006) *Gammaproteobacteria* accounted for up to 12 % of iTag reads in these soils, roughly twice the value seen in background samples.

Environmental Enrichment of Canonical Soil Methane Oxidizers

In Bkg_surr cores, MOB (methane-oxidizing lineage affiliated with *Methyloxytaceae*, *Methylothermaceae*, and *Methylococcaceae*) were undetected in 41 % (9/22) of cores, and comprised less than 0.1 % of the microbial population in the remaining 59 % (13/22) of cores (Fig. 3.2a). In Bkg_prop cores, MOB were detected in 89 % of cores (16/18), but typically did not exceed 0.3 % of the microbial population. However, in one Bkg_prop core, MOB accounted for 3.4 % of the microbial population, and in a second core at the same location, they accounted for 2.4 % of the population (Fig. 3.2b). The two cores with elevated methanotroph abundance were collected in June and July 2016 near the southeast edge of the property, and were not associated with a well. MOB abundance estimated from background samples agree with past studies. (Kolb et al., 2005; Kou et al., 2017; Lau et al., 2015; Yang et al., 2012; Zhang et al., 2014)

In contrast, canonical MOB constituted up to 13.8 % of reads in SS-25_well cores. Enrichment was most evident after March 2016, when SS-25 had been repaired, and was primarily due to increase in *Methylobacter*. In 42 % (13/31) of SS-25_well cores, a member of *Methylobacter* (98 % identity, *M. luteus*, accession NR_041814) comprised between 1.6 % and 11.9 % of reads. In an additional 42 % (13/31) of cores, *Methylobacter* accounted for 0.1 % - 1.6 % of reads, and in 16 % (5/31) of cores, less than 0.1 % of reads (Fig. 3.2c). In other words, *Methylobacter* was invariably detected in cores taken within 150 m of SS-25 throughout the sampling series, typically at abundances far exceeding background soils. *Methylobacter* was generally localized to the 23 – 28 cm horizon and its enrichment was most evident following SS-

25 repair (Fig. 3.2c). In the 0 – 5 cm horizon, *Methylobacter* was detected in 74 % of cores and accounted for up to 2.2 % of the microbial population (Fig. 3.2c). Malghani et al. have reported previously that soil methanotroph abundance does not increase in response to methane loading over a 24-day laboratory incubation course, and that other environmental factors including nitrogen availability may drive methanotroph population size.(Malghani et al., 2016) Our results demonstrate that methanotroph abundance increases substantially over a time scale of months in soils associated with natural gas loading. The complexity of chemicals present in natural gas compared to pure methane, or the longer time frame of our study may resolve superficial differences in our respective results.

Sporadic enrichment of other MOB also occurred in SS-25_well soils. A member of *Methylocaldum* (99% identity to *Methylocaldum gracile*, accession NR_026063) accounted for 9 % of reads in a 23 -28 cm sample in July 2016, and 2.6 % of reads at the same location and depth in January 2017. A member of *Methylomicrobium* (98% identity to *Methylomicrobium agile*, accession EU144026) accounted for 8.9 % reads in a 0 – 5 cm sample in June 2016, and 1.2, 2.0 and 3.7 % of reads in three additional soil cores in July 2016. Members of the alphaproteobacterial family *Methylocystaceae*, including a sequence 94 % identical to *Methylosinus trichosporium* strain B3020 (accession LT220845) and a sequence 99 % identical to *Methylocystis hirsute* strain B3183 (accession LT220847) were slightly elevated relative to background, accounting for 0.1 % - 0.2 % of reads in four samples near SS-25 between June and October 2016. Also in October 2016, a single core was substantially enriched in a sequence 99 % identical to *M. trichosporium* strain B3020 (accession LT220845, 6.1 % of reads). This core was also enriched in a non-methanotrophic methylotrophic sequence affiliating with *Methlophilales*, accounting for an additional 6.5 % of reads.

Sequences related to facultative MOB in family *Beijenrickiaceae* (e.g. *Methlocapsa*, *Methylocella*, and the upland soil cluster, “USC”), were detected in very low abundance (< 0.1 % of reads) sporadically throughout the dataset.(Ricke et al., 2005) These sequences were present in 19 % of background cores (greatest abundance = 0.07 % of reads), and in 41 % of SS-25_well cores (greatest abundance = 0.09 % of reads). Facultative MOB are understood to consume atmospheric levels of methane, and have been shown to enrich in environments with elevated methane.(Ricke et al., 2005) Our results agree with current understanding that environmental *Methlocapsa*, *Methylocella*, and the USC are likely optimized to atmospheric levels of methane.

Excluding the sample in which *M. trichosporium* accounted for 6.1 % of reads, gammaproteobacterial methanotrophs greatly outnumbered alphaproteobacterial methanotrophs in SS-25_well soils. This result agrees with current models that gammaproteobacterial methanotrophs, as a group, have a lower affinity for methane than alphaproteobacterial methanotrophs, and are more likely to enrich following methane loading.(Duan et al., 2017; Knief and Dunfield, 2005; Knief et al., 2006) Recently, rice paddy soils exposed to a transient methane “pulse” have been shown to support metabolic activity of these low affinity gammaproteobacterial methanotrophs for several weeks, at atmospheric methane concentrations.(Cai et al., 2016) Gammaproteobacterial methanotrophs may therefore be capable of high affinity function following a methane pulse, an ability which may relate to the persistence of *Methylobacter* following SS-25 repair.

The diverse alpha- and gammaproteobacterial methanotrophs identified in this study demonstrate that a range of methanotrophic potential exists in the Aliso Canyon gas storage facility soils. Aliso Canyon is typified by chaparral, temperate grassland and shrub, with a Mediterranean climate. Rainfall average is 18 inches per year. During California’s 2011 – 2016

drought, rainfall decreased to 10 inches per year. Within this context, it is notable that all the obligate methanotrophs identified (expecting *Methylobacterium*) generate stable resting forms that enable survival during dehydration. (Bodrossy et al., 1997; Lindner et al., 2007; Titus et al., 1982; Whittenbury et al., 1970) *Methylobacter*, *Methylocaldum*, and *Methylocystis* form desiccation-resistant cysts, and *Methylosinus* forms desiccation-resistant exospores. This dehydration-resistant, methane-metabolizing seed population appears to play an active role in methane consumption following gas loading.

Identification of C1-Assimilating Lineages in DNA Stable Isotope Probing

We independently assessed biological methane-oxidizing potential in soils from Aliso Canyon in $^{13}\text{CH}_4$ DNA-SIP. Soil 270 meters southwest of SS-25 (Fig 1c) was collected on January 19th, 2016, and incubated with $^{13}\text{CH}_4$. This site was chosen for DNA-SIP because it was geologically similar and geographically close to SS-25, but impacted to a lesser degree by the leak and ongoing repair efforts. iTag data also indicated that the population structure in this core was similar to that at SS-25. Below-ground soil air samples gave no evidence of soil alkane enrichment, and outgassing was not observed at this site. Thus, of the cores collected, this site was deemed acceptably representative of naïve SS-25 soils. Three soil samples from this site were used in analysis. The first was initial soil representing a T_0 time point. The second and third were incubated with $^{12}\text{CH}_4$ and $^{13}\text{CH}_4$, for SIP analysis. (Neufeld et al., 2007) Three fractions (heavy, intermediate, and light) were collected from these three soil samples for iTag analysis (9 DNA samples total).

Light DNA from all three soil samples yielded a robust PCR product and over 21,000 iTAG reads each, as expected. However, there was insufficient intermediate and heavy DNA in the T_0 time point and in the $^{12}\text{CH}_4$ incubation to generate informative results. The PCR

amplification product from these four samples was not visible in gel electrophoresis, and the number of reads in iTAG was low, suggesting a “jackpot” PCR event. These results are also expected, as isotopically heavy DNA is not expected in these samples. The intermediate and heavy DNA from the 40-day $^{13}\text{CH}_4$ sample generated robust PCR products with over 30,000 quality iTag reads each.

Heavy DNA from the 40-day $^{13}\text{CH}_4$ sample was highly enriched in *Methylobacter* (34.6 % of reads at 40 day $^{13}\text{CH}_4$ incubation, Fig 3.3). *Methylobacter* accounted for only 0.6 % of reads in the light DNA from this soil sample, confirming that its growth derived from $^{13}\text{CH}_4$. Enrichment of *Methylobacter* in SIP analysis agrees well with environmental data, supporting our interpretation that *Methylobacter* consumed methane from the Porter Ranch leak. SIP analysis also identified *Methylomicrobium*, (approximately 0.2 % of reads in 40-day heavy DNA affiliated with this lineage, compared to 0.01 % of reads in light DNA). This slight effect is difficult to interpret but is also consistent with environmental data.

An additional 27.4 % of reads in 40-day heavy DNA were assigned to 5 genera (Fig 3.3). These genera included *Lysobacter* (12.9 % of reads in heavy DNA, 3.2 % in light DNA), *Luteimonas*, *Methylotenera*, and *Brevundimonas* (3.6 % of reads in heavy DNA, 0 % in light DNA each) and an uncultured member of *Nocardioidaceae* (3.7 % of reads in heavy DNA, 1.7 % in light DNA).

Lysobacter, a member of *Xanthomonadaceae*, consumes formate and is a micropredator.(Lueders et al., 2006; Nercessian et al., 2005) Thus, *Lysobacter* may have assimilated ^{13}C through cross-feeding on methane oxidation products including formate, or through predation of isotopically heavy bacteria, such as *Methylobacter* and *Methylomicrobium*. *Methylotenera* is a non-methanotrophic methylotroph capable of growth on methanol, and may

likewise have assimilated ^{13}C from cross-feeding.(Kalyuzhnaya et al., 2012) *Luteimonas* is an aerobic chemoorganotroph which has been associated previously with methane remediation in a coal-packed filtration system, although it is not considered a methane oxidizer.(Limbri et al., 2014) *Brevundimonas* is consortia with *Pseudomonas* has been shown to degrade dichloromethane, but a direct role in C1 metabolism has not been demonstrated.(Krausova et al., 2006) Finally, some members of *Nocardioideae* have been implicated in the degradation of butane although a role in C1 metabolism has not been established.(Hamamura and Arp, 2000) Overall, our DNA-SIP results supported environmental findings that members of *Methylobacter*, and possibly *Methylomicrobium*, are present in Porter Ranch soils and can respond to metabolize methane within weeks to months of exposure. Ecologically, our results identify potential microbial networks in chaparral soils through which methane loading can support both methanotrophic and non-methanotrophic microorganisms.

Additional Lineages That Enriched Near SS-25

In contrast to the prolonged enrichment of *Methylobacter* that occurred after SS-25 repair, a transient but substantial enrichment of *Sphingobium* was detected in 0 – 5 cm soils on February 6th, 2016. At a site of active outgassing adjacent to SS-25 (indicated by large arrowhead, Fig 1b), a member *Sphingomonadaceae* (97 % identity to *Sphingobium cloacae* accession AP017655) accounted for 19.5 % of total bacterial reads (Fig. 4). On March 24th, 2016, these lineages represented less than 2.4 % of total reads, and by June they represented less than 1.2 %. In the 23 – 28 cm depth horizon of these cores, *Sphingobium* modestly enriched, but never exceeded 0.5 % of reads. *Sphingobium* did not exceed 0.25 % of reads in any background sample, and was undetected in 45 % of background cores (Fig 4).

Genus *Sphingobium*, in *Alpharotobacteria*, is a strict aerobe known for its ability to bioremediate organic pollutants including hexachlorocyclohexane, phenoxybenzoate, toluene, and trichlorophenol.(Basta et al., 2005) *Sphingobium* typically encodes biodegradation genes on extra-chromosomal megaplasmids. Despite a recognized role in the biodegradation of xenobiotic compounds, *Sphingobium* has not previously been associated with remediation of short chain alkanes including methane or ethane. Given the substantial enrichment of this lineage at a site of active outgassing, we were interested in probing a possible role of *Sphingobium* in natural gas remediation at Porter Ranch. Thus, we isolated this organism in pure culture and probed its genomic content and alkane oxidizing capabilities.

Candidatus Sphingobium alkanivorans appeared as short, regular rods. It grew in 0.25 times strength LB broth or in nitrate mineral salts medium, provided media were amended with soil extract. The genome (4,513,283 nucleotides; 60.6% GC content) included a chromosome (4,276,307 nt) and a megaplasmid (236,976 nt). Like other *Sphingobium* spp, the megaplasmid encoded metabolic genes relevant to environmental pollution – in this case, alkane gases. Specifically, gene variants of particulate methane monooxygenase, soluble methane monooxygenase, and methanol dehydrogenase were all encoded extrachromosomally. Ca. *S. alkanivorans* was tested for its ability to consume methane and ethane, and was found able to draw down ethane, but not methane, over a three-week time course. This suggests that Ca. *S. alkanivorans* enriched at a site of outgassing because of its ability to consume ethane gas during the Porter Ranch gas leak.

Two additional non-methanotrophic taxa enriched in SS-25_well soils. A member of *Rhodospirillaceae*, accounting for up to 23 % of reads in some samples, enriched in the 23 – 28 cm horizon between March 2016 and January 2017. The enrichment pattern of

Rhodospirillaceae mirrored the pattern exhibited by *Methylobacter* (Fig 3.2). *Rhodospirillaceae* comprises phototrophic purple non-sulfur bacteria, and elevated CO₂ in soil air (Fig 3.5) may have contributed to its enrichment at Porter Ranch. *Rhodospirillaceae* also lives chemotrophically at reduced oxygen tensions, which may contribute to its residence in the 23 – 28 cm depth horizon.(Baldani et al., 2014) At least one member of *Rhodospirillaceae* encodes a methane monooxygenase homolog (*Skermanella aerolata*: NCBI accession AVFK01000000). The 16S sequence detected in the present dataset is 99 % identical to *Rhodospirillaceae* strain LP35, a bacterium isolated from ginger foundation soil (accession KC921152). This *Rhodospirillaceae* lineage was not enriched in background samples or in ¹³CH₄ DNA-SIP analysis.

Members of *Rhodococcus* (99 % identity to *Rhodococcus erythropolis*, accession KT 597555) were also slightly enriched in 0 – 5 cm SS-25_well soils following repair, and comprised up to 4.1 % of reads. *Rhodococcus* has previously been associated with propane oxidation.(Ashraf et al., 1994) *R. erythropolis* has been directly linked to the remediation of crude oil and encodes a formaldehyde dehydrogenase capable of oxidizing ethanol.(Eggeling and Sahm, 1985; Hamamura et al., 2006; Ohhata et al., 2007) The eight top-kill attempts of SS-25 caused forced ejection of kill fluids, including petroleum, from the well shaft.(Safety, 2016) The enrichment of relatives of *Rhodococcus erythropolis* in SS-25_well soils suggests that either short chain alkanes including ethane or propane, their metabolic byproducts, or petroleum products related to kill attempts, may have contributed to its enrichment at SS-25.

Trace Gas Elevation in SS-25 Soils

We used two methods to measure trace gas concentrations in soils. First, beginning in January 2016, triplicate soil samples were sealed in serum vials immediately upon sampling, for

headspace analysis (Table S3.1). Gas chromatography mass spectrometry (GC-MS) revealed a ~3 fold increase in methane values in SS-25_well soils compared to background samples, with wide variance between replicate vials. This elevation persisted throughout the duration of the study. Adsorption of hydrocarbon gases to soil particles may explain these results including variance between replicates.(Cheng and Huang, 2004; Jones and Drozd, 1983; Philp and Crisp, 1982)

A second approach to measure trace gases was implemented beginning in March 2016. In this approach, underground soil air was collected into evacuated flasks immediately upon removal of select cores. This approach estimates gas concentration in underground air, but not gas adsorbed to soil particles. Atmospheric samples, collected approximately 6 feet above ground were concurrently collected. Carbon dioxide, methane, and ethane concentrations in the collected air samples were measured using cavity ring-down spectroscopy (CRDS). In the case of CO₂, carbon isotope composition ($\delta^{13}\text{C}$) was simultaneously determined.

Ethane concentrations were less than 30 ppbv throughout the dataset (Table S3.1) and never comprised more than 1 % of methane concentrations. This suggests that ethane was remediated in soil, while methane values remained elevated. Multiple soil microorganisms including members of *Pseudomonas*, *Nocardia*, and *Mycobacterium* participate in the oxidation of higher order alkanes in soils.(Van Beilen and Funhoff, 2007) Our results suggest that *Ca. Sphingobium alkanivorans* may have played a direct role in remediating ethane during and after the leak event.

Methane and carbon dioxide were highly elevated in multiple SS-25_well soil air samples, but not in background samples or in atmospheric samples. The highest soil air methane value recorded was 7463 ppm in July 2016, although higher soil air values may have occurred at

sites of active outgassing during the leak (before CRDS analyses began). In general, cores with the high methane concentrations corresponded to sites that had previously exhibited active outgassing (arrows, Fig 3.1b). Eleven months following well repair, in January of 2017, methane concentrations were still significantly above background in one SS-25_well core soil air sample (106 ppm).

Aerated soils typically function as a methane sink, and it is not unusual for soil air methane concentrations to be below atmospheric values.(Dörr et al., 1993) In background cores, and in several cores near SS-25, methane concentrations in soil air ranged from 1.58 to 2.32 ppm, in support of a sink role of these soils. Overall, our data indicate the presence of underground pockets of natural gas, available to soil microbial communities, over a time scale of months to years. The enrichment of methane oxidizing bacteria including members of *Methylobacter* through this same time frame suggests metabolism of these methane pockets.

Carbon dioxide levels were also unusually high in multiple SS-25_well soil air samples. Over 20,000 ppm CO₂ was recorded in July 2016; two additional samples had CO₂ levels above 5,000 ppm (Fig 3.5). These were the same three samples that exhibited highly elevated methane concentrations, and both the methane and carbon dioxide values are among the highest reported in the literature.(Lovell et al., 1983; Pumpanen et al., 2003; Yonemura et al., 2013)

Additionally, the $\delta^{13}\text{C}$ values in these 3 samples were highly negative (-30.09 ‰, -31.62 ‰, and -32.18 ‰); overall, $\delta^{13}\text{C}$ (CO₂) became more negative as CH₄ and CO₂ concentrations increased in soil air. Natural gas has a substantially lighter carbon isotopic signature (thermogenic natural gas is usually greater than -50 ‰), whereas atmospheric CO₂ has $\delta^{13}\text{C}$ value of -9 ‰.(Golding et al., 2013) Soil carbon dioxide is often lighter than atmospheric carbon dioxide due to the respiration of C3 and C4 plants (isotopic signatures of -33 to -24 ‰, and -16 to -10 ‰

respectively. One SS-25_well soil air sample (collected July 2016) exhibited a $\delta^{13}\text{C}$ CO_2 value of -35.4 ‰, outside the normal range of plant respiration values. The $\delta^{13}\text{C}$ value of soil air carbon dioxide in background cores was between -18 and -10 ‰. Our data suggest that soil air carbon dioxide likely derives in part leaked natural gas, and it is respiration by soil bacteria. In total, the iTag and geochemical data provide strong evidence that pockets of natural gas persisted in soils for months following well repair, and that this gas was respired by soil microorganisms including methane oxidizing bacteria.

MATERIALS AND METHODS

Site Description and Sampling Locations

The Porter Ranch gas leak occurred due to breached casing at well SS-25, one of 115 storage injection wells operated by Southern California Gas company in Aliso Canyon. SS-25 (34°18'53.81"N 118°33'50.81"W) was originally an oil well and converted for gas injection/extraction in 1973. Sampling sites included “SS-25_well” samples, at a distance of 40 – 150m from SS-25; “Bkg_prop” samples, ~ 150 - 2000 m distance on SoCal Gas property, and “Bkg_surr” sites, from ~ 2000 - 3500 m distance, on public lands (Fig. 3.1). Sampling entailed visiting 2 - 4 sites per day, and collecting two to five cores per site.

At the time of the leak, gas stored at the Aliso Canyon facility was comprised of 94.8 % methane and 3.53 % ethane (mole %, SoCal Gas, pers. comm.). These numbers agree well with emission estimates reported in which placed methane at 25 times the abundance of ethane in the plume above SS-25. (Conley et al., 2016)

Soil Collection

PVC soil corers (24 inches long, 2 inches diameter) were sliced lengthwise to aid disassembly. Corers were assembled with duct tape prior to field sampling. Assembled corers were pounded into the ground with a heavy mallet to a depth of 50 cm. The corer was rotated every 5th strike to maintain mobility of the corer. Soil cores were pulled from the ground, and the PVC tubing sliced through one lengthwise duct tape seam to open the corers. Typical soil cores were ~ 30 cm due to compaction. Sampled depths refer to compacted soil.

Working quickly, soil was partitioned at 0 – 5 cm and 23 – 28 cm. Approximately 15 g of soil from each depth was transferred into 15 ml conical polypropylene tubes (Falcon, Fisher catalog 14-959-53A). These samples provided source material for DNA extractions. In triplicate, additional 1g soil samples were transferred into 8 ml Restek crimp seal vials containing 3 ml 5 M NaOH and sealed. These samples provided source material for estimation of methane adsorbed to soil particles. Soil from 5 – 23 cm deep was sampled into 50 ml conical polypropylene tubes (Falcon brand, Fisher catalog 14-959-49A) to estimate approximate moisture content in different sampling areas over the study period. These samples were weighed at the laboratory, placed at 80 °C, and weighed again at one week. Any remaining soil from cores was bagged and stored at -20 °C to provide material for soil extract. Samples were transported to the laboratory within four hours of collection. Soil for DNA analysis was stored at -80 °C until processing.

DNA Stable Isotope Probing

Soil (23 – 28 cm horizon) from 270 m southwest of SS-25 was gently homogenized for 5 minutes using a spatula. A 10 g portion was immediately stored at -80 °C (= T₀). Two additional 10 g samples were placed into 80 ml serum bottles and crimp sealed. To these samples, with 3 ml of either ¹²CH₄ or ¹³CH₄ was added, and the bottles were rocked on a tilt platform at 22 °C.

Headspace in the bottles was refreshed on days 3, 9, and 20, and soil was stored at -80 °C on day 40. DNA was extracted from 0.25 aliquots of these 3 stored soil samples (T₀, 40 day ¹²CH₄ and 40d ¹³CH₄), as described below. From each DNA extract, ¹³C-labelled DNA (“heavy DNA”) was separated from ¹²C-labelled DNA (“light DNA”) via CsCl gradient centrifugation following (Neufeld et al., 2007). In addition to light and heavy DNA, the intermediate fraction, theoretically containing DNA with both ¹²C and ¹³C isotopes of carbon, was also collected (“intermediate DNA”).

DNA Extraction and Amplification

DNA was isolated from 0.25 g soil samples using the MoBio Power Soil beadbeating DNA isolation kit (catalog #12888, www.mobio.com) following manufacturer’s instructions in a final volume of 75 microliters (μl). Final DNA concentrations ranged from 2 – 40 ng/l and were stored at -80 °C as master stocks. Aliquots of each sample, diluted to 1 ng/l in Tris-EDTA pH 8.0, were stored at -20 °C as working stocks. DNA extracted from 0 – 5 cm depth routinely yielded between 0.75 and 4 g of nucleic acid (~ 3 – 12 g of DNA per gram soil). DNA extracted from 23 – 28 cm depth yielded between 0.15 and 0.75 g (~ 0.6 – 3 g DNA per gram soil).

To determine the microbial makeup in each DNA extract, a 2-step iTag amplification method was used (Kozich et al., 2013). The first amplification step targets a ~ 400 bp region of the prokaryotic 16S gene encompassing the 4th and 5th variable regions of the 16S gene (V45, positions 515 – 926). Primers used for the first amplification (16S_515F-ym:

TCGTCGGCAGCGTCAGATGTGTATAAGAGACAGGTGYCAGCMGCCGCGGTAA;

16S_926R-ymr_2step:

GTCTCGTGGGCTCGGAGATGTGTATAAGAGACAGCCGYCAATTYMTTTRAGTTT)

include a 21 – 22 nucleotide Illumina adapter sequence, a 10 nucleotide pad sequence, a 2

nucleotide linker that is non-complementary to the 16S gene, and the gene specific primer. Duplicate PCR reactions were performed per sample, each containing 1 ng DNA as template. Reagents and cycling conditions are as described by (Kozich et al., 2013). A robust PCR product was attainable after 25 cycles using this approach. PCR product strength was assessed via 1 % agarose gel electrophoresis. “No template controls” “mock extracts” and some samples (in particular, intermediate and heavy DNA fractions from T₀ and ¹²CH₄ incubations in SIP) showed no amplification in this visual assessment. Duplicate reactions from all samples including negative controls were pooled and 5 µl of pooled product served as template in the second (barcoding) amplification step.

The second amplification step added a unique 8-nt index (“tag” “barcode”) to each end of the amplicon. Reagents, cycling conditions, and unique index sequences were used as described in (Kozich et al., 2013). Final DNA yield was quantified from each sample, and equimolar quantities were pooled to create a single bulk amplicon. This bulk amplicon was cleaned with the Qiagen PCR purification kit (catalog 28105; Qiagen, Culver City CA) following manufacturer’s guidelines, and eluted in elution buffer. Approximately 1 µg of purified pooled amplicon was sequenced commercially on the MiSeq platform (Laragen, Culver City, CA.). Resulting reads were paired, trimmed and screened for contamination and chimeras. On average, each environmental sample generated 21484 ± 4470 quality reads. Mock extract and no template samples generated 117 ± 30 reads per sample. Quality reads were aligned to the Silva 115 database and level 1 – 6 taxonomic assignments were generated. BIOM-formatted abundance tables were generated from this information, and singletons were removed. The data was downloaded to an Excel-readable file for additional analysis.

Media for cultivation of *Sphingobium spp*

Nitrate mineral salts medium (NMS) was prepared according to standard recipes (ATCC #1306). Soil extract was prepared by adding distilled water to soil at a 1:1 v/v ratio and autoclaving this slurry twice for 30 minutes at 121 °C and 15 psi. Upon cooling, the liquid from this treatment was filtered through a 0.4-micron filter into a sterile bottle, and stored at 4 °C. A 1/20 volume of soil extract was added to NMS to make liquid soil extract-NMS media (SE-NMS). For solid media, agar (BD Bacto, Fisher catalog # DF0140-15-4) was added to 1.5% wt, autoclaved as above, and poured into sterile petri dishes. To reduce contamination by molds, cycloheximide was added to media intended for use with live soil at a final concentration of 50 g/ml.

Isolation of *Candidatus Sphingobium alkanivorans*

A 0.1 g soil sample from soil core #13 (0 – 5 cm), which was collected at a site of active outgassing on February 6th, 2016 and which exhibited *Sphingobium* species at roughly 20 % of the total microbial community, was transferred from -80 °C storage into 200 µl of 1x NMS media. This mixture was vortexed moderately for 20 seconds, and allowed to stand for 5 minutes. The supernatant was diluted 10-fold and 100-fold into sterile liquid NMS media. Samples from each dilution were plated on duplicate soil extract-NMS plates containing cycloheximide, and incubated at 23 °C. After 1-week, 60 colonies were patched to new soil extract-NMS plates. These passaged plates were incubated for 5 days, whereupon patched colonies were probed in qPCR to identify patches containing members of *Sphingobium*. 3 patches were identified via qPCR, and cells from each of these patches were transferred to liquid SE-NMS media and diluted to extinction via 10-fold serial dilution. These tubes were incubated at 23 °C with gentle rotation. After 1-week growth, 1 ml from each tube was pelleted, resuspended in 50 µl Tris-EDTA (TE, pH 8.0), and probed in qPCR. The most diluted sample

that gave a positive qPCR result was diluted to extinction a second time. Purity of the final culture was assessed by amplifying the full length 16S gene with the Bac8F and Uni1492R primers (Lane, 1991) and sequencing the amplicon (Laragen, Culver City CA). The 16S sequence was compared against iTag data to ensure that the isolate represented the same taxon identified in TAG. Using this approach, a pure culture of *Sphingobium* was obtained.

Genomic Sequencing and Analysis

Ca. Sphingobium alkanivorans was inoculated into 2L of soil extract-NMS liquid media and grown to saturation (OD600 ~ 0.8). Cells were pelleted in a Beckman Coulter Allegra X-15R tabletop centrifuge at 4000 RPM for 20 minutes. The supernatant was discarded and the pellets stored at -20 °C until processing. DNA was extracted from pellets with a standard protease K-lysozyme-phenol extraction treatment (Wilson, 2001). Approximately 15 µg of DNA were cleaned using the PowerClean DNA clean-up kit (MoBio; www.mobio.com) and sent to Pacific Biosciences genomic services at the University of Washington for single-molecule real-time (SMRT) sequencing. The genomic data was annotated in NMPDR RAST.

Trace Gas Analysis

Soil gas samples were collected in 2-liter glass flasks. These flasks were evacuated and closed off prior to sample collection. During sample collections, air was let into the flask by slowly opening the Teflon valve enclosing it to reach ambient pressure. A coarse particle filter was placed at the end of the gas introduction tube to capture large dust particles. It was then allowed a 3 minutes wait time after the valve was fully opened to ensure full equilibrium. Contents of these glass flasks were then analyzed in lab. Air samples were first analyzed using a commercially available Picarro gas analyzer to measure concentrations of CH₄ and CO₂, and

$\delta^{13}\text{C}$ of CO_2 . After the initial analysis, $\sim 80\%$ of the air remains in the flask. A mid-IR cavity ring-down spectrometer (CRDS) was then used to measure the C_2H_6 concentration. Samples with CH_4 or CO_2 concentrations much higher than the dynamic range of the Picarro analyzer were diluted after initial analysis. The dilution was done by pumping part of the gas sample out and filled with zero air to 760 Torr. The diluted samples then went through the same analysis process to measure CH_4 and CO_2 concentrations and C_2H_6 concentration.

The mid-IR cavity ring-down spectrometer was constructed and tested in the Okumura group and discussed in the previous chapter. This CRDS spectrometer uses a continuous-wave (cw) interband cascade laser (ICL) centered at $3.36\ \mu\text{m}$ to measure ethane concentrations, which takes advantage of the large absorption cross section in the mid-IR region and the long light and molecule interaction pathlength ($\sim 4.5\ \text{km}$). Ethane concentration was measured by expanding the full content of the 2 L flask after Picarro analyzer measurement into the CRDS analysis cell. Two ethane absorption bands centered at $2976.788\ \text{cm}^{-1}$ and $2983.383\ \text{cm}^{-1}$ were measured for each air sample (sample spectra shown in Fig S3.3). Ethane abundance was reported as an average of the concentration retrieved from both absorption bands. This spectrometer can measure ethane abundance as low as 200 pptv at standard temperature and pressure. Careful characterization of the spectrometer has shown that for a typical 10 ppbv C_2H_6 air sample, the precision of the measurements is $< 0.3\ \%$. Absolute ethane concentration measurement of the spectrometer was calibrated by measuring the ethane abundance in a diluted 1:200 ethane to methane in air, whose methane abundance was further calibrated by the Picarro instrument used for CH_4 , CO_2 , and $\delta^{13}\text{C}$ (CO_2) measurement.

CONCLUSIONS AND BROADER CONTEXT

The energy sector increasingly relies on natural gas, particularly as extraction and production becomes economically competitive with oil. Because of the aging infrastructure associated with gas extraction and storage facilities, high and super emitting gas leaks are ongoing issues within the industry. In this study, we investigated the response of soil microorganisms during the following the 2015 – 2016 Porter Ranch super emitting gas leak. Environmental samples were collected and processed using a suite of complementary methods. This work provides three novel and notable findings, regarding the remediative capacity of natural microbiomes to hydrocarbon loading events.

First, during the leak, a member *Sphingobium* accounted for 19.5 % of the total microbial community in an area of active outgassing. As a genus, *Sphingobium* remediates a range of xenobiotic compounds including aromatic hydrocarbons, but has not previously been associated with short chain alkanes. In pure culture, *Ca. Sphingobium alkanivorans* did not consume methane, but did effectively remediate ethane, which comprised between 3.5 and 4 % of the venting gas. Following well repair, *Sphingobium* declined in abundance, and methane oxidizing bacteria including *Methylobacter* enriched. 20th century studies on cultured methanotrophic bacteria documented the inhibitory effect of ethane on their ability to metabolize methane, and results here are consistent with the idea that ethane may suppress methanotrophs within strictly environmental context.(Dworkin and Foster, 1958; Leadbetter and Foster, 1958) Thus, remediation of ethane may be a prerequisite for effective drawdown of environmental methane via MOB, and mitigation of ethane during leak events may promote natural methane remediation in soils.

Second, the bloom patterns exhibited by *Sphingobium* and MOB including *Methylobacter* during the Porter Ranch gas leak share similarity with the microbial response to the Deepwater

Horizon (DWH) oil spill.(Hazen et al., 2010; Redmond and Valentine, 2012) Specifically, a robust bloom of non-methanotrophic lineages encoding sequence – divergent MMOs was followed by a smaller but sustained bloom of MOB. These similar patterns, from two distinct hydrocarbon spill types, suggest conservation of microbial community functioning following massive hydrocarbon events. *Sphingobium*, isolated from Porter Ranch soils, represents a new resource to explore the role of sequence divergent monooxygenases that bloom in the wake of massive emission events. Additionally, the MOB identified in this study affiliate with genera capable of forming desiccation resistant resting stages, an ideal adaptation to chaparral ecosystems.

Third, our results identify likely natural routes of carbon flow from methane into the broader soil community. Trace gas and isotopic analysis of soil air suggests that natural gas is metabolized *in situ*. By-products including methanol or formate may serve as substrates to non-methanotrophic bacteria, such as recovery of *Lysobacter* and *Methylothera* in SIP analysis; additionally, *Lysobacter* may access methane derived carbon through micropredation of MOB. The enrichment of *Rhodospirillaceae* in SS-25_well soils suggest that photoautotrophs may benefit from CO₂ elevation in soils, in this study the CO₂ appears derived from natural gas metabolism. We believe that these collective findings improve and broaden our understanding of soil microbial networks, and contribute new considerations for the development of working strategies to reduce methane emissions associated with the natural gas industry.

REFERENCE

- Angel, R. and Conrad, R. (2009) In situ measurement of methane fluxes and analysis of transcribed particulate methane monooxygenase in desert soils. *Environmental microbiology* 11, 2598-2610.
- Aronson, E.L., Allison, S.D. and Helliker, B.R. (2013) Environmental impacts on the diversity of methane-cycling microbes and their resultant function.
- Ashraf, W., Mihdhir, A. and Murrell, J.C. (1994) Bacterial oxidation of propane. *FEMS microbiology letters* 122, 1-6.
- Baldani, J.I., Videira, S.S., dos Santos Teixeira, K.R., Reis, V.M., de Oliveira, A.L.M., Schwab, S., de Souza, E.M., Pedraza, R.O., Baldani, V.L.D. and Hartmann, A. (2014) The family rhodospirillaceae, *The Prokaryotes*. Springer, pp. 533-618.
- Basta, T., Buerger, S. and Stolz, A. (2005) Structural and replicative diversity of large plasmids from sphingomonads that degrade polycyclic aromatic compounds and xenobiotics. *Microbiology* 151, 2025-2037.
- Bodrossy, L., Holmes, E.M., Holmes, A.J., Kovács, K.L. and Murrell, J.C. (1997) Analysis of 16S rRNA and methane monooxygenase gene sequences reveals a novel group of thermotolerant and thermophilic methanotrophs, *Methylocaldum* gen. nov. *Archives of Microbiology* 168, 493-503.
- Brandt, A.R., Heath, G.A., Kort, E.A., O'Sullivan, F., Petron, G., Jordaan, S.M., Tans, P., Wilcox, J., Gopstein, A.M., Arent, D., Wofsy, S., Brown, N.J., Bradley, R., Stucky, G.D., Eardley, D. and Harriss, R. (2014) Energy and environment. Methane leaks from North American natural gas systems. *Science* 343, 733-735.

- Cai, Y., Zheng, Y., Bodelier, P.L., Conrad, R. and Jia, Z. (2016) Conventional methanotrophs are responsible for atmospheric methane oxidation in paddy soils. *Nature communications* 7.
- Cheng, A.-L. and Huang, W.-L. (2004) Selective adsorption of hydrocarbon gases on clays and organic matter. *Organic geochemistry* 35, 413-423.
- Conley, S., Franco, G., Faloon, I., Blake, D.R., Peischl, J. and Ryerson, T.B. (2016) Methane emissions from the 2015 Aliso Canyon blowout in Los Angeles, CA. *Science* 351, 1317-1320.
- Conrad, R. (2009) The global methane cycle: recent advances in understanding the microbial processes involved. *Environmental Microbiology Reports* 1, 285-292.
- Dörr, H., Katruff, L. and Levin, I. (1993) Soil texture parameterization of the methane uptake in aerated soils. *Chemosphere* 26, 697-713.
- Duan, Y.-F., Reinsch, S., Ambus, P., Elsgaard, L. and Petersen, S.O. (2017) Activity of Type I Methanotrophs Dominates under High Methane Concentration: Methanotrophic Activity in Slurry Surface Crusts as Influenced by Methane, Oxygen, and Inorganic Nitrogen. *Journal of Environmental Quality*.
- Dworkin, M. and Foster, J.W. (1958) Experiments with some microorganisms which utilize ethane and hydrogen. *J Bacteriol* 75, 592-603.
- Eggeling, L. and Sahm, H. (1985) The formaldehyde dehydrogenase of *Rhodococcus erythropolis*, a trimeric enzyme requiring a cofactor and active with alcohols. *Eur J Biochem* 150, 129-134.
- Golding, S.D., Boreham, C.J. and Esterle, J.S. (2013) Stable isotope geochemistry of coal bed and shale gas and related production waters: a review. *International Journal of Coal Geology* 120, 24-40.

- Hamamura, N. and Arp, D.J. (2000) Isolation and characterization of alkane-utilizing *Nocardioides* sp. strain CF8. *FEMS microbiology letters* 186, 21-26.
- Hamamura, N., Olson, S.H., Ward, D.M. and Inskeep, W.P. (2006) Microbial population dynamics associated with crude-oil biodegradation in diverse soils. *Appl. Environ. Microbiol.* 72, 6316-6324.
- Hanson, R.S. and Hanson, T.E. (1996) Methanotrophic bacteria. *Microbiol Rev* 60, 439-471.
- Hazen, T.C., Dubinsky, E.A., DeSantis, T.Z., Andersen, G.L., Piceno, Y.M., Singh, N., Jansson, J.K., Probst, A., Borglin, S.E. and Fortney, J.L. (2010) Deep-sea oil plume enriches indigenous oil-degrading bacteria. *Science* 330, 204-208.
- Horz, H.-P., Rich, V., Avrahami, S. and Bohannan, B.J. (2005) Methane-oxidizing bacteria in a California upland grassland soil: diversity and response to simulated global change. *Appl. Environ. Microbiol.* 71, 2642-2652.
- Hou, L.-Y., Wang, Z.-P., Wang, J.-M., Wang, B., Zhou, S.-B. and Li, L.-H. (2012) Growing season in situ uptake of atmospheric methane by desert soils in a semiarid region of northern China. *Geoderma* 189, 415-422.
- Howarth, R.W., Santoro, R. and Ingraffea, A. (2011) Methane and the greenhouse-gas footprint of natural gas from shale formations. *Climatic Change* 106, 679.
- Jones, V. and Drozd, R. (1983) Predictions of oil or gas potential by near-surface geochemistry. *AAPG Bulletin* 67, 932-952.
- Judd, C.R., Koyama, A., Simmons, M.P., Brewer, P. and von Fischer, J.C. (2016) Co-variation in methanotroph community composition and activity in three temperate grassland soils. *Soil Biology and Biochemistry* 95, 78-86.

Kabelitz, N., Machackova, J., Imfeld, G., Brennerova, M., Pieper, D.H., Heipieper, H.J. and Junca, H. (2009) Enhancement of the microbial community biomass and diversity during air sparging bioremediation of a soil highly contaminated with kerosene and BTEX. *Applied microbiology and biotechnology* 82, 565-577.

Kalyuzhnaya, M.G., Beck, D.A., Vorobev, A., Smalley, N., Kunkel, D.D., Lidstrom, M.E. and Chistoserdova, L. (2012) Novel methylotrophic isolates from lake sediment, description of *Methylotenera versatilis* sp. nov. and emended description of the genus *Methylotenera*. *International journal of systematic and evolutionary microbiology* 62, 106-111.

Kang, M., Christian, S., Celia, M.A., Mauzerall, D.L., Bill, M., Miller, A.R., Chen, Y., Conrad, M.E., Darrah, T.H. and Jackson, R.B. (2016) Identification and characterization of high methane-emitting abandoned oil and gas wells. *Proceedings of the National Academy of Sciences* 113, 13636-13641.

Karion, A., Sweeney, C., Pétron, G., Frost, G., Michael Hardesty, R., Kofler, J., Miller, B.R., Newberger, T., Wolter, S. and Banta, R. (2013) Methane emissions estimate from airborne measurements over a western United States natural gas field. *Geophysical Research Letters* 40, 4393-4397.

Knief, C. and Dunfield, P.F. (2005) Response and adaptation of different methanotrophic bacteria to low methane mixing ratios. *Environmental microbiology* 7, 1307-1317.

Knief, C., Kolb, S., Bodelier, P.L., Lipski, A. and Dunfield, P.F. (2006) The active methanotrophic community in hydromorphic soils changes in response to changing methane concentration. *Environmental Microbiology* 8, 321-333.

- Kolb, S., Knief, C., Dunfield, P.F. and Conrad, R. (2005) Abundance and activity of uncultured methanotrophic bacteria involved in the consumption of atmospheric methane in two forest soils. *Environmental Microbiology* 7, 1150-1161.
- Kou, Y., Li, J., Wang, Y., Li, C., Tu, B., Yao, M. and Li, X. (2017) Scale-dependent key drivers controlling methane oxidation potential in Chinese grassland soils. *Soil Biology and Biochemistry* 111, 104-114.
- Kozich, J.J., Westcott, S.L., Baxter, N.T., Highlander, S.K. and Schloss, P.D. (2013) Development of a dual-index sequencing strategy and curation pipeline for analyzing amplicon sequence data on the MiSeq Illumina sequencing platform. *Appl. Environ. Microbiol.* 79, 5112-5120.
- Krausova, V.I., Robb, F.T. and González, J.M. (2006) Biodegradation of dichloromethane in an estuarine environment. *Hydrobiologia* 559, 77-83.
- Lane, D. (1991) 16S/23S rRNA sequencing, in: Stackenbrandt, E., Goodfellow, M. (Eds.), *Nucleic acid techniques in bacterial systematics*. John Wiley and sons, New York, NY, pp. 115-175.
- Lau, E., Dillard, Z.W., Dague, R.D., Semple, A.L. and Wentzell, W.L. (2015) High Throughput Sequencing to Detect Differences in Methanotrophic Methylococcaceae and Methylocystaceae in Surface Peat, Forest Soil, and Sphagnum Moss in Cranesville Swamp Preserve, West Virginia, USA. *Microorganisms* 3, 113-136.
- Le Mer, J. and Roger, P. (2001) Production, oxidation, emission and consumption of methane by soils: a review. *European Journal of Soil Biology* 37, 25-50.
- Leadbetter, E.R. and Foster, J.W. (1958) Studies on some methane-utilizing bacteria. *Arch Mikrobiol* 30, 91-118.

Limbri, H., Gunawan, C., Thomas, T., Smith, A., Scott, J. and Rosche, B. (2014) Coal-packed methane biofilter for mitigation of green house gas emissions from coal mine ventilation air. *PloS one* 9, e94641.

Lindner, A.S., Pacheco, A., Aldrich, H.C., Staniec, A.C., Uz, I. and Hodson, D.J. (2007) *Methylocystis hirsuta* sp. nov., a novel methanotroph isolated from a groundwater aquifer. *International journal of systematic and evolutionary microbiology* 57, 1891-1900.

Littlefield, J.A., Marriott, J., Schivley, G.A. and Skone, T.J. (2017) Synthesis of recent ground-level methane emission measurements from the US natural gas supply chain. *Journal of Cleaner Production* 148, 118-126.

Lovell, J., Hale, M. and Webb, J. (1983) Soil air carbon dioxide and oxygen measurements as a guide to concealed mineralization in semi-arid and arid regions. *Journal of Geochemical Exploration* 19, 305-317.

Lueders, T., Kindler, R., Miltner, A., Friedrich, M.W. and Kaestner, M. (2006) Identification of bacterial micropredators distinctively active in a soil microbial food web. *Appl. Environ. Microbiol.* 72, 5342-5348.

Malghani, S., Reim, A., von Fischer, J., Conrad, R., Kuebler, K. and Trumbore, S.E. (2016) Soil methanotroph abundance and community composition are not influenced by substrate availability in laboratory incubations. *Soil Biology and Biochemistry* 101, 184-194.

Margesin, R., Labbe, D., Schinner, F., Greer, C. and Whyte, L. (2003) Characterization of hydrocarbon-degrading microbial populations in contaminated and pristine alpine soils. *Appl. Environ. Microbiol.* 69, 3085-3092.

Militon, C., Boucher, D., Vachelard, C., Perchet, G., Barra, V., Troquet, J., Peyretailade, E. and Peyret, P. (2010) Bacterial community changes during bioremediation of aliphatic hydrocarbon-contaminated soil. *FEMS Microbiology Ecology* 74, 669-681.

Nercessian, O., Noyes, E., Kalyuzhnaya, M.G., Lidstrom, M.E. and Chistoserdova, L. (2005) Bacterial populations active in metabolism of C1 compounds in the sediment of Lake Washington, a freshwater lake. *Appl. Environ. Microbiol.* 71, 6885-6899.

Neufeld, J.D., Vohra, J., Dumont, M.G., Lueders, T., Manefield, M., Friedrich, M.W. and Murrell, J.C. (2007) DNA stable-isotope probing. *Nature protocols* 2, 860-866.

Ohhata, N., Yoshida, N., Egami, H., Katsuragi, T., Tani, Y. and Takagi, H. (2007) An extremely oligotrophic bacterium, *Rhodococcus erythropolis* N9T-4, isolated from crude oil. *Journal of bacteriology* 189, 6824-6831.

Philp, R. and Crisp, P. (1982) Surface geochemical methods used for oil and gas prospecting—a review. *Journal of Geochemical Exploration* 17, 1-34.

Popp, N., Schlömann, M. and Mau, M. (2006) Bacterial diversity in the active stage of a bioremediation system for mineral oil hydrocarbon-contaminated soils. *Microbiology* 152, 3291-3304.

Pumpanen, J., Ilvesniemi, H., PERÄMÄKi, M. and Hari, P. (2003) Seasonal patterns of soil CO₂ efflux and soil air CO₂ concentration in a Scots pine forest: comparison of two chamber techniques. *Global Change Biology* 9, 371-382.

Redmond, M.C. and Valentine, D.L. (2012) Natural gas and temperature structured a microbial community response to the Deepwater Horizon oil spill. *Proc Natl Acad Sci U S A* 109, 20292-20297.

Ricke, P., Kube, M., Nakagawa, S., Erkel, C., Reinhardt, R. and Liesack, W. (2005) First genome data from uncultured upland soil cluster alpha methanotrophs provide further evidence for a close phylogenetic relationship to *Methylocapsa acidiphila* B2 and for high-affinity methanotrophy involving particulate methane monooxygenase. *Appl. Environ. Microbiol.* 71, 7472-7482.

Safety, I.T.F.o.N.G.S. (2016) Ensuring Safe and Reliable Underground Natural Gas Storage.

Sayavedra-Soto, L.A., Hamamura, N., Liu, C.W., Kimbrel, J.A., Chang, J.H. and Arp, D.J. (2011) The membrane-associated monooxygenase in the butane-oxidizing Gram-positive bacterium *Nocardioides* sp. strain CF8 is a novel member of the AMO/PMO family. *Environmental microbiology reports* 3, 390-396.

Semrau, J.D., DiSpirito, A.A. and Vuilleumier, S. (2011) Facultative methanotrophy: false leads, true results, and suggestions for future research. *FEMS microbiology letters* 323, 1-12.

Smith, K., Dobbie, K., Ball, B., Bakken, L., Sitaula, B., Hansen, S., Brumme, R., Borken, W., Christensen, S. and Priemé, A. (2000) Oxidation of atmospheric methane in Northern European soils, comparison with other ecosystems, and uncertainties in the global terrestrial sink. *Global Change Biology* 6, 791-803.

Titus, J.A., Reed, W.M., Pfister, R. and Dugan, P. (1982) Exospore formation in *Methylosinus trichosporium*. *Journal of bacteriology* 149, 354-360.

Van Beilen, J.B. and Funhoff, E.G. (2007) Alkane hydroxylases involved in microbial alkane degradation. *Applied microbiology and biotechnology* 74, 13-21.

Whittenbury, R., Phillips, K.C. and Wilkinson, J.F. (1970) Enrichment, isolation and some properties of methane-utilizing bacteria. *J Gen Microbiol* 61, 205-218.

Wilson, K. (2001) Preparation of genomic DNA from bacteria. *Curr Protoc Mol Biol* Chapter 2, Unit 2.4.

Yang, S., Wen, X., Jin, H. and Wu, Q. (2012) Pyrosequencing investigation into the bacterial community in permafrost soils along the China-Russia Crude Oil Pipeline (CRCOP). *PLoS One* 7, e52730.

Yang, T., Nigro, L.M., Gutierrez, T., Joye, S.B., Highsmith, R. and Teske, A. (2016) Pulsed blooms and persistent oil-degrading bacterial populations in the water column during and after the Deepwater Horizon blowout. *Deep Sea Research Part II: Topical Studies in Oceanography* 129, 282-291.

Yonemura, S., Yokozawa, M., Sakurai, G., Kishimoto-Mo, A.W., Lee, N., Murayama, S., Ishijima, K., Shirato, Y. and Koizumi, H. (2013) Vertical soil–air CO₂ dynamics at the Takayama deciduous broadleaved forest AsiaFlux site. *Journal of forest research* 18, 49-59.

Zhang, C.-Y., He, Z., Zhang, S., Yin, M.-Y., Ning, Z. and Liu, Y.-C. (2014) Quantitative significance of functional genes of methanotrophs and propanotrophs in soil above oil and gas fields, China. *Journal of Petroleum Science and Engineering* 120, 170-176.

FIGURES AND TABLES

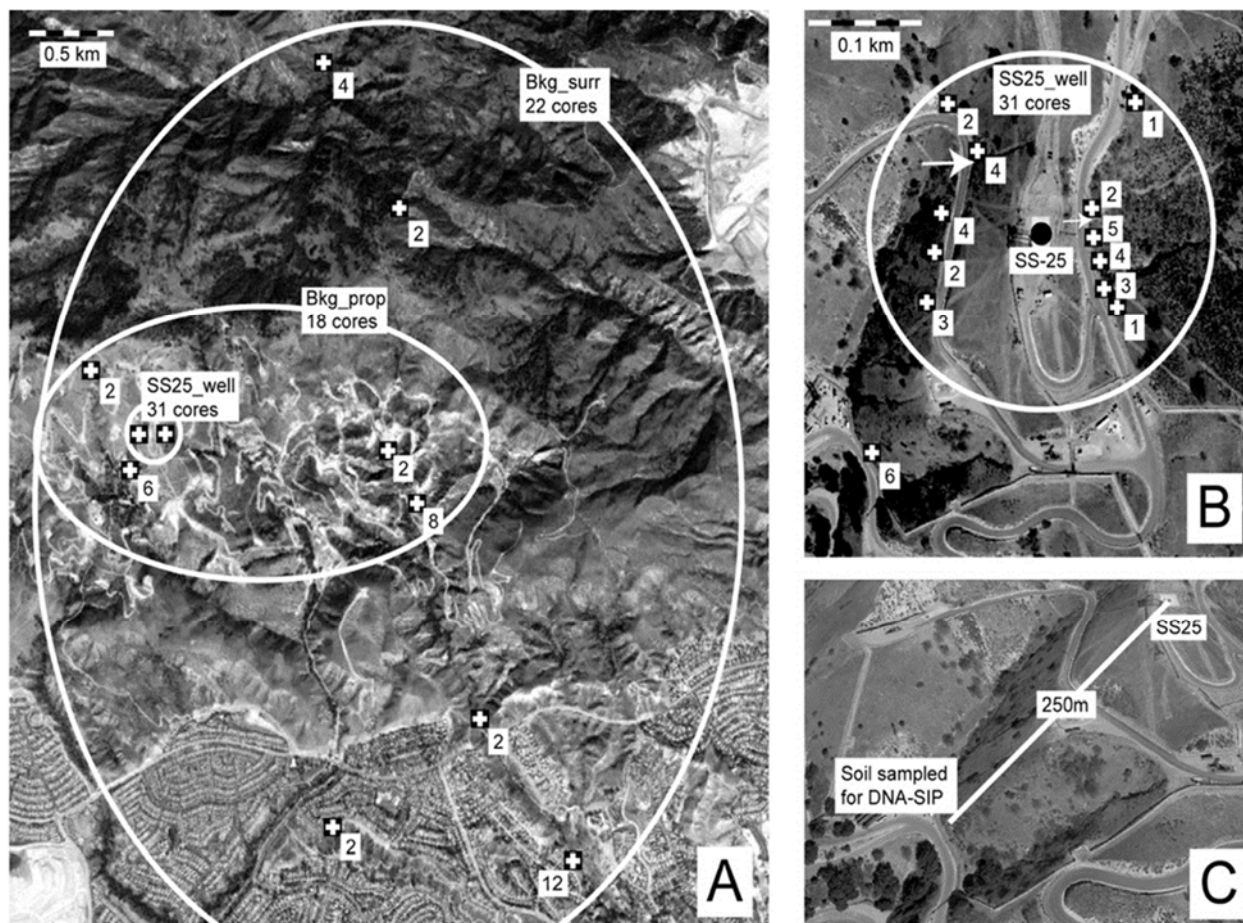


Figure 3.1. Location of the study area. The Aliso Canyon storage facility is in the San Fernando region of California, north of the Porter Ranch residential community. (A) Overview of the area including Porter Ranch, SoCal Gas property, and green space. Sites of coring are indicated with white crosses. Numbers indicate total cores taken at each site. (B) Close-up of the area around failed well SS-25. Sampling sites at multiple points around the well head are indicated. Arrowheads indicate regions of active outgassing identified in January 2016. (C) Angled view of topography showing sampling site for soils used in SIP analysis and relationship to well SS-25. For sampling dates, see Table S3.1.

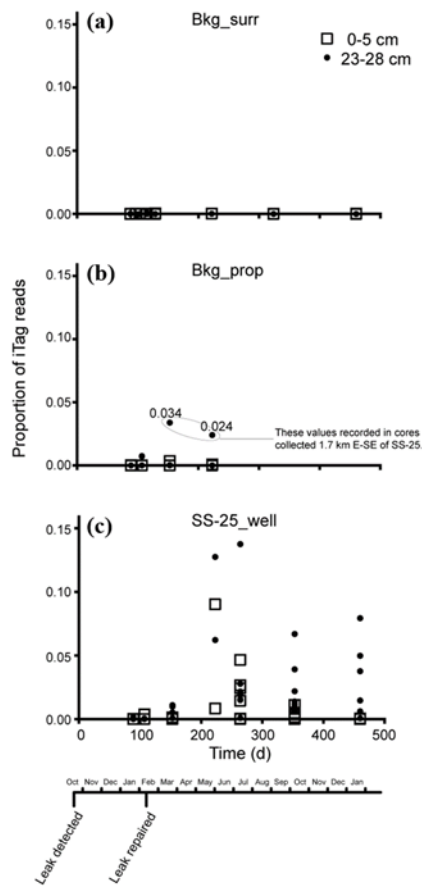


Figure 3. 2. Abundance of methane oxidizing bacteria in environmental samples over time. (a) Background samples surrounding the SoCal Gas property (Bkg_surr, 22 cores.) Methane oxidizing bacteria comprised less than 0.1% of the total microbial population in both 0-5 cm (open squares) and 23 – 28 (filled circles) samples. (b) Background samples on the SoCal Gas property (Bkg_prop, 18 cores.) Methane oxidizing bacteria comprised less than 0.3% of the total microbial population in both 0-5 cm (open squares) and 23 – 28 (filled circles) samples, with the exception of two samples in which they were detected at 2.4 and 3.4% of the population. (c) Samples collected within 150m of the SS-25 wellhead (SS-25_well soils, 31 cores.) Methane oxidizing bacteria comprised up to 13.8% of the total microbial population in multiple samples between March 2016 and January 2017, these dates are subsequent to the repair of well SS-25. Enrichment is more evident in the 23 – 28 cm horizon but also occurs in the 0 – 5 cm horizon.

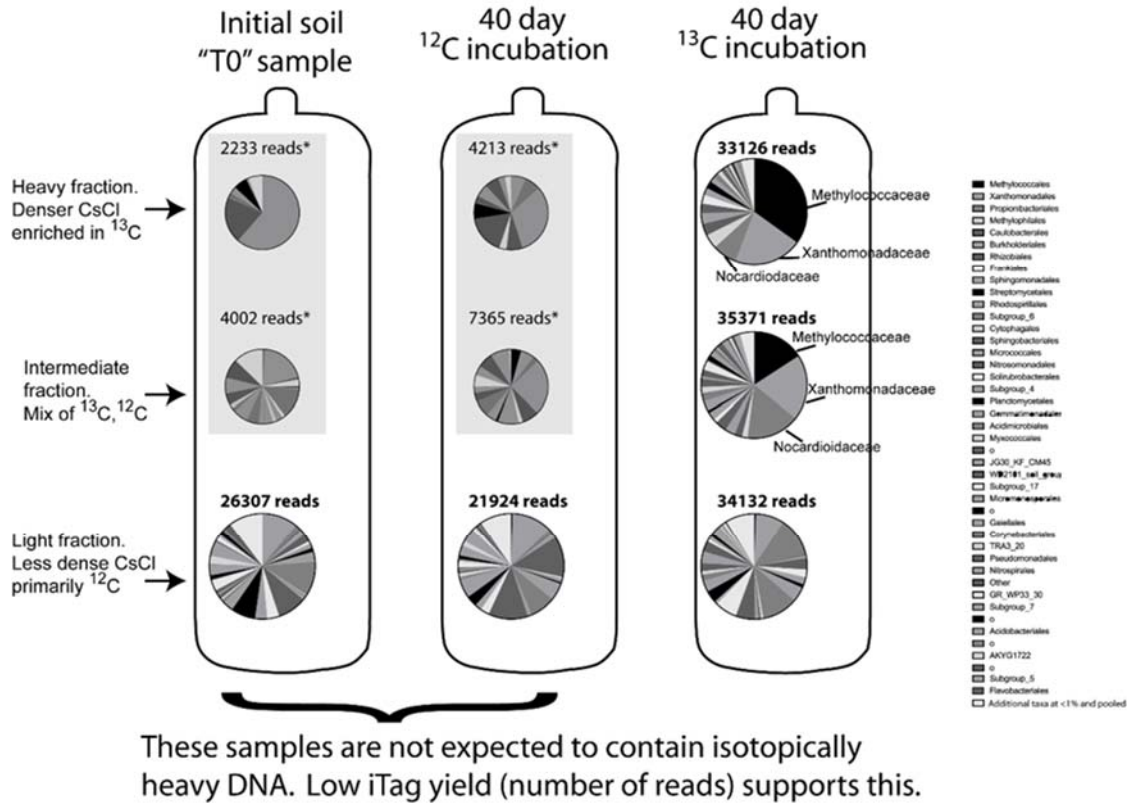


Figure 3.3. ¹³CH₄ DNA SIP. Three soil samples (T₀, ¹²CH₄ incubation, ¹³CH₄ incubation) were analyzed for community composition in SIP. Isotopically heavy DNA was separated from isotopically light DNA in an ultracentrifugation-generated CsCl gradient. Three gradients (heavy, intermediate, light) were collected for each sample and processed with iTAG high throughput sequencing. All three samples generated a strong amplification product from isotopically light DNA, as expected. The T₀ and ¹²CH₄ samples had insufficient DNA to generate a visible PCR product from intermediate or heavy fractions, and generated substantially fewer reads in iTAG. These iTAG results are indicated by shading and asterisks in the figure, and may represent so-called jackpot PCR events. The ¹³CH₄ sample generated a robust amplification product from all three fractions. Isotopically heavy DNA from the ¹³CH₄ incubation was highly enriched in methane-, methanol-, and formate-utilizing microorganisms.

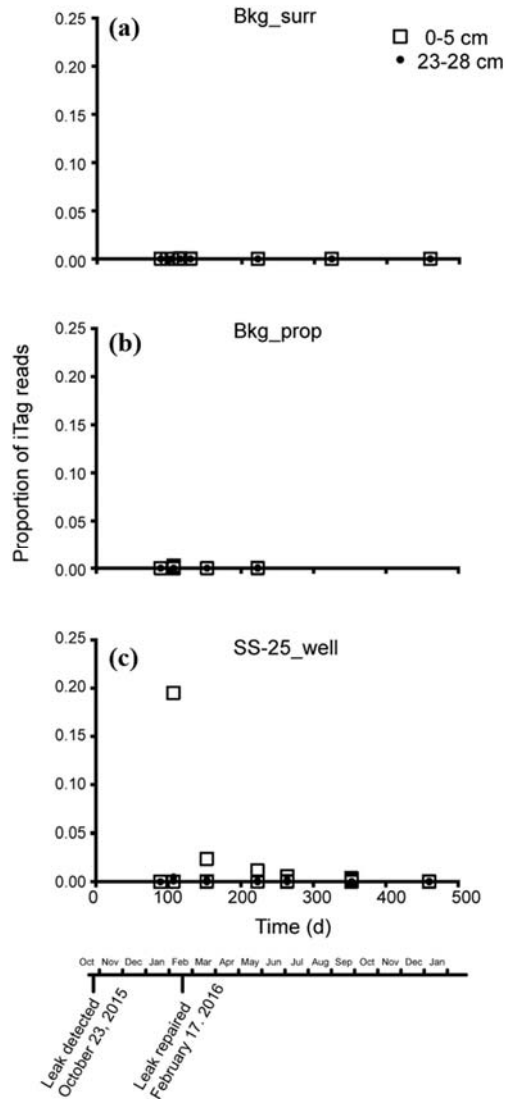


Figure 3. 4. Abundance of *Spingobium* in environmental samples over time. (a-b). Background samples surrounding the SoCal Gas property (Bkg_surr, 22 cores) or on SoCal Gas property (Bkg_prop, 18 cores). *Spingobium* comprised less than 0.3% of the total microbial population in both depth horizons throughout the background sample set (c). Samples collected within 150m of the SS-25 wellhead (SS-25_well soils, 31 cores.) *Spingobium* comprised up to 19.5% of reads at a site of active outgassing in February 2016. Abundance was most pronounced in the 0 – 5 cm horizon. The abundance of *Spingobium* remained above background in multiple SS-25_well soils following the repair of SS-25, but declined significantly with time.

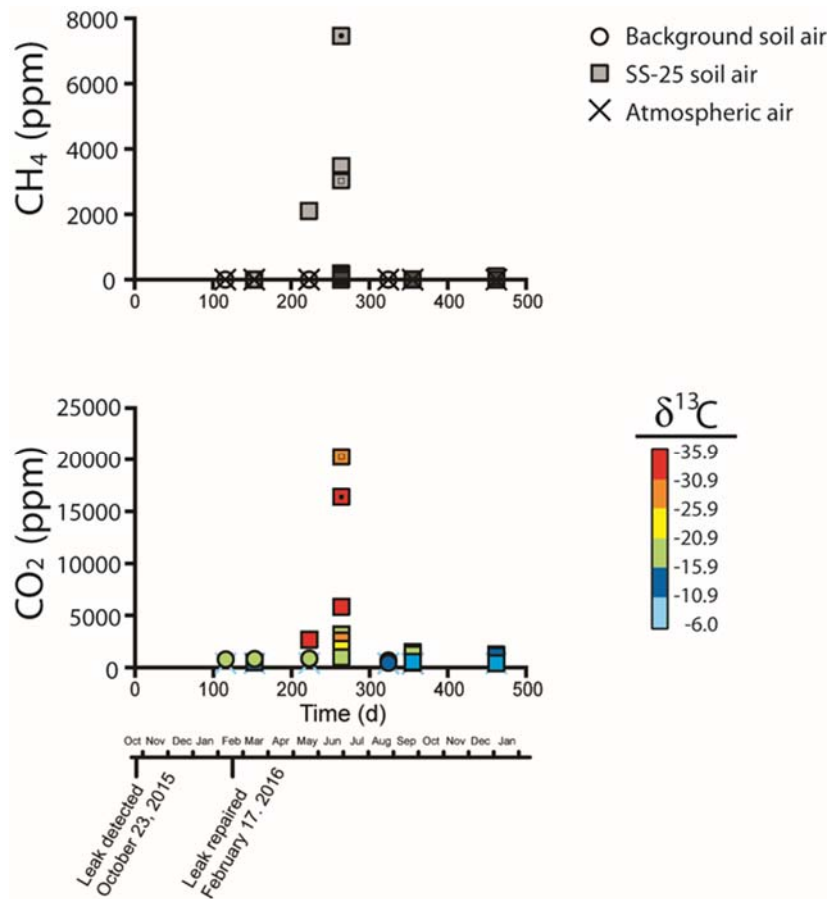


Figure 3. 5. Trace gas analysis in atmospheric and soil air. Cavity ring down spectroscopy was applied to select air samples beginning in February 2016. Select cores were chosen based on localization of outgassing. Representative cores throughout the greater study area were collected as well. Panel A (top). Methane values in soil air near SS-25, but not background cores, were highly elevated in samples collected in June and July 2016, 4 months after SS-25 was sealed. Panel B (bottom). Carbon dioxide values in soil air were highly elevated in SS-25_well samples collected in June and July 2016, but not in background samples. The isotopic composition of CO₂ in these samples is highly depleted in ¹³C, suggesting a relationship between the natural gas and the CO₂ levels. High CO₂ values coincide with samples exhibiting high methane concentrations (see figure S3). Lack of similarly high signal in earlier time points is likely due to insufficient sampling coverage in earlier field trips.

SUPPORTING INFORMATION

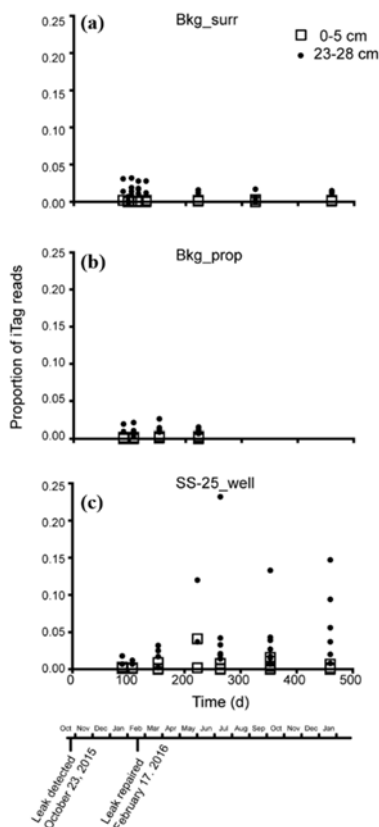


Figure S3. 1. Enrichment of a member of *Rhodospirillaceae* in environmental samples over time. (a) Background samples surrounding the SoCal Gas property (Bkg_surr, 22 cores) and (b) on the SoCal Gas property (Bkg_prop, 18 cores). This *Rhodospirillaceae* comprised less than 3.2% of the microbial population in both 0-5 cm (open squares) and 23 – 28 (filled circles) samples among all background samples. (c) Samples collected within 150m of the SS-25 wellhead (SS-25_well soils, 31 cores.) The member of *Rhodospirillaceae* comprised up to 23.2% of the total microbial population, and was significantly enriched in multiple samples between March 2016 and January 2017, these dates are subsequent to the repair of well SS-25. Enrichment is more evident in the 23 – 28 cm horizon but also occurs in the 0 – 5 cm horizon. This pattern of enrichment is similar to that exhibited by *Methylobacter* over the same time frame.

Relationship between methane, carbon dioxide, geography, and ^{13}C

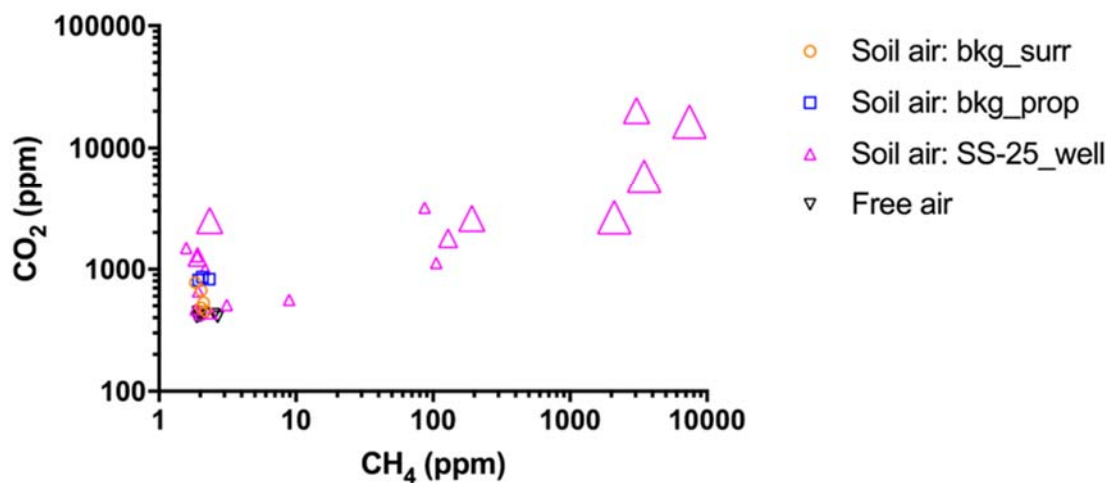


Figure S3. 2. Relationship between CH₄, CO₂, $\delta^{13}\text{C}$, and geography over time. See also Figure 5 in the main document. Atmospheric air (black upside down triangles) contains CO₂ and CH₄ in agreement with multiple independent studies, and $\delta^{13}\text{C}$ value between -8 and -10. Soil air from background samples surrounding the SoCal Gas property (blue squares) has a greater range of CO₂ concentration values, and is generally higher than atmospheric values. Soil air from background samples on the SoCal Gas property (orange circles) is elevated in CO₂ concentration values relative to atmospheric values. Soil air collected near well SS-25 including at sites of active outgassing include samples that are highly enriched in methane, CO₂, and $\delta^{12}\text{C}$ (CO₂).

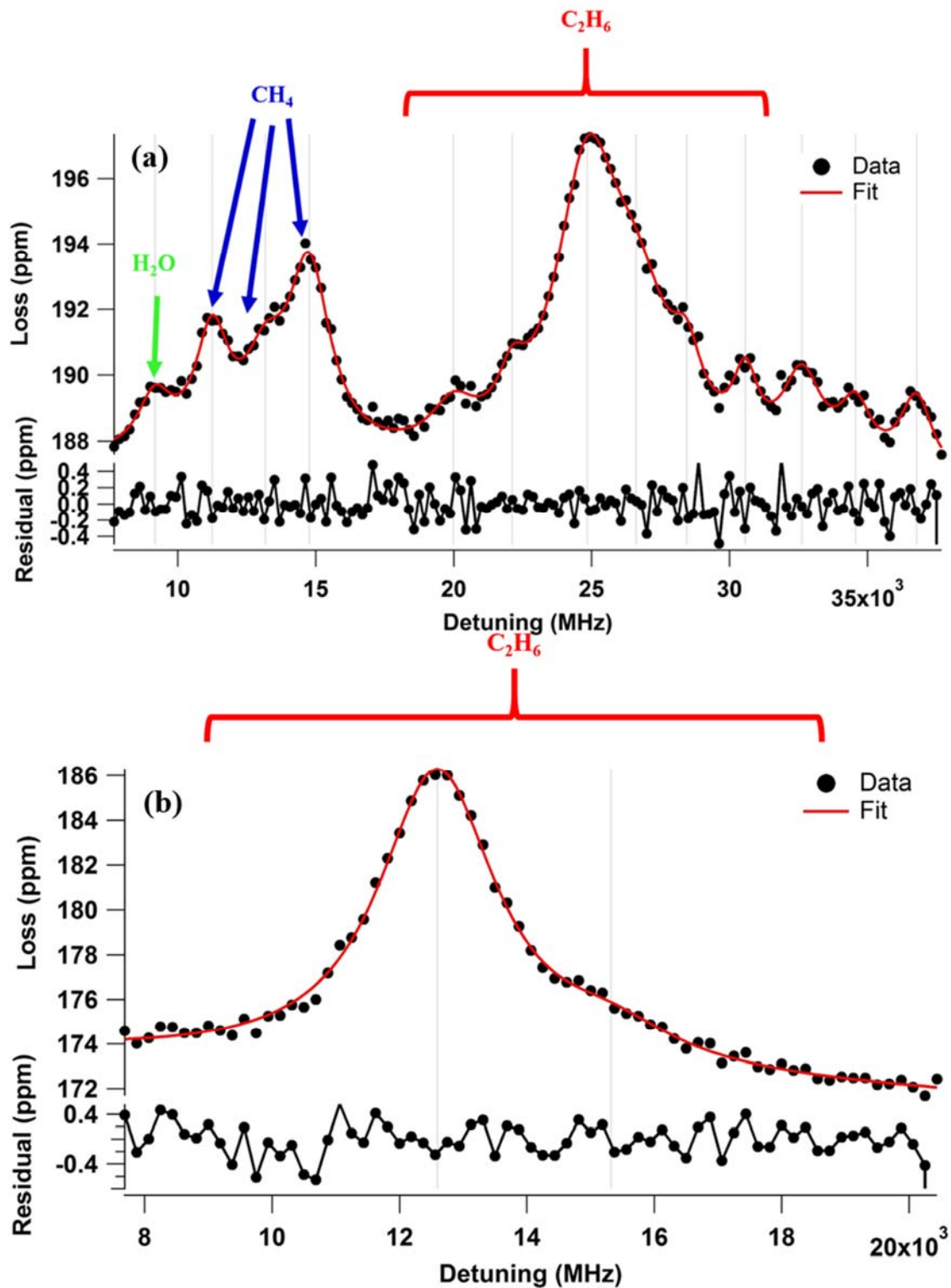


Figure S3.3. Sample spectra of ethane CRDS measurement.

Table S3.1. Table of the sample measurement results. Within the cavity ring-down spectroscopy results, CH₄, CO₂, and δ¹³C of CO₂ were reported from Picarro measurements. The C₂H₆ were measured using the mid-infrared cavity ring-down spectrometer reported in the previous chapter.

Sampling locations and notes							Cavity ring down spectroscopy (soil air)*				GC-MS (soil adsorption)	
Core	Date	Meters from leak	Category (see Fig. 3.1)	Identifier (or well name)	Latitude	Longitude	CH ₄	C ₂ H ₆	CO ₂	δ ¹³ C	CH ₄ 0-5 cm	CH ₄ 23 - 28 cm
1	1/18/2016	4100 SE	Bkg_surr	Laughton Way	34.2888	-118.5329	ND	ND	ND	ND	29.78 +/- 13.95	4.51 +/- 0.60
2	1/18/2016	4100 SE	Bkg_surr	Laughton Way	34.289	-118.5331	ND	ND	ND	ND	35.19 +/- 1.82	75.06 +/- 11.60
3	1/19/2016	84 W	SS-25_well	SS-25 (West)	34.3152	-118.565	ND	ND	ND	ND	942.72 +/- 353.16	867.29 +/- 440.29
4	1/19/2016	87 W	SS-25_well	SS-25 (West)	34.3151	-118.565	ND	ND	ND	ND	532.57 +/- 81.40	626.17 +/- 51.96
5	1/19/2016	270 SW	Bkg_prop	SS-5	34.3132	-118.5656	ND	ND	ND	ND	114.61 +/- 19.35	317.34 +/- 52.94

6	1/19/2016	270 SW	Bkg_prop	SS-5	34.3133	-118.5657	ND	ND	ND	ND	143.5109 +/- 17.47	135.27 +/- 16.83
7	1/27/2016	1960 NE	Bkg_surr	NE of SoCalGas	34.3261	-118.5472	ND	ND	ND	ND	17.83 +/- 13.03	10.41 +/- 2.40
8	1/27/2016	1960 NE	Bkg_surr	NE of SoCalGas	34.3256	-118.5469	ND	ND	ND	ND	3.81 +/- 1.39	10.67 +/- 0.83
9	2/2/2016	4100 SE	Bkg_surr	Laughton Way	34.2891	-118.5332	ND	ND	ND	ND	62.65 +/- 50.57	3.656 +/- 1.58
10	2/2/2016	4100 SE	Bkg_surr	Laughton Way	34.2892	-118.5333	ND	ND	ND	ND	32.7 +/- 30.55	3.71 +/- 0.73
11	2/2/2016	2800 SE	Bkg_surr	Palisades Park	34.2921	-118.5512	ND	ND	ND	ND	28.48 +/- 3.81	24.13 +/- 8.82
12	2/2/2016	2800 SE	Bkg_surr	Palisades Park	34.292	-118.5518	ND	ND	ND	ND	30.86 +/- 21.71	9.03 +/- 3.28
13	2/6/2016	90 NW	SS-25_well	SS-25 (West)	34.3157	-118.5647	ND	ND	ND	ND	160.4667 +/- 25.14	247.78 +/- 106.17
14	2/6/2016	87 W	SS-25_well	SS-25 (West)	34.3152	-118.5649	ND	ND	ND	ND	234.5 +/- 57.63	396.16 +/- 13.51
15	2/6/2016	313 SW	Bkg_prop	SS-5	34.3128	-118.5659	ND	ND	ND	ND	149.42	43.46

											+/- 10.51	+/- 5.40
16	2/6/2016	280 SW	Bkg_prop	SS-5	34.3131	-118.5657	ND	ND	ND	ND	307.234 +/- 39.75	233.67 +/- 65.82
17	2/6/2016	1580 E	Bkg_prop	P-50A	34.3144	-118.5473	ND	ND	ND	ND	94.01 +/- 102.98	26.98 +/- 2.01
18	2/6/2016	1580 E	Bkg_prop	P-50A	34.3144	-118.547	ND	ND	ND	ND	33.53 +/- 4.37	24.11 +/- 0.91
19	2/6/2016	1830 SE	Bkg_prop	Aliso Cyn Wash	34.3115	-118.5452	ND	ND	ND	ND	41.91 +/- 13.87	150.95 +/- 99.15
20	2/6/2016	1830 SE	Bkg_prop	Aliso Cyn Wash	34.3116	-118.5452	ND	ND	ND	ND	29.2 +/- 2.12	40.24 +/- 3.28
21	2/15/2016	2900 SE	Bkg_surr	Aliso Cyn	34.298	-118.5411	ND	ND	ND	ND	17.23 +/- 3.18	40.79 +/- 26.67
22	2/15/2016	2900 SE	Bkg_surr	Aliso Cyn	34.2981	-118.541	ND	ND	ND	ND	15.09 +/- 3.64	7.1 +/- 0.91
23	2/15/2016	2800 NE	Bkg_surr	Rice Cyn	34.3383	-118.5517	ND	ND	ND	ND	33.59 +/- 1.78	34.93 +/- 4.54
24	2/15/2016	2800 NE	Bkg_surr	Rice Cyn	34.3378	-118.5517	1.84	1.42	777.79	-15.06	28.24	22.97

							+/- 0.01	+/- 0.08	+/- 0.05	+/- 0.07	+/- 2.25	+/- 1.52
25	2/29/2016	4100 SE	Bkg_surr	Laughton Way	34.2887	-118.5329	ND	ND	ND	ND	10.69 +/- 2.30	5.12 +/- 1.92
26	2/29/2016	4100 SE	Bkg_surr	Laughton Way	34.2892	-118.5332	ND	ND	ND	ND	55.78 +/- 33.52	87.47 +/- 24.79
27	3/24/2016	85 W	SS-25_well	SS-25 (West)	34.3151	-118.565	ND	ND	ND	ND	152.69 +/- 17.45	106.13 +/- 18.44
28	3/24/2016	90 NW	SS-25_well	SS-25 (West)	34.3157	-118.5647	3.12 +/- 0.01	25.21 +/- 0.16	507.04 +/-0.05	-12.84 +/-0.16	132.01 +/- 17.71	245.41 +/- 34.67
29	3/24/2016	40 E	SS-25_well	SS-25 (East)	34.315	-118.5636	ND	ND	ND	ND	228.69 +/- 38.60	250.16 +/- 20.33
30	3/24/2016	59 SE	SS-25_well	SS-25 (East)	34.3148	-118.5636	ND	ND	ND	ND	198.58 +/- 43.79	185.61 +/- 40.65
31	3/24/2016	270 SW	Bkg_prop	SS-5	34.3134	-118.5659	ND	ND	ND	ND	169.49 +/- 87.36	173.02 +/- 56.73
32	3/24/2016	278 SW	Bkg_prop	SS-5	34.3134	-118.5661	ND	ND	ND	ND	183.07 +/- 53.93	228.28 +/- 51.41

33	3/24/2016	1830 SE	Bkg_prop	Aliso Cyn Wash	34.3115	-118.5453	1.95 +/- 0.00	4.17 +/- 0.21	813.01 +/- 0.04	-16.78 +/-0.04	37.36 +/- 2.03	11.02 +/- 6.42
34	3/24/2016	1830 SE	Bkg_prop	Aliso Cyn Wash	34.3114	-118.5452	ND	ND	ND	ND	48.32 +/- 10.15	11.47 +/- 1.35
35	6/1/2016	4100 SE	Bkg_surr	Laughton Way	34.2892	-118.5332	ND	ND	ND	ND	67.71 +/- 8.43	60.98 +/- 0.88
36	6/1/2016	4100 SE	Bkg_surr	Laughton Way	34.2891	-118.5331	ND	ND	ND	ND	35.67 +/- 16.04	130.64 +/- 93.41
37	6/2/2016	40 E	SS-25_well	SS-25 (East)	34.3151	-118.5636	2106.0 +/- 0.50	1963.3 +/- 0.09	2675.07 +/- 0.33	-35.46 +/- 0.12	167.71 +/- 41.23	157.18 +/- 31.63
38	6/2/2016	47 SE	SS-25_well	SS-25 (East)	34.3149	-118.5636	ND	ND	ND	ND	180.61 +/- 24.72	157.46 +/- 33.70
39	6/2/2016	290 SW	Bkg_prop	SS-5	34.3134	-118.5663	2.07 +/- 0.04	10.3 +/- 0.497	864.16 +/- 0.17	-15.84 +/- 0.10	245.03 +/- 57.33	ND
40	6/2/2016	260 SW	Bkg_prop	SS-5	34.3136	-118.566	ND	ND	ND	ND	165.44	ND

												+/- 123.67	
41	6/2/2016	1830 SE	Bkg_prop	Aliso Cyn Wash	34.3116	-118.5453	2.32 +/- 0.01	8.18 +/- 0.35	829.55 +/- 0.06	-18.41 +/- 0.07	32.42 +/- 3.82	26.01 +/- 2.09	
42	6/2/2016	1830 SE	Bkg_prop	Aliso Cyn Wash	34.3114	-118.5452	ND	ND	ND	ND	27.24 +/- 7.90	18.02 +/- 4.01	
43	6/2/2016	540 NW	Bkg_prop	SS-21	34.3188	-118.5681	ND	ND	ND	ND	107.9 +/- 15.80	109.73 +/- 20.52	
44	6/2/2016	540 NW	Bkg_prop	SS-21	34.3192	-118.5681	ND	ND	ND	ND	382.29 +/- 493.94	79.03 +/- 13.28	
45	7/13/2016	96 SE	SS-25_well	SS-25 (East)	34.3145	-118.5634	2.35 +/- 0.004	3.2 +/- 0.14	2508.36 +/- 0.38	-27.5 +/- 0.05	120 +/- 33.04	183.19 +/- 39.13	
46	7/13/2016	70 SE	SS-25_well	SS-25 (East)	34.3147	-118.5635	3475.4 +/- 0.44	NA	5827.44 +/- 0.20	-32.18 +/- 0.12	45.31 +/- 52.31	197.17 +/- 118.10	
47	7/13/2016	61 SE	SS-25_well	SS-25 (East)	34.3148	-118.5635	192.37	NA	2603.28	-26.62	259.69	229.35	

							+/- 0.04		+/- 0.08	+/- 0.09	+/- 126.41	+/- 50.60
48	7/13/2016	41 E	SS-25_well	SS-25 (East)	34.3151	-118.5636	7463.9 +/- 0.64	NA	16411.12 +/- 0.7	-31.62 +/- 0.13	247.71 +/- 13.99	199.53 +/- 74.24
49	7/13/2016	48 NE	SS-25_well	SS-25 (East)	34.3153	-118.5636	129.12 +/- 0.01	11.8 +/- 0.009	1791.75 +/- 0.15	-21.52 +/- 0.04	201.79 +/- 30.42	167.83 +/- 37.81
50	7/13/2016	115 NW	SS-25_well	SS-25 (West)	34.3159	-118.5648	3052.4 +/- 0.387	NA	20275.71 +/- 1.33	-30.09 +/- 0.05	156.88 +/- 16.91	140.83 +/- 0.85
51	7/13/2016	94 W	SS-25_well	SS-25 (West)	34.315	-118.565	86.862 +/- 0.015	NA	3181.35 +/- 0.06	-15.5 +/- 0.04	148.15 +/- 3.63	176.84 +/- 0.91
52	7/13/2016	103 SW	SS-25_well	SS-25 (West)	34.3148	-118.5651	2.172 +/- 0.003	1.35	1001.66 +/- 0.06	-18.12 +/- 0.04	ND	433.42 +/- 43.71
53	9/11/2016	2800 NE	Bkg_surr	Rice Cyn	34.3382	-118.5519	2.03	7.5		-10.99	ND	ND

							+/- 0.00	+/- 1.72	482.98 +/- 0.01	+/- 0.19		
54	9/11/2016	2800 NE	Bkg_surr	Rice Cyn	34.3378	-118.5517	2.19 +/- 0.01	11.4 +/- 2.44	453.27 +/- 0.04	-10.08 +/- 0.09	ND	ND
55	9/11/2016	4100 SE	Bkg_surr	Laughton Way	34.2891	-118.5332	2.03 +/- 0.00	22.64 +/- 6.57	668.40 +/- 0.06	-14.11 +/- 0.13	ND	ND
56	9/11/2016	4100 SE	Bkg_surr	Laughton Way	34.2892	-118.5333	2.12 +/- 0.00	9.76 +/- 0.85	532.52 +/- 0.04	-12.45 +/- 0.14	ND	ND
57	10/10/2016	92 NW	SS-25_well	SS-25 (West)	34.3157	-118.5647	1.85 +/- 0.00	N/A	466.94 +/- 0.03	-10.90 +/- 0.14	ND	ND
58	10/10/2016	99 W	SS-25_well	SS-25 (West)	34.3148	-118.565	1.58 +/- 0.00	N/A	1496.04 +/- 0.14	-18.11 +/- 0.06	ND	ND
59	10/10/2016	133 NW	SS-25_well	SS-25 (West)	34.3161	-118.5649	ND	ND	ND	ND	ND	ND

60	10/10/2016	42 E	SS-25_well	SS-25 (East)	34.315	-118.5636	1.9 +/- 0.01	N/A	1277.74 +/- 164.55	-18.93 +/- 0.09	ND	ND
61	10/10/2016	145 NE	SS-25_well	SS-25 (East)	34.3162	-118.5632	8.93 +/- 10.10	N/A	559.43 +/- 0.04	-10.10 +/- 2.16	ND	ND
62	10/10/2016	64 SE	SS-25_well	SS-25 (East)	34.3148	-118.5635	ND	ND	ND	ND	ND	ND
63	10/10/2016	45 NE	SS-25_well	SS-25 (East)	34.3152	-118.5636	ND	ND	ND	ND	ND	ND
64	1/25/2017	91 NW	SS-25_well	SS-25 (West)	34.3156	-118.5647	1.97 +/- 0.003	6.9 +/- 1.08	427.81 +/- 0.027	-9.94 +/- 0.090	142.12 +/- 38.21	157.67 +/- 45.90
65	1/25/2017	102 SW	SS-25_well	SS-25 (West)	34.3148	-118.565	1.93 +/- 0.003	4.74 +/- 0.58	657.65 +/- 0.063	-14.66 +/- 0.126	280.67 +/- 109.69	113.79 +/- 5.00
66	1/25/2017	86 W	SS-25_well	SS-25 (West)	34.3151	-118.565	ND	ND	ND	ND	125.38 +/- 15.04	120.5 +/- 45.27
67	1/25/2017	40 E	SS-25_well	SS-25 (East)	34.3151	-118.5636	1.91	N/A	1259.053	-23.15	177.18	204.44

							+/- 0.003		+/- 0.125	+/- 0.084	+/- 30.48	+/- 27.85
68	1/25/2017	66 SE	SS-25_well	SS-25 (East)	34.3147	-118.5635	2.41 +/- 0.14	0.43 +/- 0.062	436.43 +/- 1.40	-8.86 +/- 0.17	124.84 +/- 18.02	130.99 +/- 34.59
69	1/25/2017	55 SE	SS-25_well	SS-25 (East)	34.3148	-118.5636	105.77 +/- 75.28	2.51 +/- 0.2	1125.76 +/- 531.7	-17.34 +/- 7.24	145.12 +/- 27.47	151.46 +/- 10.03
70	1/25/2017	4100 SE	Bkg_surr	Laughton Way	34.2892	-118.5332	ND	ND	ND	ND	58.95 +/- 36.86	99.99 +/- 84.16
71	1/25/2017	4100 SE	Bkg_surr	Laughton Way	34.2891	-118.5332	ND	ND	ND	ND	110.26 +/- 129.26	79.87 +/- 2.71

**Chapter 4: Measurements of Doubly-Substituted Methane Isotopologues
by Frequency Stabilized Mid-IR Cavity Ring-Down Spectroscopy**

ABSTRACT

Measurements of the abundances of doubly-substituted methane isotopologues ($^{13}\text{CH}_3\text{D}$ and $^{12}\text{CH}_2\text{D}_2$) are important in methane source attributions.(Stolper et al., 2014a) Currently, methods developed for $^{13}\text{CH}_3\text{D}$ and $^{12}\text{CH}_2\text{D}_2$ measurements have been mostly focused on the use of isotope ratio mass spectrometry (IRMS), which faces the challenges of mass resolutions. In this work, we focus on measuring these low abundant methane isotopologues optically, taking advantage of the distinct absorption features of them. Spectroscopy measurements of $^{13}\text{CH}_3\text{D}$ in naturally abundant methane have been demonstrated using a multi-pass direct absorption technique.(Ono et al., 2014) Measurement of the lower abundant $^{12}\text{CH}_2\text{D}_2$ has remained a challenge.

We demonstrate high sensitivity measurements of both $^{13}\text{CH}_3\text{D}$ and $^{12}\text{CH}_2\text{D}_2$ isotopologues using a high precision and high resolution spectroscopy technique, frequency stabilized cavity ring-down spectroscopy (FS-CRDS). The frequency range of the spectrometer is 2200 cm^{-1} to 2300 cm^{-1} , which provides capability to detect the five highest abundant methane isotopologues. The cavity ring-down method uses two highly reflective mirrors to increase the effective pathlength of laser light up to 5km inside the optical cavity, increasing the sensitivity significantly from traditional absorption techniques. The physical length of the cavity is actively stabilized with respect to a frequency stabilized He/Ne laser, which improves the sensitivity and precision of the spectrometer. This technique can be used as a potential complement to IRMS measurements for its ability to measure abundances of rare methane isotopologues with a short time average (~ 1 hour average per isotope ratio measurement).

INTRODUCTION

Methane is the most abundant hydrocarbon in the Earth atmosphere, is also an important greenhouse gas, energy source, and microbial metabolic energy source and product.(Ferry, 1998; Hinrichs et al., 1999; Ramaswamy, 2001; Thauer, 1998; Wuebbles, 2002) Atmospheric methane monitoring since 1983 has provided us more understanding of its dynamics. The methane growth rate slowly decreased since the beginning of the direct monitoring of the atmosphere, until it reached a relative plateau in the early 2000 s. However, methane concentration has started increase rapidly since 2007 at more than 10 times the rate between 2000 and 2006.(Butler and Montzka, 2017; Dlugokencky et al., 2011; Saunio et al., 2016) Despite its environmental and economic importance, much of the formation and destruction mechanisms remains poorly constrained. This rapid change in the last decay calls for response in methane source identifications and possibilities of emission control.

The methods of methane source attribution include isotopic composition measurement and methane coemitting gas measurement. Isotope composition measurements uses the correlation between the $\delta^{13}\text{C}$ and δD of the methane to identify methane sources, shown in Fig. 1.3.(Schoell, 1980; Whiticar, 1999) The carbon and hydrogen isotope ratios of CH_4 generated are fundamental parameters for interpreting gas origins in natural settings, including abiotic methane and biotic methane.(Etiope and Lollar, 2013; McCollom, 2013; Stolper et al., 2015) In general, more negative $\delta^{13}\text{C}$ and δD values indicate biogenic sources, while more positive $\delta^{13}\text{C}$ and δD values indicate thermogenic sources.(Bernard et al., 1976; Douglas et al., 2016; Schoell, 1983; Whiticar, 1999) On the other hand, the biogenic methane produced by methanogens contains only pure methane while many thermogenic gases contain not only methane, but larger hydrocarbons such as ethane, propane, and butane.(Bernard et al., 1976; Claypool and

Kvenvolden, 1983) Complimentary analysis of both the methane isotope and higher order hydrocarbon compositions were used when detailed methane source attribution is needed.

However, there have been examples in which both these parameters fail. Thus, an additional parameter to distinguish biogenic and thermogenic methane from each other is needed. One method is to differentiate them by their formation temperature, biogenic sources produce methane with temperatures significantly lower. The formation temperature of the methane could be determined with measurement of the abundance of the doubly substituted methane isotopologues, $^{13}\text{CH}_3\text{D}$ and $^{12}\text{CH}_2\text{D}_2$.(Stolper et al., 2014a; Yeung et al., 2012; Young et al., 2017; Young et al., 2016) However, these methane isotopologues have been challenging to measure mostly due to their very low abundance compare to the singly substituted isotopologues. Currently, methods developed for $^{13}\text{CH}_3\text{D}$ and $^{12}\text{CH}_2\text{D}_2$ measurements have been mostly focused on the use of isotope ratio mass spectrometry (IRMS), which faces the challenges of mass resolutions. Eiler et al. has demonstrated an IRMS instrument, in which the combined abundance of $^{13}\text{CH}_3\text{D}$ and $^{12}\text{CH}_2\text{D}_2$ were measured. (Douglas et al., 2016; Eiler et al., 2013a; Eiler et al., 2013b; Stolper et al., 2014a; Stolper et al., 2014b) In 2016, Young et al. developed a prototype mass spectrometer capable of resolving the two mass-18 isotopologues for high-precision isotope ratio analysis.(Young et al., 2017; Young et al., 2016)

Recent works by Ono et al has developed a direct absorption based analyzer for the higher abundant doubly substituted methane, $^{13}\text{CH}_3\text{D}$, and used this technique to study temperature dependent kinetic isotope effect of methane oxidation by OH and Cl radicals, which are important atmospheric methane removers.(Joelsson et al., 2016; Ono et al., 2014; Whitehill et al., 2017) In this work, we demonstrated the first optical observation of $^{12}\text{CH}_2\text{D}_2$ using a frequency stabilized cavity ring-down spectrometer (FS-CRDS).

METHODS

The spectrometer was designed based on the one designed by Hodges et al. (Hodges and Ciuryło, 2005; Hodges et al., 2004; Lisak et al., 2010). A schematic of the spectrometer is shown in Fig 4.1. The mid-infrared light source used for doubly substituted methane isotopologue measurement is a commercial 4.5 μm external cavity quantum cascade laser (EC-QCL, Daylight Solutions 41043-MHF), which has a tenability range of 2195 cm^{-1} – 2313 cm^{-1} . The output power of the laser varies between 80 mW to 175 mW. The laser output first passes through two free-space optical isolators (Thorlabs, IO-4-4500-WG, and Electro-Optics Technology, Inc., Mesos Series 4500 – 4600 nm Mid-IR optical isolator) sequentially to eliminate residual back reflections from optical elements perpendicular to the beam, which can prohibit the laser from reliably tune as a single-mode light source. A small amount of the MIR light (< 1 %) was picked off with a MgF_2 window to send into a wavemeter (Bristol, 621A-IR) for laser frequency monitoring, while the rest of the light was collimated and shaped prior to entering the acousto-optic modulator (AOM, Brimrose, GEM-40-4-4400, active crystal size 0.8 mm diameter), which was used as an optical shutter. The first order output beam from the AOM was then sent into the ring-down cavity.

The ring-down cavity was constructed with two plano/concave dual coated high reflective ZnSe substrate mirrors (LohnStar Optics) with 99.985% reflectivity at 4.5 μm and 95% reflectivity at 633 nm, with 6 m radius of curvature. These two mirrors were placed ~ 1.5 meters away from each other with one of them mounted on a low voltage ring piezo actuator (PZT, Piezomech GmbH, HPSt 150/14-10/40 VS22), yielding an effective pathlength of ~ 10 km. This distance was chosen with the considerations of having closely spaced cavity modes and long light molecule interaction pathlength without sacrificing large amount of photons reaching

the detector. The two ring-down mirror mounts were then mounted on a set of four 2.54 cm diameter low-thermal expansion stainless steel rods to enhance system rigidity and minimize thermal expansion effects. Light transmitted from the cavity was focused with a 20 mm focal length lens into a liquid nitrogen cooled indium antimonide (InSb) detector (InfraRed Associates Inc., IS-1.0) with an impedance matched low noise and adjustable gain pre-amplifier (INSB-1000). The electrical bandwidth of the pre-amplifier was set to 1.5 Hz to 3 MHz.

In order to increase the sensitivity of the spectrometer and precision of the measurements, the length of the optical cavity is actively stabilized to a frequency stabilized HeNe reference laser (Micro-g LaCoste ML-1) which has a reported frequency stability of 500 kHz/ 24 hours. Unlike the transmission lock employed by Hodges et al., the locking method used here for the cavity length stabilization is the Pound-Drever-Hall (PDH) lock, which generates an “error signal” proportional to the difference between the laser and the cavity line centers.(Black, 2001; Paldus et al., 1998) The PDH locking method is used due to the low power of the frequency stabilized HeNe reference laser and the large absorption loss of the 632 nm light through the high reflectivity cavity mirrors. As shown in Fig 4.1, a free-space electro-optic modulator (Thorlabs, EO-PM-NR-C1) was used as the phase modulator, which was driven by a function generator (SRS, DS345) set to 20.1 MHz. The HeNe light was polarized prior to the EOM and the modulated beam was injected into the cavity by combining it with the 4.5 μm MIR light using a dichroic mirror (Rocky Mountain Instrument Company, RT1012C0634204) anti-reflective (AR) coated for 4.5 μm light ($T_{\text{avg}} > 95\%$, $R_{\text{avg}} < 1\%$ at 3.9 – 4.5 μm , 45°) and high reflectivity coated for 633 nm light ($R > 99.5\%$ at 633 nm, 45°). Optical signal reflected from the ring-down cavity was measured with a silicon photodiode (New Focus, model 1801, 125 MHz bandwidth) after passing through a quarter waveplate along with a polarizing beam splitter. The detector signal

was then amplified, filtered, and phase-sensitively demodulated using a lock-in amplifier (SRS, SR844). The PDH error signal generated from the lock-in amplifier was then processed through a feedback servo circuit (Vescent, D2-125 Laser Servo) to generate a correction signal. The correction signal was sent to the PZT to actively control the cavity length. The cavity lock was obtained by manually adjust the offset on the PZT driver until the cavity TEM₀₀ mode cavity enters the locking range of the servo. We have observed that after the lock was achieved, the cavity length remains locked to the HeNe laser for up to 3 hours, before external perturbations, such as mechanical and acoustic vibrations and the temperature dependent residual amplitude modulation from the EOM, moves the system beyond the range of the servo. The transmission of the 633 nm light was monitored using a silicon avalanche photodiode (Thorlabs, APD130A2) after separation from the probe light with an identical dichroic mirror as above.

Starting frequency of each spectrum was set by the laser controller and verified with the wavemeter. Spectra were acquired by tuning and locking the MIR probe laser frequency to successive longitudinal modes of the frequency stabilized cavity (FS-CRDS). As previously demonstrated, this approach provides great linear spectrum frequency axis with equal spaced steps one free-spectral range (FSR) from each other. Although frequency stepping capability was built in the laser controller, the minimum tuning step is too coarse for our experiment. Thus, the frequency tuning of the laser was achieved by externally changing the voltage (Thorlabs, MDT694B) towards the piezo of the external cavity of the laser. The non-linear frequency tuning from the piezo stepping was subsequently corrected by a slow current modulation to the laser head to achieve the lock between the laser frequency and the stabilized optical cavity. After laser frequency was locked to the cavity modes, 200 ring-down decays were averaged at each frequency with an acquisition rate of ~ 50 Hz. Each ring-down event was initiated by

transmission signals detected by the InSb detector exceeding a set amplitude threshold triggering the generation of a TTL pulse from a digital delay generator, which switches off the first order diffracted beam from the AOM. Each ring-down event was digitized by an analog-to-digital board and fitted with an exponential decay to retrieve the decay time constant, τ .

Since the cavity FSR is a function of both the physical cavity length (l) and the refractive index, n , it is very crucial for us to precisely measure the FSR at a few working pressures. The measurement was based on the procedure reported by Hodges et al. (Lisak et al., 2010). After tuning and locking the laser frequency to each successive cavity mode, the laser frequency was recorded by the Bristol wavemeter. Thus, the uncertainty of the FSR measurement is only from the uncertainty of the wavemeter frequency measurement. The measured FSR of the cavity is 98.05 MHz.

Total pressure of the FS-CRDS cell was monitored with a 1000 Torr Baratron, while the temperature of the cavity was monitored at three different locations along the 1.5-meter cavity with stick on thermistor sensors (Omega, SA1-TH-4408-40-T) to ensure temperature stability and uniformity. The cavity was evacuated before and after each methane sample analysis with a turbo pump to 1.0×10^{-5} Torr. All pumps used for these experiments were oil free to eliminate possible hydrocarbon contaminations to the spectrometer.

RESULTS AND DISCUSSION

Spectrometer Sensitivity

Figure 4.2 shows the Allan deviation plot of the baseline losses at 2268.00 cm^{-1} , collected for up to 20,000 ring-down decay acquisitions at a rate of $\sim 50 \text{ Hz}$. The Allan

deviation displays a power law relationship with respect to the number of ring-down acquisitions, where the fitted slope is -0.35. It can be shown in the Allan deviation plot that white noise dominates up to ~ 500 ring-down decays, which corresponds to approximately 50 seconds of ring-down time averaging. We achieved a typical detectable absorbance of $\alpha_{\min} \sim 1.49 \times 10^{-10} \text{ cm}^{-1}$, which translates to the noise equivalent absorption (NEA) of $4.7 \times 10^{-10} \text{ cm}^{-1} \text{ Hz}^{-1/2}$.

Line Searches

Among different possible methane infrared absorption bands, we chose to perform the measurements of the two doubly substituted methane isotopologues ($^{13}\text{CH}_3\text{D}$, $^{12}\text{CH}_2\text{D}_2$) in the $4.5 \mu\text{m}$ region, which covers most of the fundamental stretch ro-vibrational bands of these two molecules. This region is chosen to minimize interference from two highest abundant isotopologues ($^{12}\text{CH}_4$ and $^{13}\text{CH}_4$). However, line parameters of $^{13}\text{CH}_3\text{D}$ and $^{12}\text{CH}_2\text{D}_2$ are not well known in this region. In order to identify absorption transition positions and relative strengths for these doubly substituted methane isotopologues, high resolution Fourier transformation infrared (FTIR) spectroscopy measurements of 5 Torr pure samples were done in the same spectral region as the tuning region of the EC-QCL laser. Line positions were verified by measurement of diluted pure $^{13}\text{CH}_3\text{D}$ (synthesized) and $^{12}\text{CH}_2\text{D}_2$ (Sigma-Aldrich, 486841-1L) 50 ppb in nitrogen. The relative strength of these transitions were normalized to the FS-CRDS measurement of 5 Torr pure natural abundance methane sample in the spectral windows of $2224.0 \text{ cm}^{-1} - 2224.5 \text{ cm}^{-1}$, $2228.6 \text{ cm}^{-1} - 2229.0 \text{ cm}^{-1}$, $2231.5 \text{ cm}^{-1} - 2232.0 \text{ cm}^{-1}$, and $2269.5 \text{ cm}^{-1} - 2271.0 \text{ cm}^{-1}$. Normalized spectra of the most abundant five isotopologues of methane ($^{12}\text{CH}_4$, $^{13}\text{CH}_4$, $^{12}\text{CH}_3\text{D}$, $^{13}\text{CH}_3\text{D}$, and $^{12}\text{CH}_2\text{D}_2$) are plotted in Fig. 4.3 with the first three simulated from the HITRAN database and the last two from the normalized FTIR broadband measurements. (Gordon et al., 2017)

Lineshape Study

In order to accurately and precisely measure the concentration of each isotopologue, areas under each absorption transition needs to be integrated by fitting with a line profile which best describes the lineshape of the absorption line. The spectrometer performance was first used to study the spectrum of a known $^{12}\text{CH}_3\text{D}$ transition with pure natural abundance methane. The spectral line measured is centered at 2278.775 cm^{-1} , which as a reported ground state energy of 350.1516 cm^{-1} .(Gordon et al., 2017) It has been previously shown that the Voigt profile is not sufficient in modeling high resolution molecular spectra.(Bui et al., 2014; Lisak et al., 2006; Lisak et al., 2010; Long et al., 2011a; Long et al., 2012; Long et al., 2011b) This line profile model only takes into account of the free motion of the absorber assuming Maxwellian distribution based of the absorber velocity (Doppler lineshape), and the collisional broadening (Lorentzian lineshape) and collisional shift independent of the absorber velocity. The measured spectrum was fitted with a Galatry line profile, which includes a narrowing effect from collisions.(Dicke, 1953; Galatry, 1961; Hubbert and Troup, 1977) This line profile is based on the soft-collision model and assumes that a single collision cannot effect the velocity of the absorber. This soft-collision model is more applicable when absorption spectrum of a light perturber is in question, such as in our case of methane spectroscopy. The Dicke narrowing coefficient (η) can be estimated from the mass diffusion coefficient (D), the absorber mass (m_a), and the pressure (p) and temperature (T) of the absorber with the equation:

$$\eta_{Dicke} = \frac{k_B T}{2\pi m_a D p} \quad (\text{Eq. 4. 1})$$

The line width parameters can be expressed as the following:

$$\Gamma_G = \Gamma_D (1 + \eta_{Dicke} \times p) \quad (\text{Eq. 4. 2})$$

$$\Gamma_D = \sqrt{\frac{8k_B T \ln 2}{m_a c^2}} v_{center} \quad (\text{Eq. 4. 3})$$

$$\Gamma_L = \eta_p \times p \quad (\text{Eq. 4. 4})$$

Where Γ_G and Γ_L are Gaussian and Lorentzian widths, respectively, v_{center} is the center of the measured absorption transition, and η_p is the pressure broadening coefficient. Figure 4.4 shows an example comparing fits using the traditional Voigt profile and the Galatry profile for pure methane at 20 Torr in the spectrally isolated regime.

This same transition was measured at pressures between 1.4 Torr and 63.2 Torr to verify the performance of the spectrometer. Figure 4.5a shows the five individual spectra collected for the pressure dependent study. The spectra were plotted without baseline correction. Each spectrum was fitted to a Galatry profile with fixed Doppler width calculated from measured temperature and only vary the Dicke narrowing coefficient and the pressure broadening. The integrated areas of these lines and full width half maximum of the Lorentzian line profile are retrieved from the fits and plotted as a function of methane pressure, shown in Fig 4.5b. The calculated pressure broadening coefficient from this experiment is 0.0682 (3) $\text{cm}^{-1}/\text{atm}$, which agrees with the HITRAN reported value of 0.069 $\text{cm}^{-1}/\text{atm}$.(Gordon et al., 2017)

$^{12}\text{CH}_2\text{D}_2$ Measurement

To test the precision of the instrument, number density of methane isotopologues were monitored in a natural abundance methane sample with a pressure of 5.1 Torr. This pressure is chosen to obtain high enough $^{12}\text{CH}_2\text{D}_2$ absorption without pressure over broadening the targeted spectral line until mixing with other nearby transitions. The ratio between $^{12}\text{CH}_3\text{D}$ and the rarely

abundant $^{12}\text{CH}_2\text{D}_2$ was monitored 7 times by measuring the $^{12}\text{CH}_3\text{D}$ doublet at 2268.1 cm^{-1} and $^{12}\text{CH}_2\text{D}_2$ line at 2268.02 cm^{-1} back and forth over 4 hours. The $^{12}\text{CH}_2\text{D}_2$ transition used for these measurements is the only line isolated from interference by other more abundant isotopologues. However, interference from strong carbon dioxide transitions at 2267.997 cm^{-1} ($^{13}\text{C}^{16}\text{O}_2$) and 2268.003 cm^{-1} ($^{12}\text{C}^{16}\text{O}_2$) can become significant with a small impurity in the sample or minor cavity leak. Thus, the FS-CRDS cavity was designed to have very low leak rates. Methane sample was not treated prior to introduction to the analysis cavity cell. Since the $^{12}\text{CH}_2\text{D}_2$ transition was not assigned and no line parameters were reported for it, temperature dependence of this line is not known. Thus, it is crucial to use a $^{12}\text{CH}_3\text{D}$ line close to the targeted $^{12}\text{CH}_2\text{D}_2$ line and with small temperature dependence, which translates to a low ground state energy. The targeted $^{12}\text{CH}_3\text{D}$ transition used is the doublet centered at 2268.107 cm^{-1} and 2268.114 cm^{-1} , which both have ground state energy of $E'' = 58.8831\text{ cm}^{-1}$. Figure 4.6 shows sample spectra of one pair of the measurement. The ratio of $^{12}\text{CH}_2\text{D}_2/^{12}\text{CH}_3\text{D}$ can be expressed as:

$$R = \frac{[^{12}\text{CH}_2\text{D}_2]}{[^{12}\text{CH}_3\text{D}]} = \frac{S_{^{12}\text{CH}_3\text{D}} A_{^{12}\text{CH}_2\text{D}_2}}{S_{^{12}\text{CH}_2\text{D}_2} A_{^{12}\text{CH}_3\text{D}}} \quad (\text{Eq. 4. 5})$$

where A_x is the integrated area of each absorption line, while S_x is the line strength of that absorber. Since the line strength is not known for $^{12}\text{CH}_2\text{D}_2$, only the ratio between the areas of each pair of these two isotopologues can be reported. However, only deviation from a known standard ($R_{\text{sample}}/R_{\text{standard}}$) is needed for isotope composition measurements. Thus, we will demonstrate the performance of our doubly substituted methane FS-CRDS spectrometer in terms of the precision of $^{12}\text{CH}_2\text{D}_2$ number density and $^{12}\text{CH}_2\text{D}_2/^{12}\text{CH}_3\text{D}$ measurement.

Each $^{12}\text{CH}_2\text{D}_2$ line is fitted with a Galatry profile to integrate area underneath the line.

As shown in Fig 4.6, the signal to noise ratio (SNR), defined as the ratio between the peak signal

to the RMS noise of the residual, of each measurement is $\sim 85:1$. The standard error of these 7 measurements is $\sim 1.5\%$ for each $^{12}\text{CH}_2\text{D}_2$ number density measurement. On the other hand, each $^{12}\text{CH}_3\text{D}$ spectrum is fitted as a linear combination of two Galatry line profiles to integrate the area under both lines simultaneously. Since the $^{12}\text{CH}_3\text{D}$ is much stronger in a natural abundance sample measurement, the SNR of each $^{12}\text{CH}_3\text{D}$ spectral fit is approximately 300:1. The overall statistics of the seven $^{12}\text{CH}_3\text{D}$ number density measurements yielded a standard error of 1.09%. When taken ratio of the area of $^{12}\text{CH}_2\text{D}_2$ and $^{12}\text{CH}_3\text{D}$ (measured ~ 20 minutes from each other) within each measurement pair, the standard error in the area ratio measurement is reported to be 1.38%.

CONCLUSION

In this work, we demonstrated a prototype optical analyzer to measure clumped isotope abundance of methane. We demonstrate high sensitivity measurements of $^{12}\text{CH}_2\text{D}_2$ isotopologues using a high precision and high resolution spectroscopy technique, frequency stabilized cavity ring-down spectroscopy (FS-CRDS). The frequency range of the spectrometer is 2200 cm^{-1} to 2300 cm^{-1} , which provides capability to detect the five highest abundant methane isotopologues. The cavity ring-down method uses two highly reflective mirrors to increase the effective pathlength of laser light up to 5km inside the optical cavity, increasing the sensitivity significantly from traditional absorption techniques. The physical length of the cavity is actively stabilized with respect to a frequency stabilized He/Ne laser, which improves the sensitivity and precision of the spectrometer. This technique can be used as a potential complement to IRMS measurements for its ability to measure abundances of rare methane isotopologues with a short

time average. This instrument demonstrated a precision of $\sim 1.38 \text{ ‰}$ for the ratio measurement of $^{12}\text{CH}_2\text{D}_2/^{12}\text{CH}_3\text{D}$ with ~ 4 hours of averaging.

ACKNOWLEDGEMENTS

We would like to thank Keeyoon Sung and Linda Brown from the Jet Propulsion Laboratory who provided us the FTIR spectra of $^{13}\text{CH}_3\text{D}$ and $^{12}\text{CH}_2\text{D}_2$. We would also like the help of Carl Blumenfeld for his help on the synthesis of $^{13}\text{CH}_3\text{D}$. L. S. and T. Q. B were supported by NASA's Earth and Space Science Fellowships and the NASA Mars Fundamental Research Grant NNX12AI01G.

REFERENCE

- Bernard, B.B., Brooks, J.M. and Sackett, W.M. (1976) Natural gas seepage in the Gulf of Mexico. *Earth and Planetary Science Letters* 31, 48-54.
- Black, E.D. (2001) An introduction to Pound–Drever–Hall laser frequency stabilization. *American Journal of Physics* 69, 79-87.
- Bui, T.Q., Long, D.A., Cygan, A., Sironneau, V.T., Hogan, D.W., Rupasinghe, P.M., Ciurylo, R., Lisak, D. and Okumura, M. (2014) Observations of Dicke narrowing and speed dependence in air-broadened CO₂ lineshapes near 2.06 μm . *J. Chem. Phys.* 141, 10.
- Butler, J.H. and Montzka, S.A. (2017) The NOAA Annual Greenhouse Gas Index (AGGI).
- Claypool, G.E. and Kvenvolden, K.A. (1983) METHANE AND OTHER HYDROCARBON GASES IN MARINE SEDIMENT. *Annu. Rev. Earth Planet. Sci.* 11, 299-327.

Dicke, R.H. (1953) The Effect of Collisions upon the Doppler Width of Spectral Lines. *Physical Review* 89, 472-473.

Dlugokencky, E.J., Nisbet, E.G., Fisher, R. and Lowry, D. (2011) Global atmospheric methane: budget, changes and dangers. *Philosophical Transactions of the Royal Society A: Mathematical, Physical and Engineering Sciences* 369, 2058-2072.

Douglas, P.M.J., Stolper, D.A., Smith, D.A., Anthony, K.M.W., Paull, C.K., Dallimore, S., Wik, M., Crill, P.M., Winterdahl, M., Eiler, J.M. and Sessions, A.L. (2016) Diverse origins of Arctic and Subarctic methane point source emissions identified with multiply-substituted isotopologues. *Geochim. Cosmochim. Acta* 188, 163-188.

Eiler, J.M., Clog, M., Magyar, P., Piasecki, A., Sessions, A., Stolper, D., Deerberg, M., Schlueter, H.-J. and Schwieters, J. (2013a) *Int. J. Mass. Spectrom.* 335, 45-56.

Eiler, J.M., Clog, M., Magyar, P., Piasecki, A., Sessions, A., Stolper, D., Deerberg, M., Schlueter, H.-J. and Schwieters, J. (2013b) A high-resolution gas-source isotope ratio mass spectrometer. *International Journal of Mass Spectrometry* 335, 45-56.

Etioppe, G. and Lollar, B.S. (2013) ABIOTIC METHANE ON EARTH. *Rev. Geophys.* 51, 276-299.

Ferry, J.G. (1998) Enzymology of one-carbon metabolism in methanogenic pathways. *Microbiology Reviews* 23, 13-38.

Galatry, L. (1961) Simultaneous Effect of Doppler and Foreign Gas Broadening on Spectral Lines. *Physical Review* 122, 1218-1223.

Gordon, I.E., Rothman, L.S., Hill, C., Kochanov, R.V., Tan, Y., Bernath, P.F., Birk, M., Boudon, V., Campargue, A., Chance, K.V., Drouin, B.J., Flaud, J.M., Gamache, R.R., Hodges, J.T., Jacquemart, D., Perevalov, V.I., Perrin, A., Shine, K.P., Smith, M.A.H., Tennyson, J., Toon,

G.C., Tran, H., Tyuterev, V.G., Barbe, A., Császár, A.G., Devi, V.M., Furtenbacher, T., Harrison, J.J., Hartmann, J.M., Jolly, A., Johnson, T.J., Karman, T., Kleiner, I., Kyuberis, A.A., Loos, J., Lyulin, O.M., Massie, S.T., Mikhailenko, S.N., Moazzen-Ahmadi, N., Müller, H.S.P., Naumenko, O.V., Nikitin, A.V., Polyansky, O.L., Rey, M., Rotger, M., Sharpe, S.W., Sung, K., Starikova, E., Tashkun, S.A., Auwera, J.V., Wagner, G., Wilzewski, J., Wcisło, P., Yu, S. and Zak, E.J. (2017) The HITRAN2016 molecular spectroscopic database. *Journal of Quantitative Spectroscopy and Radiative Transfer*.

Hinrichs, K.-U., Hayes, J.M., Sylva, S.P., Brewer, P.G. and DeLong, E.F. (1999) Methane-consuming archaeobacteria in marine sediments. *Nature* 398, 802-805.

Hodges, J.T. and Ciuryło, R. (2005) Automated high-resolution frequency-stabilized cavity ring-down absorption spectrometer. *Rev. Sci. Instrum.* 76, 023112.

Hodges, J.T., Layer, H.P., Miller, W.W. and Scace, G.E. (2004) Frequency-stabilized single-mode cavity ring-down apparatus for high-resolution absorption spectroscopy. *Rev. Sci. Instrum.* 75, 849-863.

Hubbert, R.G. and Troup, G.J. (1977) Single-mode 3.39 μm laser study of methane absorption lineshape. *Physics Letters A* 61, 33-34.

Joelsson, L.M.T., Schmidt, J.A., Nilsson, E.J.K., Blunier, T., Griffith, D.W.T., Ono, S. and Johnson, M.S. (2016) Kinetic isotope effects of $(\text{CH}_3\text{D})\text{-C-12} + \text{OH}$ and $(\text{CH}_3\text{D})\text{-C-13} + \text{OH}$ from 278 to 313 K. *Atmos. Chem. Phys.* 16, 4439-4449.

Lisak, D., Hodges, J.T. and Ciuryło, R. (2006) Comparison of semiclassical line-shape models to rovibrational H_2O spectra measured by frequency-stabilized cavity ring-down spectroscopy. *Phys. Rev. A* 73, 012507.

Lisak, D., Masłowski, P., Cygan, A., Bielska, K., Wójtewicz, S., Piwiński, M., Hodges, J.T., Trawiński, R.S. and Ciuryło, R. (2010) Line shapes and intensities of self-broadened σ_{O_2} band transitions measured by cavity ring-down spectroscopy. *Physical Review A* 81, 042504.

Long, D.A., Bielska, K., Lisak, D., Havey, D.K., Okumura, M., Miller, C.E. and Hodges, J.T. (2011a) The air-broadened, near-infrared CO₂ line shape in the spectrally isolated regime: Evidence of simultaneous Dicke narrowing and speed dependence *J. Chem. Phys.* 135.

Long, D.A., Cygan, A., van Zee, R.D., Okumura, M., Miller, C.E., Lisak, D. and Hodges, J.T. (2012) Frequency-Stabilized Cavity Ringdown Spectroscopy. *Chem. Phys. Lett.* 536, 1-8.

Long, D.A., Okumura, M., Miller, C.E. and Hodges, J.T. (2011b) Frequency-stabilized cavity ring-down spectroscopy measurements of carbon dioxide isotopic ratios *Appl. Phys. B* 105, 471-477.

McCollom, T.M. (2013) Laboratory Simulations of Abiotic Hydrocarbon Formation in Earth's Deep Subsurface. *Reviews in Mineralogy and Geochemistry* 75, 467-494.

Ono, S., Wang, D.T., Gruen, D.S., Lollar, B.S., Zahniser, M.S., McManus, B.J. and Nelson, D.D. (2014) Measurement of a Doubly Substituted Methane Isotopologue, (CH₃D)-C-13, by Tunable Infrared Laser Direct Absorption Spectroscopy. *Analytical Chemistry* 86, 6487-6494.

Paldus, B.A., Harb, C.C., Spence, T.G., Wilke, B., Xie, J., Harris, J.S. and Zare, R.N. (1998) Cavity-locked ring-down spectroscopy. *Journal of Applied Physics* 83, 3991-3997.

Ramaswamy, V., Boucher, O., Haigh, J., Hauglustine, D., Haywood, J., Myhre, G., Nakajima, T., Shi, G., Solomon, S. (2001) Radiative forcing of climate. *Climate Change*, 349-416.

Saunio, M., Jackson, R.B., Bousquet, P., Poulter, B. and Canadell, J.G. (2016) The growing role of methane in anthropogenic climate change. *Environmental Research Letters* 11, 120207.

Schoell, M. (1980) THE HYDROGEN AND CARBON ISOTOPIC COMPOSITION OF METHANE FROM NATURAL GASES OF VARIOUS ORIGINS. *Geochim. Cosmochim. Acta* 44, 649-661.

Schoell, M. (1983) GENETIC-CHARACTERIZATION OF NATURAL GASES. *AAPG Bull.-Am. Assoc. Petr. Geol.* 67, 2225-2238.

Stolper, D.A., Martini, A.M., Clog, M., Douglas, P.M., Shusta, S.S., Valentine, D.L., Sessions, A.L. and Eiler, J.M. (2015) Distinguishing and understanding thermogenic and biogenic sources of methane using multiply substituted isotopologues. *Geochim. Cosmochim. Acta* 161, 219-247.

Stolper, D.A., Sessions, A.L., Ferreira, A.A., Neto, E.V.S., Schimmelmann, A., Shusta, S.S., Valentine, D.L. and Eiler, J.M. (2014a) Combined C-13-D and D-D clumping in methane: Methods and preliminary results. *Geochim. Cosmochim. Acta* 126, 169-191.

Stolper, D.A., Sessions, A.L., Ferreira, A.A., Santos Neto, E.V., Schimmelmann, A., Shusta, S.S., Valentine, D.L. and Eiler, J.M. (2014b) Combined ¹³C–D and D–D clumping in methane: Methods and preliminary results. *Geochim. Cosmochim. Acta* 126, 169-191.

Tauer, R.K. (1998) Biochemistry of methanogenesis: a tribute to Marjory Stephenson:1998 Marjory Stephenson Prize Lecture. *Microbiology* 144, 2377-2406.

Whitehill, A.R., Joelsson, L.M.T., Schmidt, J.A., Wang, D.T., Johnson, M.S. and Ono, S. (2017) Clumped isotope effects during OH and Cl oxidation of methane. *Geochim. Cosmochim. Acta* 196, 307-325.

Whiticar, M.J. (1999) Carbon and hydrogen isotope systematics of bacterial formation and oxidation of methane. *Chem. Geol.* 161, 291-314.

Wuebbles, D.J., Hayhoe, K. (2002) Atmospheric methane and global change. *EarthScience Reviews* 57, 177-210.

Yeung, L.Y., Young, E.D. and Schauble, E.A. (2012) Measurements of (OO)-O-18-O-18 and (OO)-O-17-O-18 in the atmosphere and the role of isotope-exchange reactions. *Journal of Geophysical Research-Atmospheres* 117.

Young, E.D., Kohl, I.E., Lollar, B.S., Etiope, G., Rumble, D., Li, S., Haghnegahdar, M.A., Schauble, E.A., McCain, K.A., Foustoukos, D.I., Sutcliffe, C., Warr, O., Ballentine, C.J., Onstott, T.C., Hosgormez, H., Neubeck, A., Marques, J.M., Perez-Rodriguez, I., Rowe, A.R., LaRowe, D.E., Magnabosco, C., Yeung, L.Y., Ash, J.L. and Bryndzia, L.T. (2017) The relative abundances of resolved (CH₂D₂)-C-12 and (CH₃D)-C-13 and mechanisms controlling isotopic bond ordering in abiotic and biotic methane gases. *Geochim. Cosmochim. Acta* 203, 235-264.

Young, E.D., Rumble, D., Freedman, P. and Mills, M. (2016) A large-radius high-mass-resolution multiple-collector isotope ratio mass spectrometer for analysis of rare isotopologues of O-2, N-2, CH₄ and other gases. *International Journal of Mass Spectrometry* 401, 1-10.

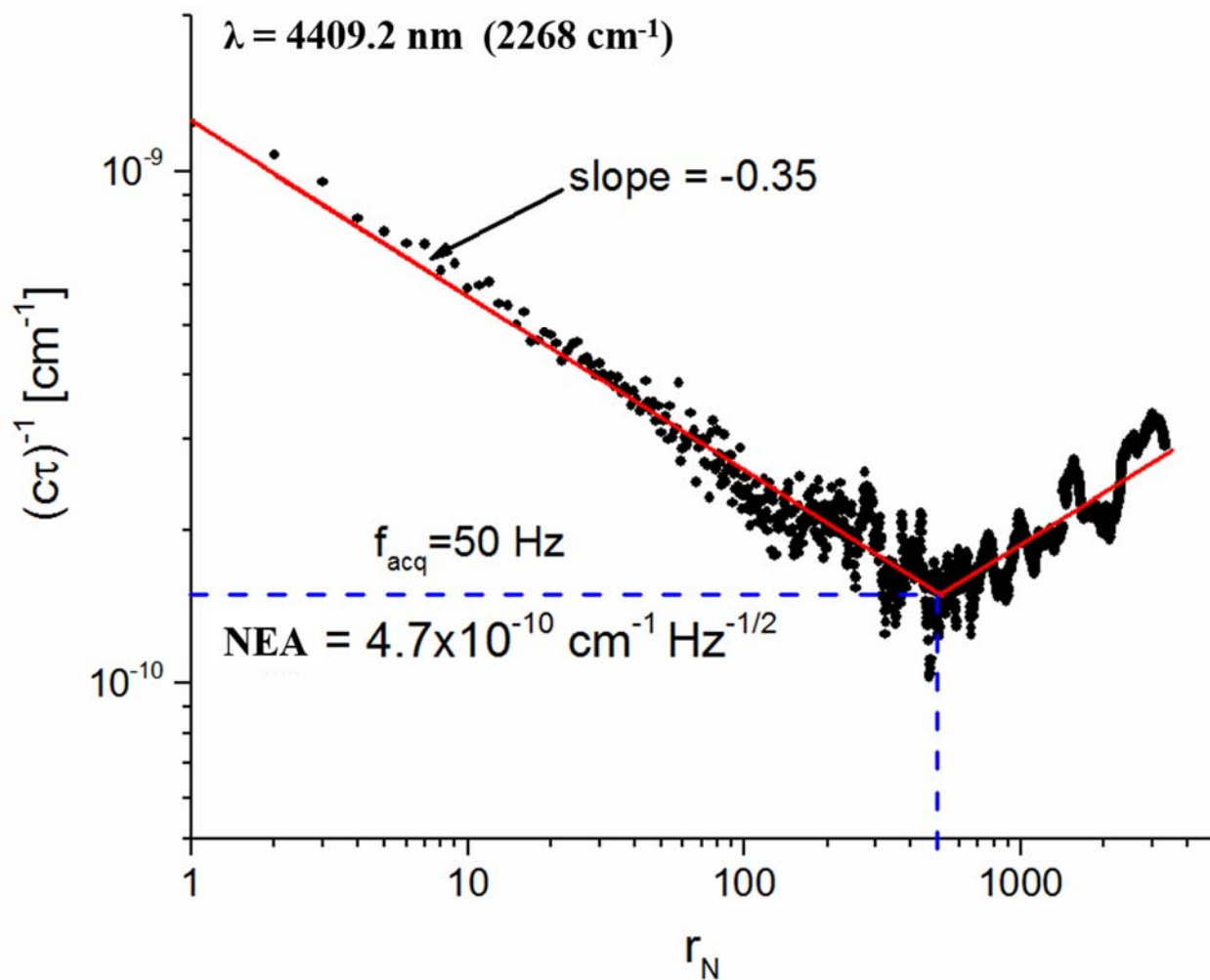


Figure 4.2. Allan deviation plot for the ringdown decays of vacuum baseline losses at 2268.00 cm^{-1} . The acquisition rate is $\sim 50 \text{ Hz}$ with the estimated minimum detectable absorbance of the spectrometer as $1.49 \times 10^{-10} \text{ cm}^{-1}$.

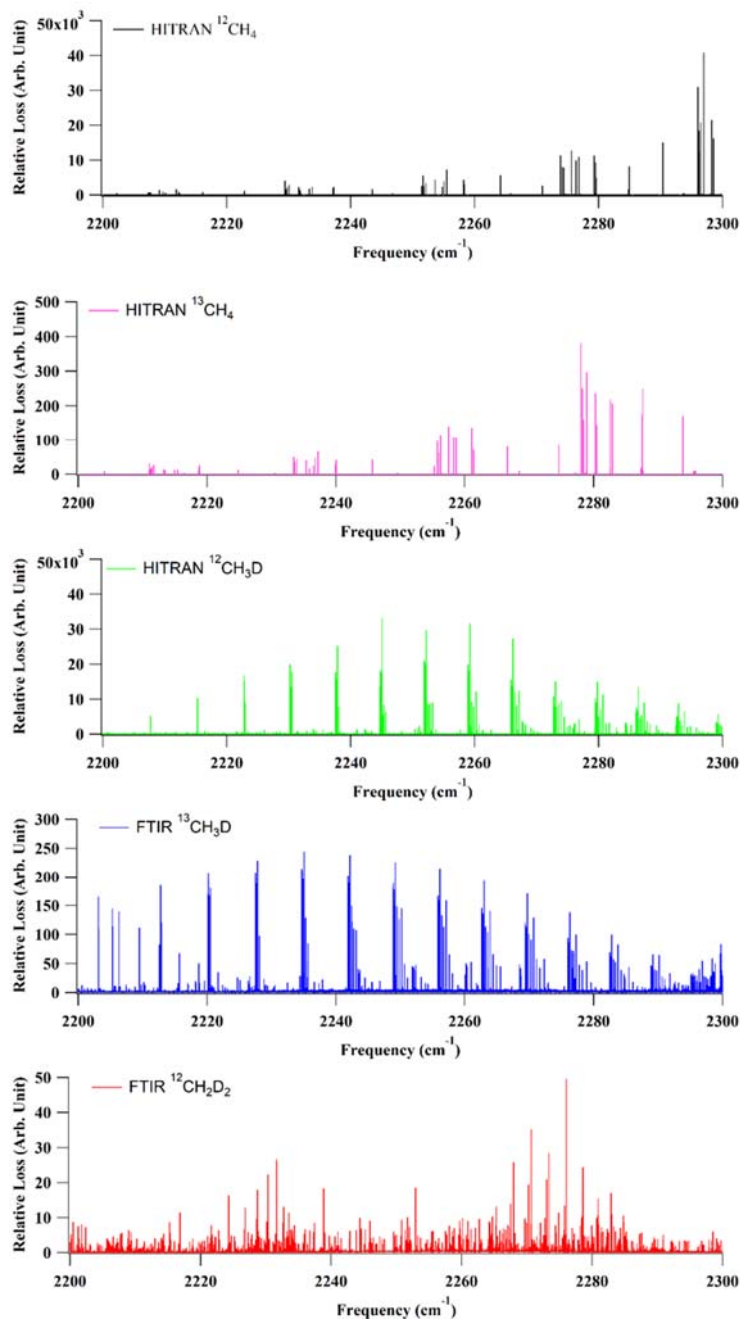


Figure 4. 3. Absorption line positions and relative strength for five of the major isotopologues of methane within the tuning range of the EC-QCL laser used for our spectrometer. Spectra of the first 3 isotopologues were generated based on the line parameters reported in the HITRAN database. Spectra of the two doubly substituted methane isotopologues were from normalized high resolution FTIR measurements of pure $^{13}\text{CH}_3\text{D}$ and $^{12}\text{CH}_2\text{D}_2$.

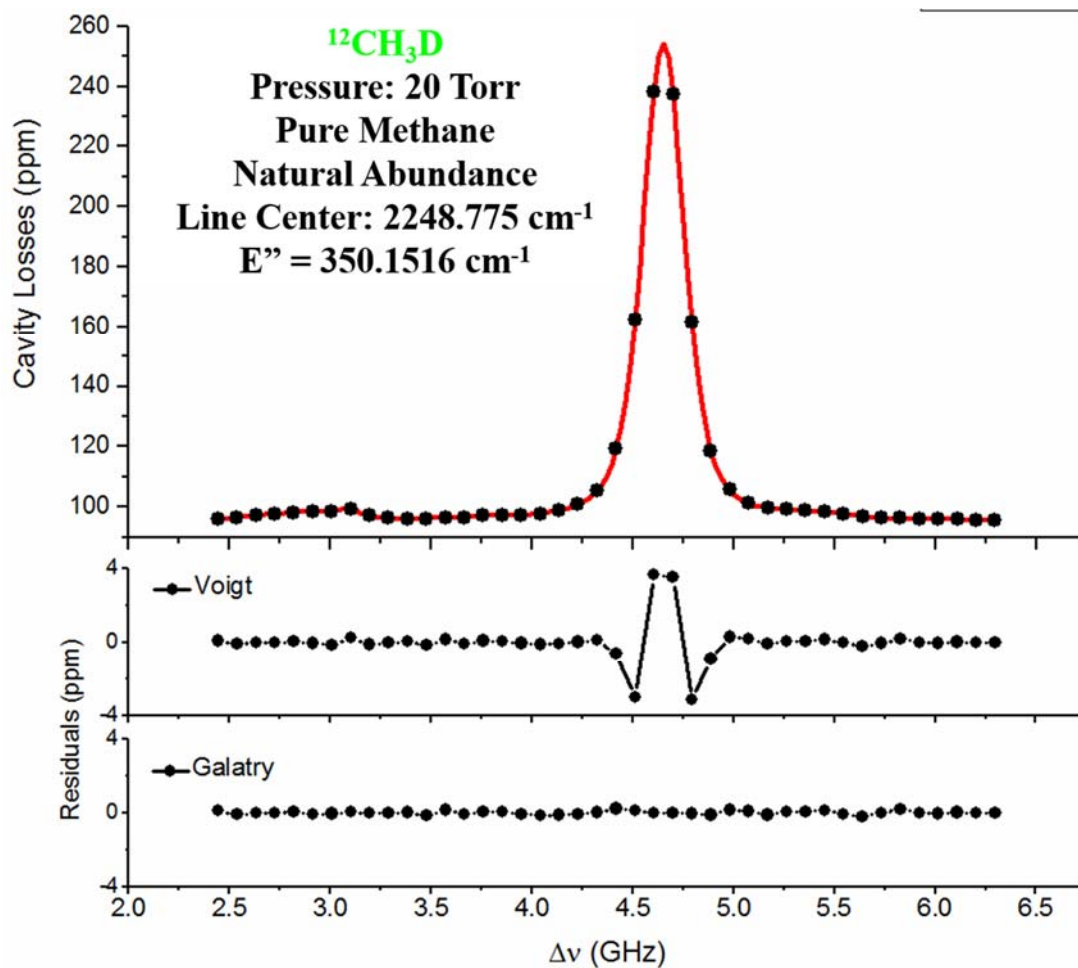


Figure 4.4. Comparison of the Voigt profile versus Galatry profile model for the $^{12}\text{CH}_3\text{D}$ spectrum at 2248.75 cm^{-1} from measurement of a 20 Torr natural abundance methane sample. In the upper panel, the measured data are shown in the black dots, while the red solid line is the galatry profile fit. The middle and bottom panels are the residuals for these two profile fits.

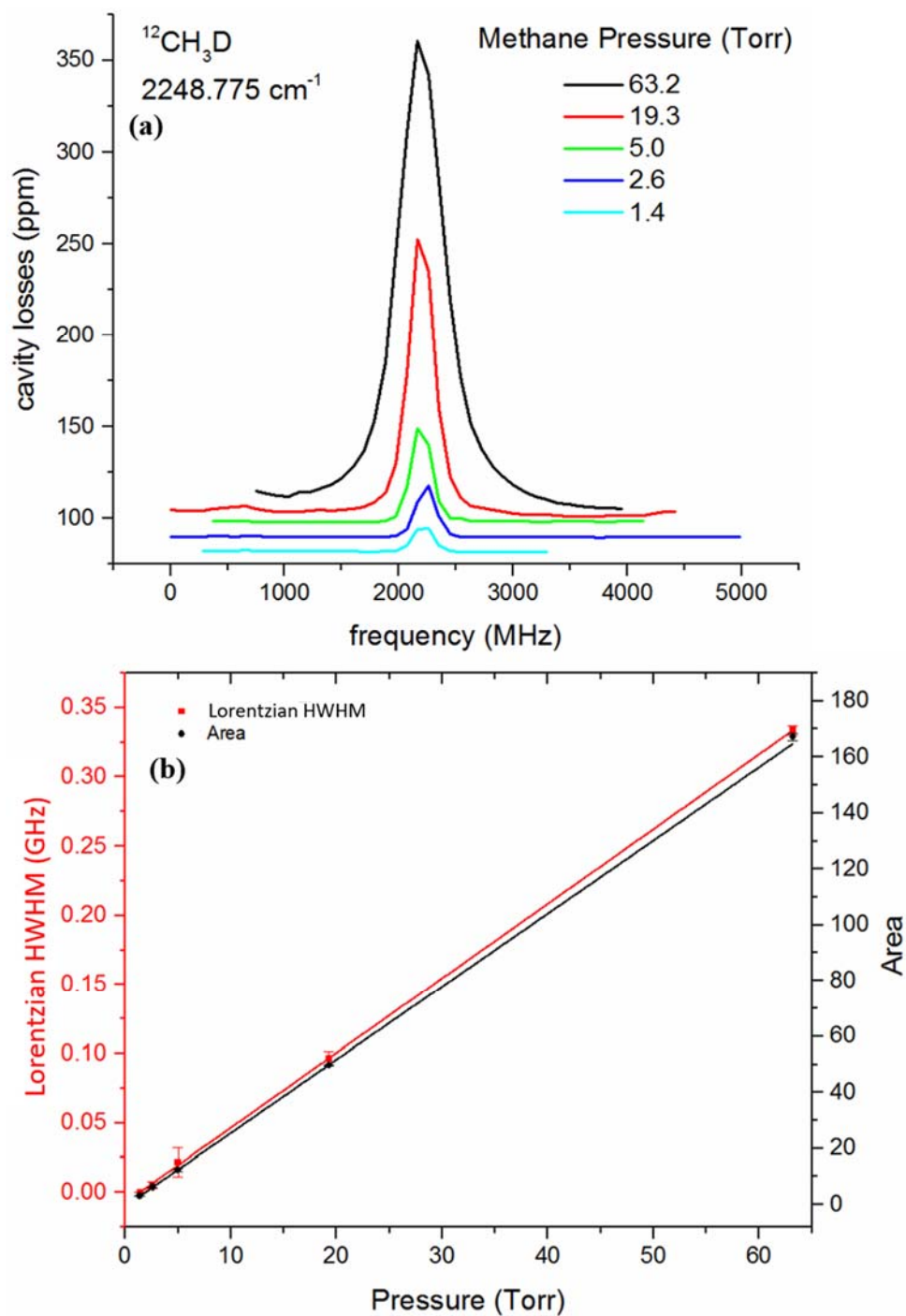


Figure 4. 5. Lineshape study of the $^{12}\text{CH}_3\text{D}$ line centered at 2248.775 cm^{-1} . (a) Spectra of the $^{12}\text{CH}_3\text{D}$ transition measured at pressures between 1.4 Torr and 63.2 Torr. (b) Spectral fit results, Lorentzian width (HWHM) and integrated area, plotted as a function of the total methane pressure.

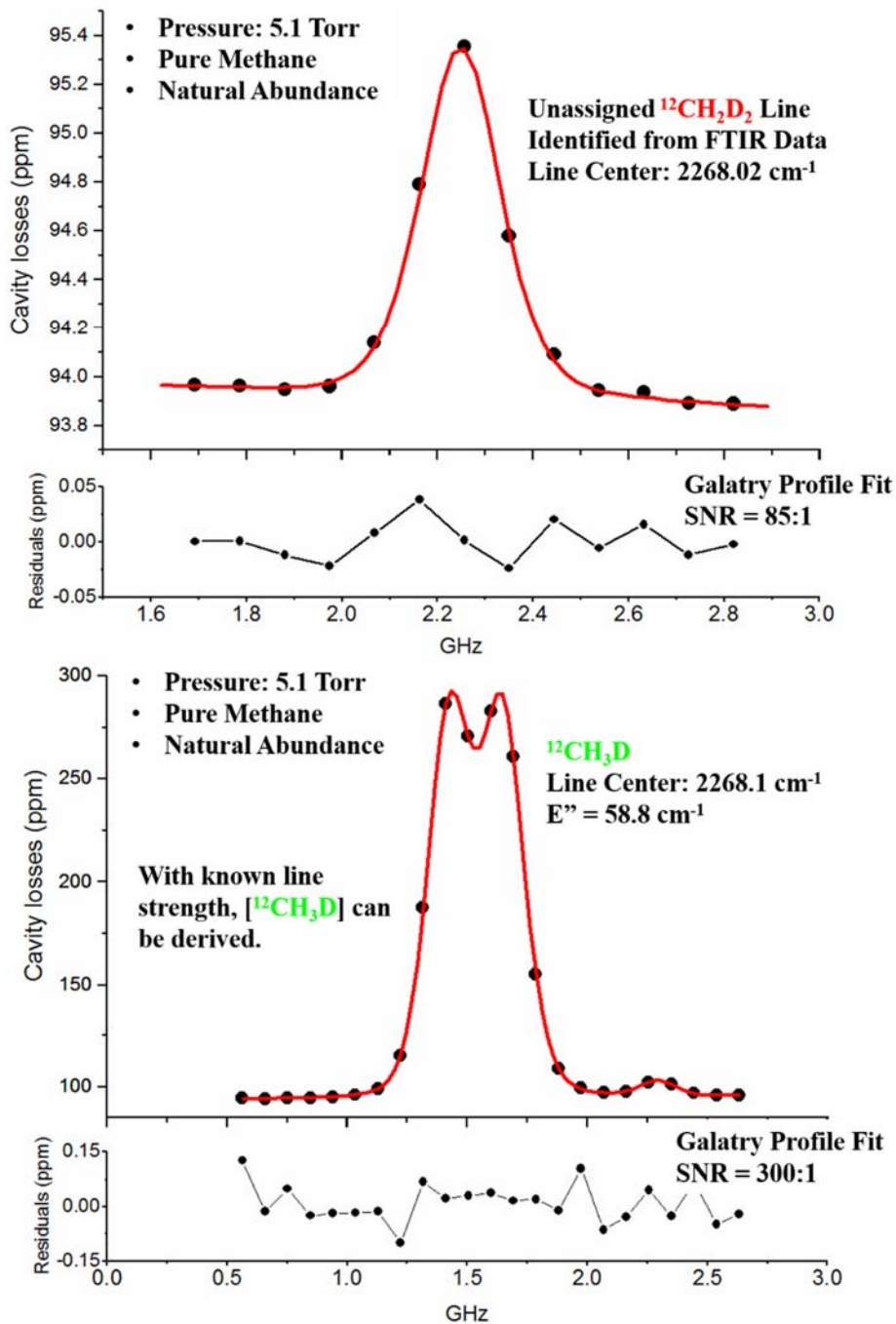


Figure 4. 6. Sample spectra of a pair of the $^{12}\text{CH}_2\text{D}_2$ and $^{12}\text{CH}_3\text{D}$ abundance measurement of a 5.1 Torr natural abundance methane measurement. The black dots in each spectrum was the measured data and the red solid line is the fitted model. Both spectra were fitted to Galatry profiles with residuals shown in the figures.

SUPPORTING MATERIAL

Isotope Terminology Notation

Isotopologue composition of particular minor isotopologue ($^{13}\text{CH}_4$, $^{12}\text{CH}_3\text{D}$, $^{13}\text{CH}_3\text{D}$, and $^{12}\text{CH}_2\text{D}_2$) are normally expressed as its ratio against the major isotopologue $^{12}\text{CH}_4$. Such as:

$$R^{13}\text{CH}_4 = \frac{[^{13}\text{CH}_4]}{[^{12}\text{CH}_4]} \quad (\text{Eq. S4. 1})$$

$$R^{12}\text{CH}_3\text{D} = \frac{[^{12}\text{CH}_3\text{D}]}{[^{12}\text{CH}_4]} \quad (\text{Eq. S4. 2})$$

Isotopologue ratios are normally measured relative to a known standard:

$$\delta^{13}\text{CH}_4 = \left(\frac{^{13}R_{\text{sample}}}{^{13}R_{\text{standard}}} - 1 \right) \times 1000 \text{‰} \quad (\text{Eq. S4. 3})$$

At natural isotopic abundances, isotopologue ratios of the singly substituted methane are approximately equal to the bulk isotope ratios

$$^{13}R = \frac{^{13}\text{C}}{^{12}\text{C}} \approx R^{13}\text{CH}_4 \quad (\text{Eq. S4. 4})$$

$$^{\text{D}}R = \frac{\text{D}}{\text{H}} \approx R^{12}\text{CH}_3\text{D} \quad (\text{Eq. S4. 5})$$

The international standard used for carbon is the Vienna Pee Dee Belemnite standard (VPDB); and the standard used for hydrogen is the Vienna Standard Mean Ocean Water standard (VSMOW).

Grignard Synthesis Protocol for $^{13}\text{CH}_3\text{D}$

In order to verify $^{13}\text{CH}_3\text{D}$ lines reported from the high resolution FTIR measurement, a pure $^{13}\text{CH}_3\text{D}$ sample was diluted in nitrogen. However, pure $^{13}\text{CH}_3\text{D}$ is not commercially available. Thus, we used a known Grignard process to synthesize and trapped a sample of $^{13}\text{CH}_3\text{D}$. Synthesis procedure is shown as below:

1. Weight out 0.5 g Mg. Check that Mg still shines (not oxidized).
2. Add a stir bar and Mg to a three-neck flask. From one neck, have a helium inlet and evacuation path (and a valve between these). On the middle neck, have a condenser attached to a water/ether trap, methane trap (with bypass), and bubbler. On the third neck, have a septum.
3. Flame dry the apparatus with switch to vacuum. Close before the bubbler.
4. Run between He flow and vacuum for three cycles, then leave on He flow. Whenever on He flow, open to bubbler. Keep at a slow flow (1 bubble every few seconds)
5. Extract 9mL of anhydrous ether. Before extraction insert a balloon of Ar on a syringe into the vial. This will ensure that the volume of ether extracted is replaced with Ar.
6. Inject the ether into the flask.
7. Turn on the stirrer.
8. In a syringe, measure 0.9 mL methyl iodide. Inject dropwise into the Grignard.
9. Wait for Grignard to form. Solution will first become cloudy, then dark and clear.
10. Open to methane trap. Add liquid nitrogen and pentane to the ether trap and liquid nitrogen to the methane trap.
11. Add 0.7 mL water to the flask.

12. Wait for reaction to finish (you should be able to see the progress on the bubbler—as it proceeds, more gas is formed and bubbles out), then open bypass valve and close methane trap.
13. Quench reaction with DI water.
14. Put methane trap on a vacuum line with an ether trap (keep methane trap in liquid nitrogen).
15. Evacuate.
16. Once line is evacuated, open methane trap and evacuate any He in the trap.
17. Close line to vacuum take liquid nitrogen off methane (have a pressure reader in line!).
18. Warm methane trap with a flame for 5-10 minute.
19. Add pentane and dry ice to the ether trap. Wait for 3 minutes or form pressure to stabilize.
20. Add liquid nitrogen to the methane trap.
21. Wait for pressure to stabilize.
22. Close trap.

Figures and Tables

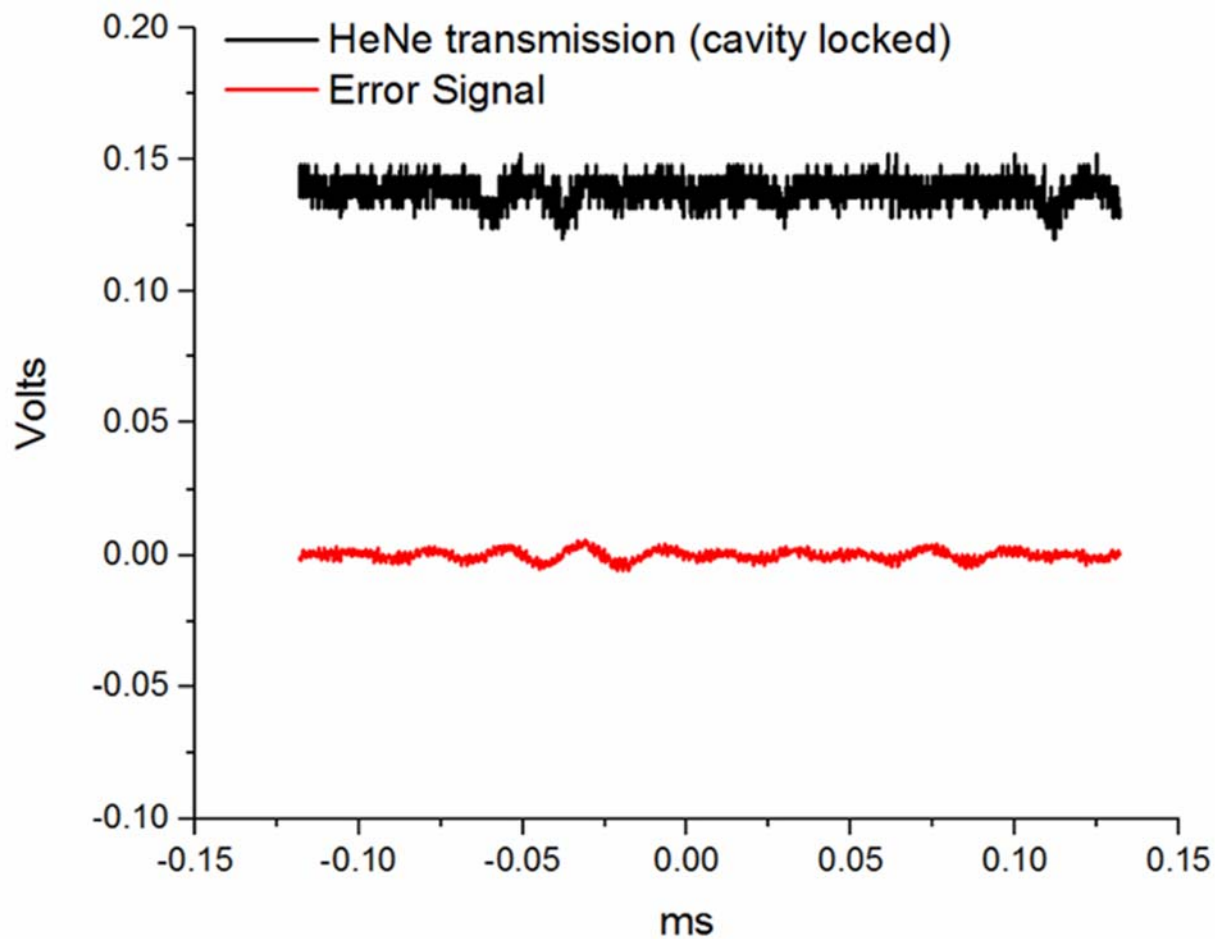


Figure S4. 1. Performance of the PDH locked cavity. The black trace is shows the HeNe transmission signal detected on the avalanche detector. The red trace shows the error signal produced from the lock-in amplifier

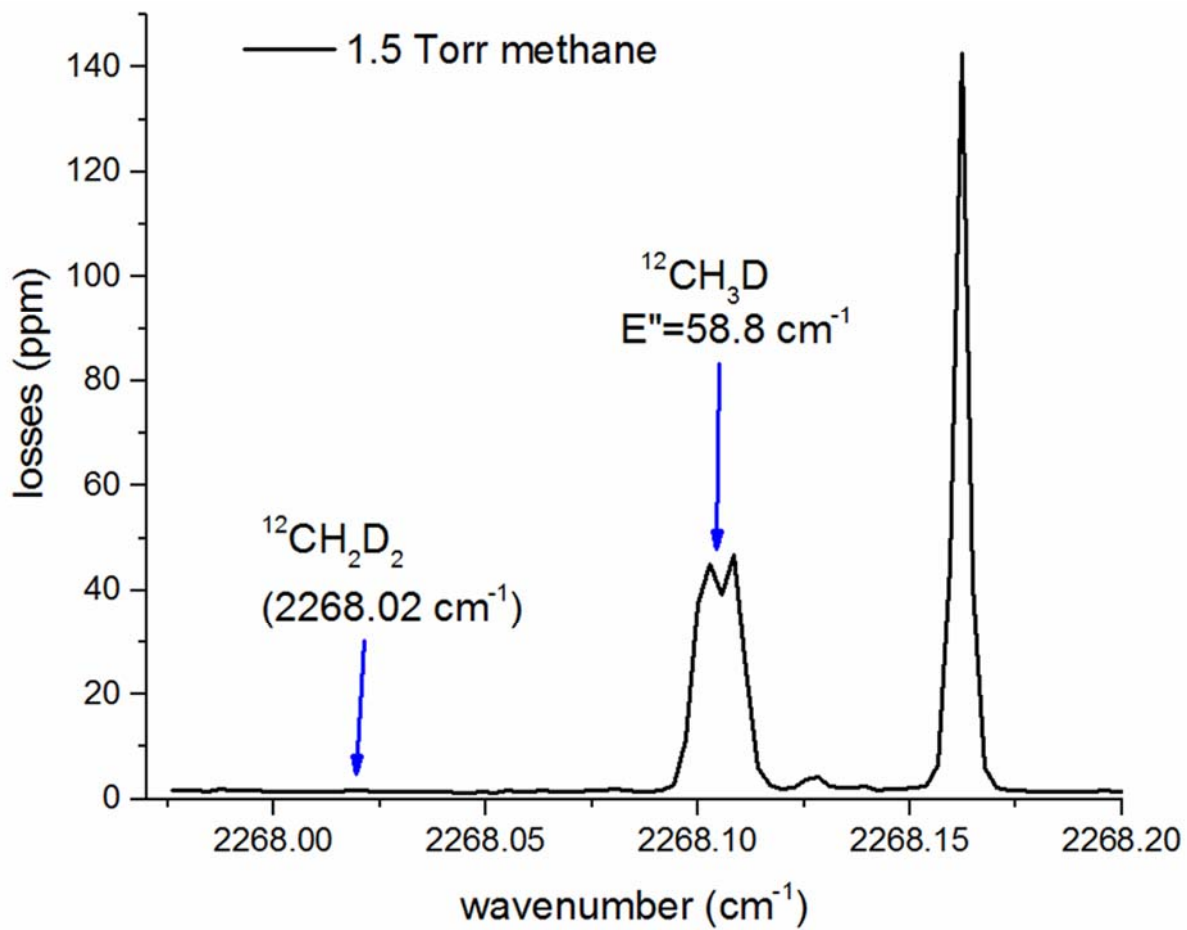


Figure S4. 2. Broadband measurement of a 1.5 Torr methane sample between 2267.925 cm^{-1} and 2268.20 cm^{-1} showing the line position and relative strength difference of the lines used for $^{12}\text{CH}_2\text{D}_2/^{12}\text{CH}_3\text{D}$ measurement.

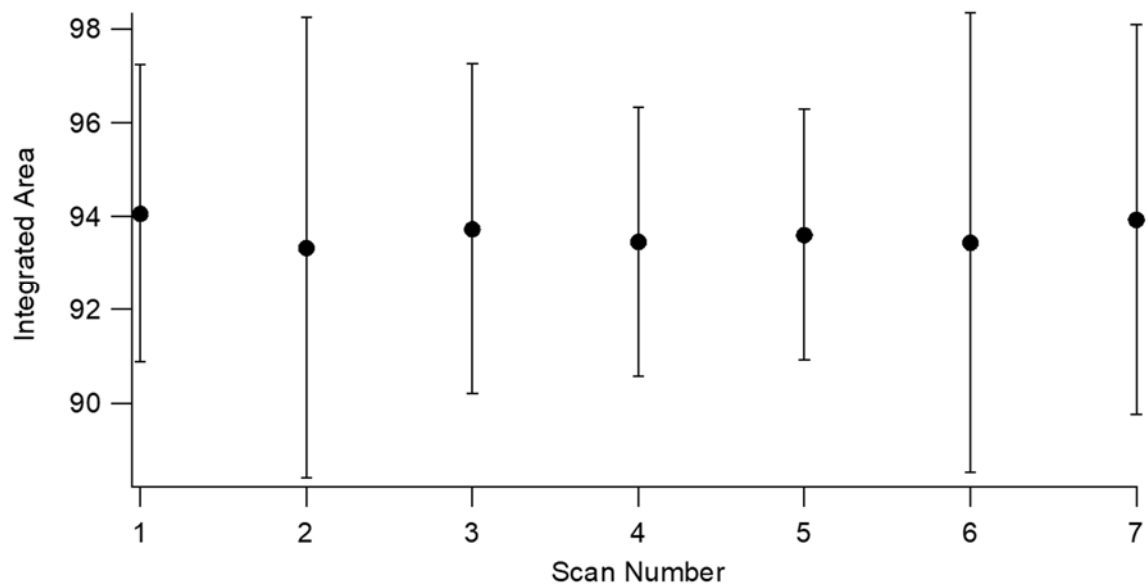


Figure S4. 3. Fitted area of the 7 $^{12}\text{CH}_3\text{D}$ lines. Error bars shown in this figure came from the reported error in the fit results.

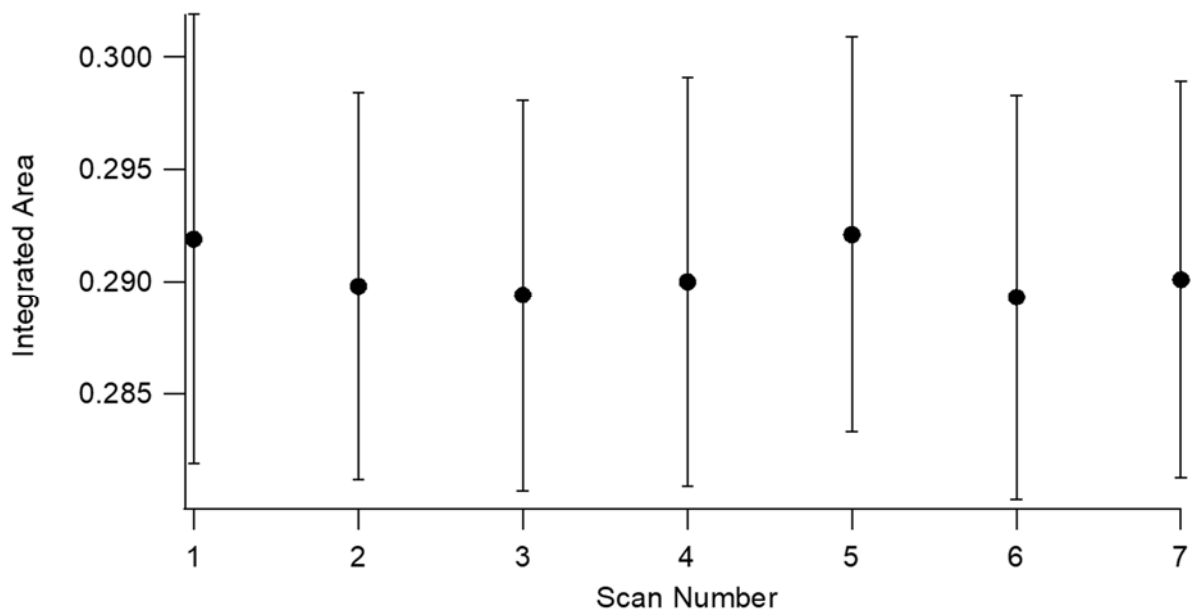


Figure S4. 4. Fitted area of the 7 $^{12}\text{CH}_2\text{D}_2$ lines. Error bars shown in this figure came from the reported error in the fit results.

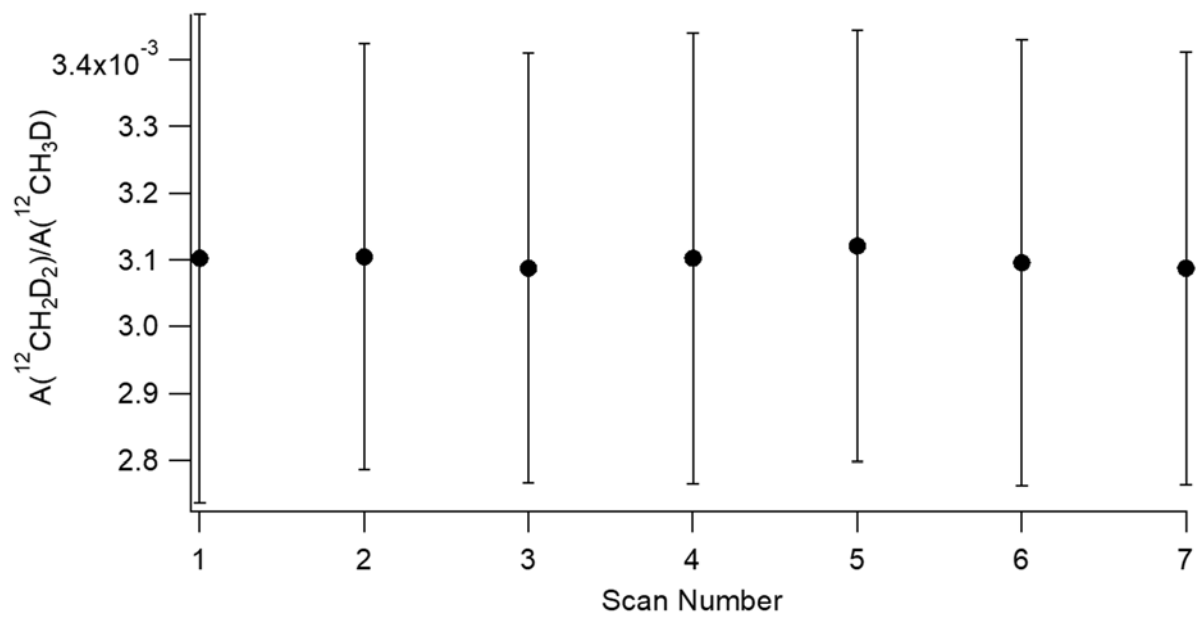


Figure S4. 5. Ratio of the 7 $^{12}\text{CH}_2\text{D}_2/^{12}\text{CH}_3\text{D}$ measurements.

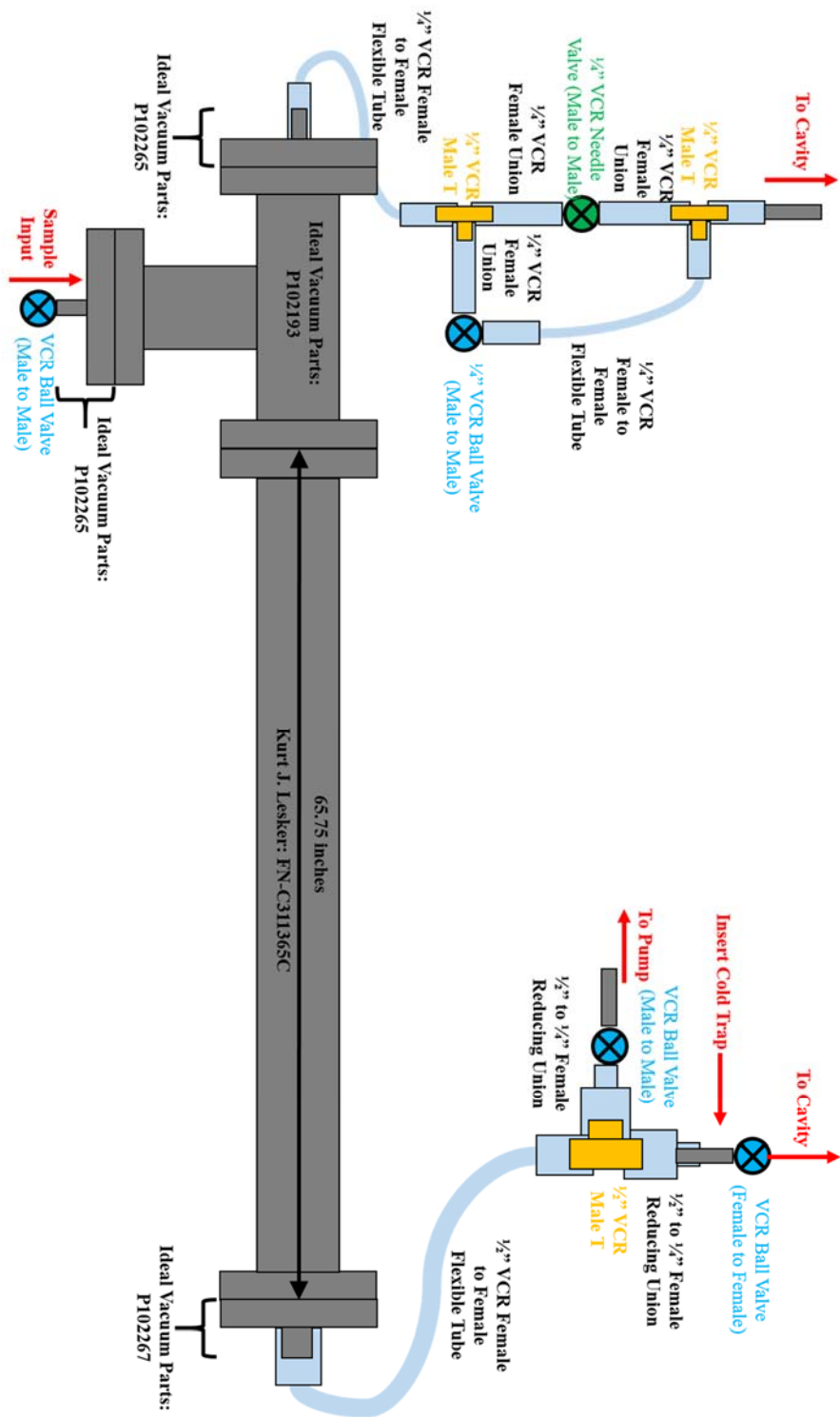


Figure S4. 6. Schematic of the sample inlet design configuration.

Chapter 5: Infrared Kinetic Spectroscopy Studies on HO₂ Radicals

Produced from Criegee Intermediate (CH₂OO)

ABSTRACT

In this laboratory study, we utilized our IR kinetic spectroscopy (IRKS) apparatus to study the formation of HCO radicals from the smallest Criegee Intermediate (CH_2OO), which was generated by photolyzing a mixture of $\text{CH}_2\text{I}_2/\text{O}_2/\text{N}_2$. HCO formation was observed in the form of HO_2 in the presence of O_2 . Since IO is a significant co-product from this photochemical system, and a good HO_2 remover, the study of IO kinetics is also needed. With the IRKS apparatus, we measured the concentrations of HO_2 and IO simultaneously. The time-dependent HO_2 concentration was measured with a frequency modulated diode laser, while the IO kinetics were monitored with an LED lamp. In order to constrain this complicated photochemical system, especially the iodine and peroxy radical chemistry, experiments were first carried out in the presence of a known Criegee Intermediate scavenger, hexafluoroacetone (HFA). Since the reaction rate constant between stabilized CH_2OO and HFA is known, a large amount of HFA molecules were added into the system to limit CH_2OO lifetime to less than 5 μs . Results from the high HFA experiments yield reaction rate constants for HO_2 formation without stabilized CH_2OO , and the branching ratio of CH_2IOO formation from $\text{CH}_2\text{I} + \text{O}_2$. Results from the high HFA experiments were then used to describe HO_2 and IO kinetics observed without HFA, thus with the presence of CH_2OO . Pressure and temperature dependences of the HO_2 and IO kinetics were studied. The typical rate of HCO formation from CH_2OO was estimated to be $\sim 800 \text{ s}^{-1}$.

INTRODUCTION

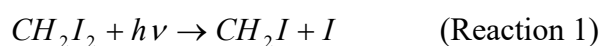
The ozonolysis reactions of alkenes are thought to proceed *via* the formation of energy rich 5-member-ring intermediate (primary ozonide, POZ), which are formed by initial addition of O₃ across the C=C unsaturated bond. In the gas phase, the highly energized POZs undergo direct decomposition into a Criegee intermediate (CI) and a carbonyl product (shown in Fig. 5.1). CIs are proposed to undergo (1) collisional stabilization, (2) isomerization to a “hot” hydroperoxide followed by breakage of the O-OH bond to form an OH radical plus a substituted alkyl radical (the “hydroperoxide channel”), (3) rearrangement to a “hot” ester with subsequent decomposition (the “ester channel”), or (4) elimination of an O (³P) atom. (Fenske et al., 2000; Kroll et al., 2001a; Kroll et al., 2001b)

CIs may play an important role in atmospheric chemistry through their reaction with other important atmospheric trace gases. Recent direct kinetic measurements have suggested that CI reactions with SO₂ and NO₂ are substantially faster than previously thought. Both of the reactions brought more attentions to CI in view of SOA formation and heterogeneous chemistry in the boundary layer. Recent work by Welz *et al.* using photoionization mass spectrometry was the first to observe the Criegee intermediate directly. In this work, a rate constant of $3.9 \times 10^{-11} \text{ cm}^3 \text{ molecule}^{-1} \text{ s}^{-1}$ was obtained for the reaction between SO₂ and CI at 4 torr, which is 100 times higher than previous experimental observation by Hatakeyama *et al.*, and 10 times lower than the calculated result by Kurten *et al.* (Hatakeyama et al., 1986; Kurten et al., 2011; Welz et al., 2012)

On the other hand, OH formation has been observed in alkenes ozonolysis reactions. OH is the primary oxidant in the atmosphere, to a large extent controlling the oxidative capacity in the troposphere. Previous studies measured OH yield in the ozone and alkenes reactions. However, since the alkene ozonolysis reactions are largely exothermic, the mechanism is rather complex. Only until recently, direct

evidence that the OH is coming CI has been reported.(Fang et al., 2016; Kidwell et al., 2016; Liu et al., 2014a; Liu et al., 2014b) In terms of the ethylene and O₃ reaction, which generate the smallest CI, CH₂OO, studies have shown OH yields of 14 to 60 %.

Previous work by Liu et al. observed OH being formed in the system CH₂I + O₂ and proposed that OH is directly from CH₂OO. (Liu et al., 2014b) The CI producing process was adopted from previous work by Welz et al, in which CH₂OO was directly generated by reacting iodomethyl radicals with molecular oxygen.(Welz et al., 2012) CH₂OO production mechanism is indicated as:



Where *M* stands for reaction collision partners. While the ethylene and O₃ reaction forms energetic POZ and it is sufficiently exothermic to decompose into CH₂OO + CH₂O or OH + HCO + CH₂O, this reaction generates CH₂OO mostly thermoneutrally, which makes it possible to directly study the composition of thermalized CI.

Once formed, CH₂OO has a short lifetime due to either unimolecular reaction to decompose into OH and HCO or other bimolecular processes. The possible CH₂OO decay reactions include:





OH from this system has been detected and its kinetics has been studied using laser induced fluorescence (LIF). However, kinetic study of the fate of the other byproduct, HCO, is crucial to fully understand the unimolecular reaction of the CH₂OO decomposition. With the presence of oxygen, HCO is known to be rapidly converted into HO₂ radical. Thus, studying of HO₂ kinetics in this system can shine light in the unimolecular kinetics of CH₂OO. In this study, we utilize the infrared kinetic spectroscopy (IRKS) to simultaneously monitor HO₂ and IO to study the self-reaction kinetics of the smallest Criegee intermediate.

METHODS

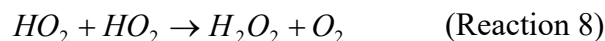
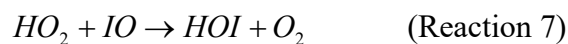
The infrared kinetic spectroscopy (IRKS) apparatus was used to measure the HO₂ and IO kinetics. Figure 5.2 shows a schematic of the IRKS instrument. The HO₂ self-reaction kinetics has been studied in order to test and optimize the performance of the apparatus. A mixture of radical precursors (Cl₂, C₂H₂, and O₂) and carrier gases (He and N₂) flows into the temperature controlled cell, and radical chemistry is initiated by pulsed laser photolysis of Cl₂ at 351nm to create Cl radicals. HO₂ radicals are created from Cl attacking C₂H₂ in the presence of O₂. The concentration of HO₂ radicals was monitored with two different optical methods simultaneously: UV absorption spectroscopy and frequency modulated (FM) near infrared (NIR) absorption spectroscopy. Light from a 150 W deuterium lamp (Hamamatsu L1314) enters the flow cell along the same pathway with the excimer light but in an opposite direction. After traveling through the whole flow cell once, a monochromator (Acton SpectraPro 300i) is coupled at the end of the D₂ lamp path to select the desired wavelength for HO₂ absorption, and a photomultiplier tube (PMT) was mounted at the end to measure the intensity of the selected wavelength.

The NIR probe light is introduced into the flow cell slightly off axis and passes through the cell 30 times in a Herriot resonance pattern and detected with an InGaAs photodiode detector.

The NIR probe was a 3mW distributed-feedback (DFB) continuous-wave tunable diode laser manufactured in the JPL Microdevices Laboratory. The NIR laser was frequency modulated at 6.8 MHz prior to entering the cell by varying the current with an external RF generator. Signal collected by the InGaAs detector was demodulated at 13.6 MHz and amplified by a factor of 1000. The monochromator was calibrated with the atomic emission lines from Hg (253.6 nm) and Cd (214.4, and 228.8 nm) pen lamps. For the HO₂ self-reaction measurements, the monochromator was set at 220 nm, measuring the absorbance mainly attributed by the A ← X transition of HO₂, and H₂O₂ molecule. At time zero (t = 0) (time zero was defined as when the excimer laser fires), high voltage and discharge from the lasing of the excimer laser caused a very negatively going signal lasting through the first 80 μs. According to kinetics model, at t = 0, HO₂ was generated instantaneously, and H₂O₂ was insignificant. Thus, it was assumed that absorption of the 220 nm light at t = 0 all came from the contribution of HO₂ absorption. Using Beer's Law, initial concentration of HO₂ could be calculated ([HO₂]₀). From previous studies, the path length of the UV probe was measured to be 150 cm.(Christensen et al., 2002; Noell et al., 2010) It was also assumed that at t = ∞, the only contribution to the absorbance was from H₂O₂. HO₂ concentration was monitored with the NIR probe by measuring the absorption at 6638.20 cm⁻¹, which is the ⁴Q₂ band head of the first overtone of the OH stretch.(Thiebaud et al., 2007) Because the FM modulation signal was not an absolute absorbance, the NIR signal was converted into concentration by calibration to the absolute concentration measured by the UV probe and calculating a voltage multiplier factor.

For the CH₂OO kinetics study, a mixture of CH₂I₂/O₂/N₂ was flown into the reaction cell. CH₂I₂ was introduced into the flow cell by flowing nitrogen carrying gas through a bubbler filled with the CH₂I₂ liquid, which was submerged in a 300 K water bath. A flip mirror was used to switch between the D₂ lamp and an air cooled LED (Thorlabs LED405E). The D₂ lamp was used to measure the concentration of the CH₂I₂ precursor at the beginning of each set of experiments at 240 nm. The LED was used to

measure the IO kinetics at 427.2 nm. The IO cross section reported from the JPL kinetic database is $2.05 \times 10^{-17} \text{ cm}^{-1}$.(Sander, 2011) The main HO₂ and IO reactions include:



For experiments to explore secondary chemistry without the presence of CH₂OO, hexafluoroacetone (HFA) was used to quickly remove CH₂OO from the system. Reaction rate constant between HFA and CH₂OO has been measured by Taatjes et al.(Welz et al., 2012)

RESULTS AND ANALYSIS

First, a time dependent signal with a lifetime of ~ 2 ms was observed with the NIR laser at 6638.20 cm^{-1} . Due to the spectral overlap between HO₂ and the CH₂I₂ precursor and other CH₂I₂ photolysis byproducts, the UV absorption could not be used to verify that this signal was indeed HO₂. Thus, we performed time dependent measurements with the NIR laser at other known transitions of HO₂ within the tunable range of the laser.(Parker et al., 2011) The results from these three frequencies are shown in Fig. 5.3. The kinetic traces measured at 6638.11 cm^{-1} and 6636.80 cm^{-1} show identical time dependence with the one observed at 6638.20 cm^{-1} . Relative amplitudes of signals at these two frequencies compare to at 6638.20 cm^{-1} agrees to the cross section differences reported in the literature. Thus, we could conclude that we have observed HO₂ from the CH₂I₂/O₂/N₂ photolysis system.

Second, it is important to confirm that the HO₂ signal observed is from reactions CH₂OO related. As shown by Wertz et al., HFA is a good CI scavenger. The typical HFA concentration we use for the CI scavenging experiments were $\sim 7 \times 10^{15}$ molecules/cm³, resulting in a CI lifetime of $\sim 4 \mu\text{s}$ once formed. Results of the HO₂ kinetics observed with or without HFA is shown in Fig. 5.4. It was found that most of the HO₂ was made from CI related reactions, while there is a prompt formation of HO₂ mechanism unrelated to CI. This could be attributed fast decomposition of the internally “hot” CH₂I₂OO to form HCO, OH, and I. This agrees well with the prompt OH formation observed from the LIF experiments.(Liu et al., 2014b)

We also monitored the IO kinetics simultaneously with HO₂ using the blue LED to provide complimentary understanding of the HO₂ kinetics. IO kinetics with or without HFA is shown in Fig. 5.5. IO was first thought to only form from reaction between CH₂I and O₂ (reaction R2a). However, photoionization mass spectrometry studies did not observe adequate amount of HCHO, which is a coproduct of this reaction channel.(Wertz et al., 2012) Thus, IO was made mainly from reaction between the collisionally quenched CH₂I₂OO radical and the photolysis product I. The rate of this reaction was estimated to be $\sim 4 \times 10^{-11}$.(Gravestock et al., 2010) The main IO removing reactions are the reaction with HO₂ to form HOI and O₂. Kinetics of this reaction has been well documented in the JPL kinetics database.(Sander, 2011) If IO formation was solely from CH₂I₂OO reactions, IO formation kinetics should not be affected when HFA was introduced to the system and IO decay rate should be slower due to the removal of HO₂. However, time dependent IO concentration measurements show a decrease of IO formation with HFA, indicating that some of the IO was from CH₂OO related reactions. Analogues to ozone, which is structurally and reactively similar to CH₂OO, we propose a reaction between CH₂OO and I to make IO and HCHO.

Pressure and temperature dependence of the HO₂ and IO kinetics with or without HFA was then studied to shine more light into the reaction mechanism of the CH₂OO related reactions. First, we investigated the temperature and pressure dependence of HO₂ (Fig. 5.6) and IO (Fig. 5.7) with the presence of HFA to isolate reactions prior to the formation of CH₂OO. Pressure dependence was studied between 10 Torr and 100 Torr. Total pressure was controlled by changing the partial pressure of N₂ in the flow cell, while keeping number densities of CH₂I₂, O₂, and HFA the same. Temperature dependence was carried out between 298.52 K and 324.48 K by flowing slightly heated water through the jacket of the flow cell. As we have observed that, neither the HO₂ nor IO experienced any temperature dependence. However, a positive pressure dependence of IO production was observed, while HO₂ kinetics remained unrelated to the pressure. This indicates a negative pressure dependence for CH₂OO production, since the overall CH₂I + O₂ reaction is pressure independent.

Finally, we investigated the pressure and temperature dependence of the CH₂OO related HO₂ kinetics in the same pressure and temperature ranges as above. A negative pressure dependence was observed for the HO₂ formation rate, which is consistent with the predicted pressure dependent branching ratio of the product channels of the CH₂I + O₂ reaction. Although HO₂ react with both HO₂ and IO, reaction rate with IO is much faster, making it the major HO₂ remover. Temperature dependence of the HO₂ kinetics is more complicated. There shows a slight negative temperature dependence of the HO₂ production rate. However, the reaching mechanism leading to this negative temperature dependence is still not clear.

In order to better deconvolute contributions from different reactions, we built a chemical kinetics model using the Kintecus program with the reactions listed in Table 5.1.(Ianni, 2012) Reaction rates included in the model were taken from sources including the JPL kinetics

database, the NIST chemistry database, the IUPAC database, and other literature sources.(Atkinson et al., 2004, 2007; Enami et al., 2004; Gravestock et al., 2010; Liu et al., 2014b; Masaki et al., 1995; Sander, 2011; Sehested et al., 1994; Welz et al., 2012) The reaction rate varied is the unimolecular decay rate of CH₂OO to HCO and OH. Fig. 5.9 shows the comparison between the data collected and the models. The grey shades around the model presents the error in the model. The estimated CI decay rate is $\sim 2500 \text{ s}^{-1}$. The model can describe the HO₂ and IO kinetics well without the presence of CH₂OO. But the reaction mechanism with CH₂O still presents challenges to constrain.

CONCLUSION

In order to aid into the understanding of the fate of Criegee intermediate in the atmosphere, we investigated the kinetics of HO₂ produced from the photolysis of CH₂I₂/O₂/N₂. There are two mechanisms of HO₂ formation: CH₂OO related reactions, and prompt HO₂ formation from CH₂I + O₂ without CH₂OO. The prompt HO₂ formation has no temperature or pressure dependence. There is a negative pressure dependence for the HO₂ production, which is negatively correlated with the IO production. We also observed a negative temperature dependence for the HO₂ formation, which is still not well understood. A more detailed and constrained model need to be built to calculate the temperature and pressure dependence of CH₂OO lifetime.

REFERENCES

Atkinson, R., Baulch, D.L., Cox, R.A., Crowley, J.N., Hampson, R.F., Hynes, R.G., Jenkin, M.E., Rossi, M.J. and Troe, J. (2004) Evaluated kinetic and photochemical data for atmospheric chemistry: Volume I - gas phase reactions of O-x, HOx, NOx and SOx species. *Atmos. Chem. Phys.* 4, 1461-1738.

Atkinson, R., Baulch, D.L., Cox, R.A., Crowley, J.N., Hampson, R.F., Hynes, R.G., Jenkin, M.E., Rossi, M.J. and Troe, J. (2007) Evaluated kinetic and photochemical data for atmospheric chemistry: Volume III - gas phase reactions of inorganic halogens. *Atmos. Chem. Phys.* 7, 981-1191.

Christensen, L.E., Okumura, M., Sander, S.P., Salawitch, R.J., Toon, G.C., Sen, B., Blavier, J.F. and Jucks, K.W. (2002) Kinetics of $\text{HO}_2 + \text{HO}_2 \rightarrow \text{H}_2\text{O}_2 + \text{O}_2$: Implications for stratospheric H_2O_2 . *Geophysical Research Letters* 29.

Enami, S., Ueda, J., Goto, M., Nakano, Y., Aloisio, S., Hashimoto, S. and Kawasaki, M. (2004) Formation of iodine monoxide radical from the reaction of CH_2I with O_2 . *Journal of Physical Chemistry A* 108, 6347-6350.

Fang, Y., Liu, F., Klippenstein, S.J. and Lester, M.I. (2016) Direct observation of unimolecular decay of $\text{CH}_3\text{CH}_2\text{CHOO}$ Criegee intermediates to OH radical products. *J. Chem. Phys.* 145, 9.

Fenske, J.D., Hasson, A.S., Ho, A.W. and Paulson, S.E. (2000) Measurement of Absolute Unimolecular and Bimolecular Rate Constants for CH_3CHOO Generated by the trans-2-Butene Reaction with Ozone in the Gas Phase. *J. Phys. Chem. A* 104, 9921-9932.

Gravestock, T.J., Blitz, M.A., Bloss, W.J. and Heard, D.E. (2010) A Multidimensional Study of the Reaction $\text{CH}_2\text{I} + \text{O}_2$: Products and Atmospheric Implications. *ChemPhysChem* 11, 3928-3941.

Hatakeyama, S., Kobayashi, H., Lin, Z.Y., Takagi, H. and Akimoto, H. (1986) MECHANISM FOR THE REACTION OF CH₂OO WITH SO₂. J. Phys. Chem. 90, 4131-4135.

Ianni, J.C. (2012) Kintecus Windows Version 4.55.

Kidwell, N.M., Li, H.W., Wang, X.H., Bowman, J.M. and Lester, M.I. (2016) Unimolecular dissociation dynamics of vibrationally activated CH₃CHOO Criegee intermediates to OH radical products. Nat. Chem. 8, 509-514.

Kroll, J.H., Clarke, J.S., Donahue, N.M., Anderson, J.G. and Demerjian, K.L. (2001a) Mechanism of HO_x Formation in the Gas-Phase Ozone-Alkene Reaction. 1. Direct, Pressure-Dependent Measurements of Prompt OH Yields. J. Phys. Chem. A 105, 1554-1560.

Kroll, J.H., Sahay, S.R., Anderson, J.G., Demerjian, K.L. and Donahue, N.M. (2001b) Mechanism of HO_x formation in the gas-phase ozone-alkene reaction. 2. prompt versus thermal dissociation of carbonyl oxides to form OH. J. Phys. Chem. A 105, 4446-4457.

Kurten, T., Lane, J.R., Jorgensen, S. and Kjaergaard, H.G. (2011) A Computational Study of the Oxidation of SO₂ to SO₃ by Gas-Phase Organic Oxidants. Journal of Physical Chemistry A 115, 8669-8681.

Liu, F., Beames, J.M. and Lester, M.I. (2014a) Direct production of OH radicals upon CH overtone activation of (CH₃)₂COO Criegee intermediates. J. Chem. Phys. 141, 11.

Liu, Y.D., Bayes, K.D. and Sander, S.P. (2014b) Measuring Rate Constants for Reactions of the Simplest Criegee Intermediate (CH₂OO) by Monitoring the OH Radical. Journal of Physical Chemistry A 118, 741-747.

Masaki, A., Tsunashima, S. and Washida, N. (1995) RATE CONSTANTS FOR REACTIONS OF SUBSTITUTED METHYL RADICALS (CH₂OCH₃, CH₂NH₂, CH₂I, AND CH₂CN) WITH O-2. J. Phys. Chem. 99, 13126-13131.

Noell, A.C., Alconcel, L.S., Robichaud, D.J., Okumura, M. and Sander, S.P. (2010) Near-Infrared Kinetic Spectroscopy of the HO₂ and C₂H₅O₂ Self-Reactions and Cross Reactions. *Journal of Physical Chemistry A* 114, 6983-6995.

Parker, A.E., Jain, C., Schoemaeker, C., Szriftgiser, P., Votava, O. and Fittschen, C. (2011) Simultaneous, time-resolved measurements of OH and HO₂ radicals by coupling of high repetition rate LIF and cw-CRDS techniques to a laser photolysis reactor and its application to the photolysis of H₂O₂. *Applied Physics B-Lasers and Optics* 103, 725-733.

Sander, S.P.A., J.; Barker, J. R.; Burkholder, J. B.; Friedl, R. R.; Golden, D. M.; Huie, R. E.; Kolb, C. E.; Kurylo, M. J.; Moortgat, G. K.; Orkin, V. L.; Wine, P. H. (2011) JPL Publication 10-6 Jet Propulsion Laboratory, Pasadena.

Sehested, J., Ellermann, T. and Nielsen, O.J. (1994) A SPECTROKINETIC STUDY OF CH₂I AND CH₂IO₂ RADICALS. *Int. J. Chem. Kinet.* 26, 259-272.

Thiebaud, J., Crunaire, S. and Fittschen, C. (2007) Measurements of line strengths in the 2 ν₁ band of the HO₂ radical using laser photolysis/continuous wave cavity ring-down spectroscopy (cw-CRDS). *Journal of Physical Chemistry A* 111, 6959-6966.

Welz, O., Savee, J.D., Osborn, D.L., Vasu, S.S., Percival, C.J., Shallcross, D.E. and Taatjes, C.A. (2012) Direct Kinetic Measurements of Criegee Intermediate (CH₂OO) Formed by Reaction of CH₂I with O₂. *Science* 335, 204-207.

FIGURES AND TABLES

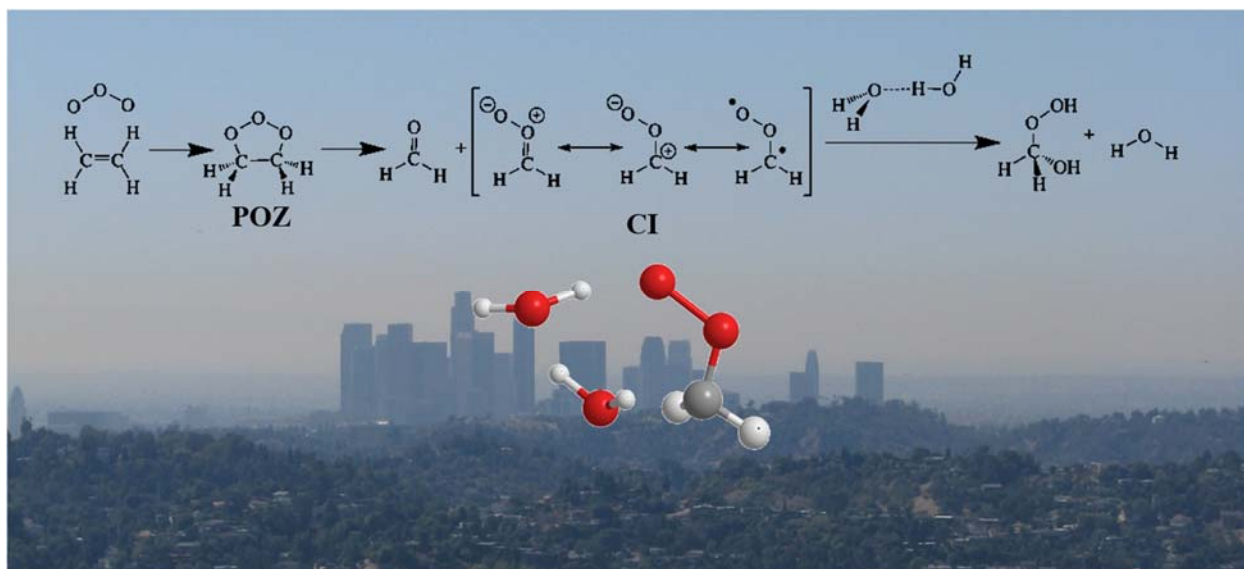


Figure. 5. 1. Schematic of the reaction mechanism of the ozonolysis reaction mechanism of the smallest alkene.

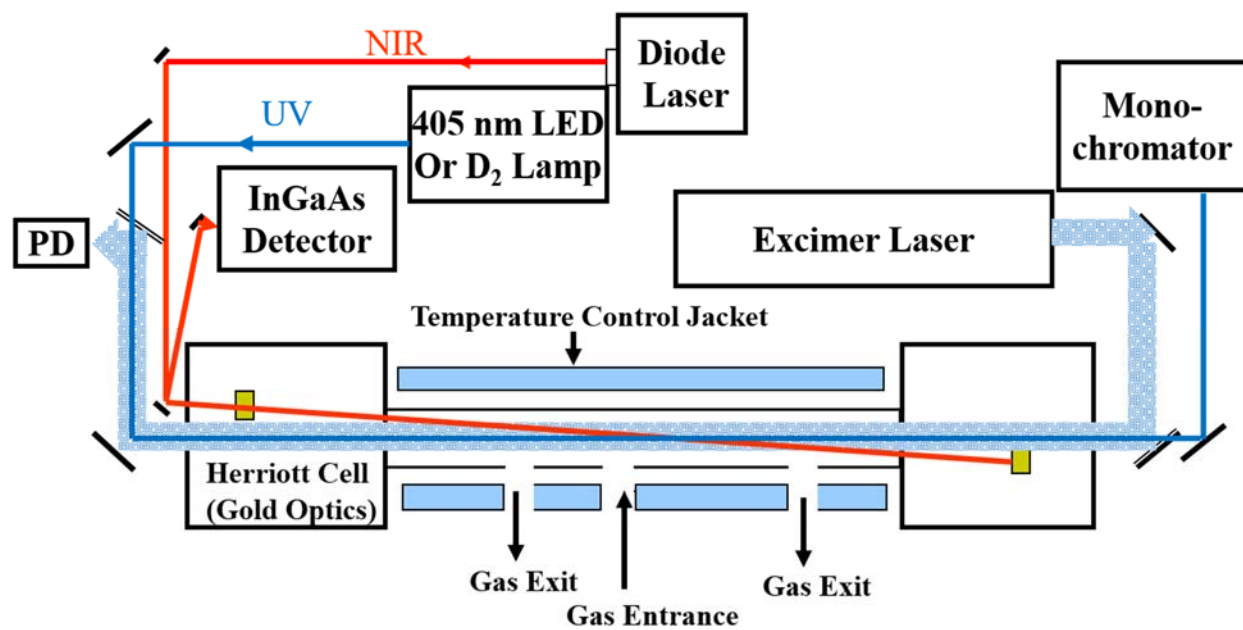


Figure 5. 2. Schematic of the infrared kinetics spectroscopy (IRKS) apparatus showing the three light sources.

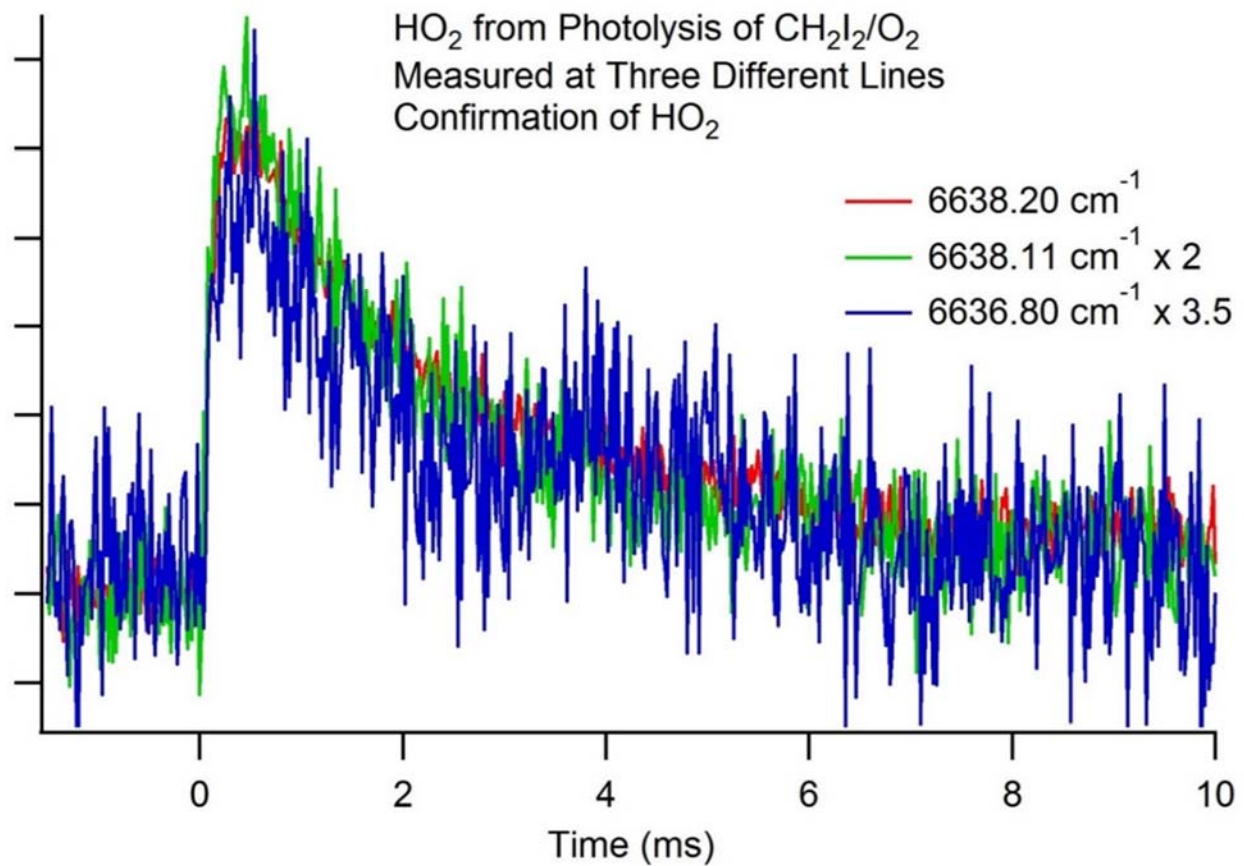


Figure. 5. 3. HO₂ was observed from the CH₂I₂/O₂ system. The product was confirmed to be HO₂ by measurement at different HO₂ transitions.

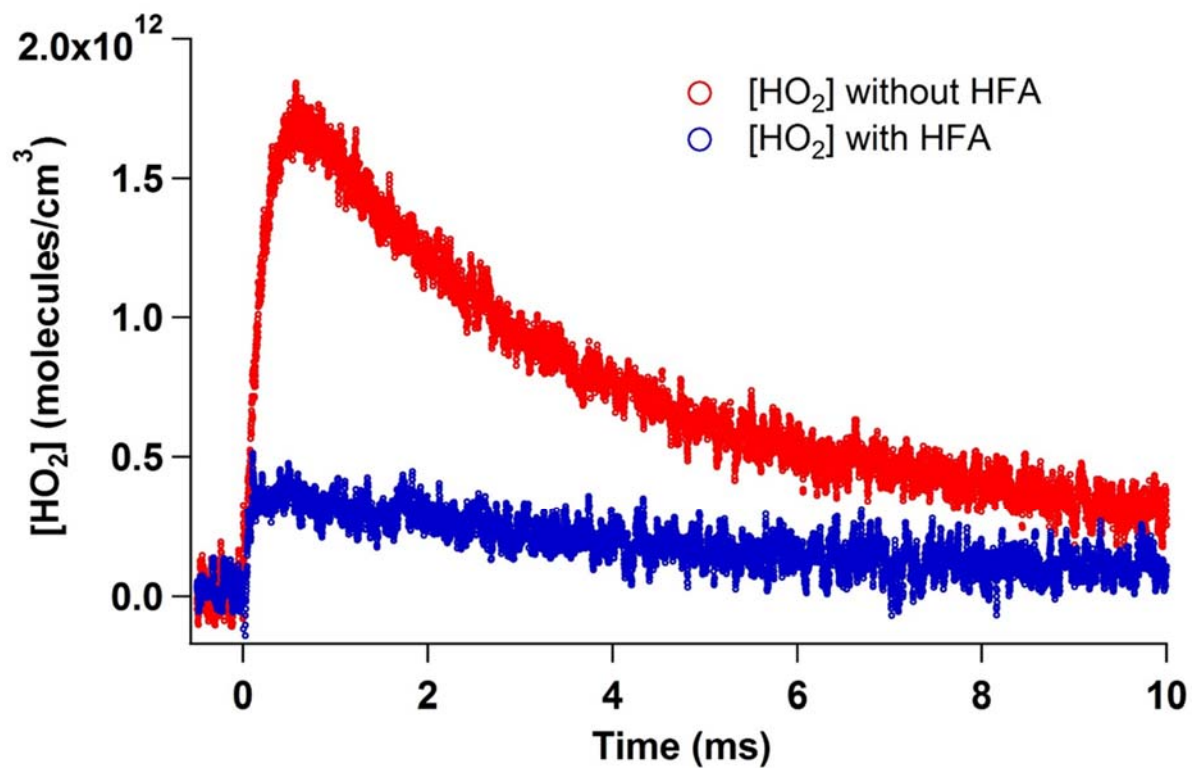


Figure 5. 4. Hexafluoroacetone (HFA) was added as a Criegee scavenger to study reaction kinetics with or without CI. It was found that most of the HO_2 was made from CI, while there is a fast HO_2 formation mechanism unrelated to CI, most likely from direct $\text{CH}_2\text{I} + \text{O}_2$ reaction.

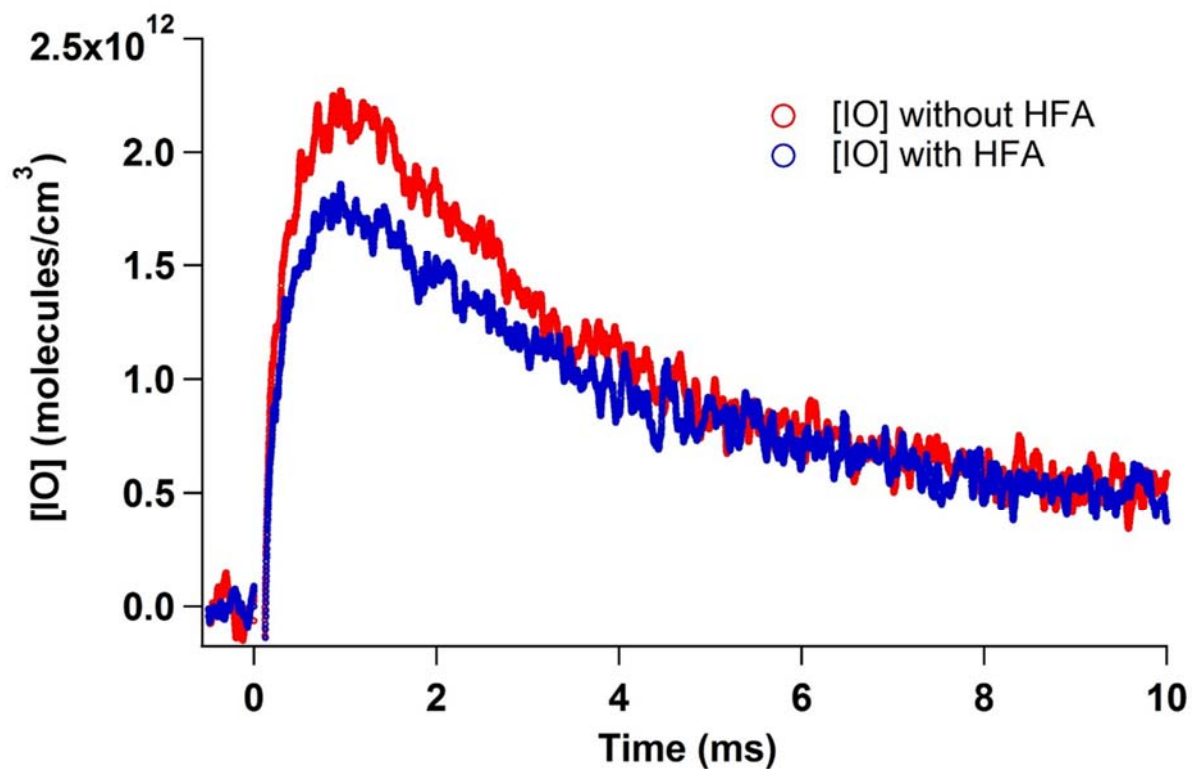


Figure 5.5. We also monitored IO simultaneously with HO₂. IO was made mainly from CH₂IOO + I. The rate for this reaction was about $4 \times 10^{-11} \text{ cm}^3 \text{ molecules}^{-1} \text{ s}^{-1}$. From the experiments with HFA, we found that some of the IO came from the reaction between CH₂OO and I.

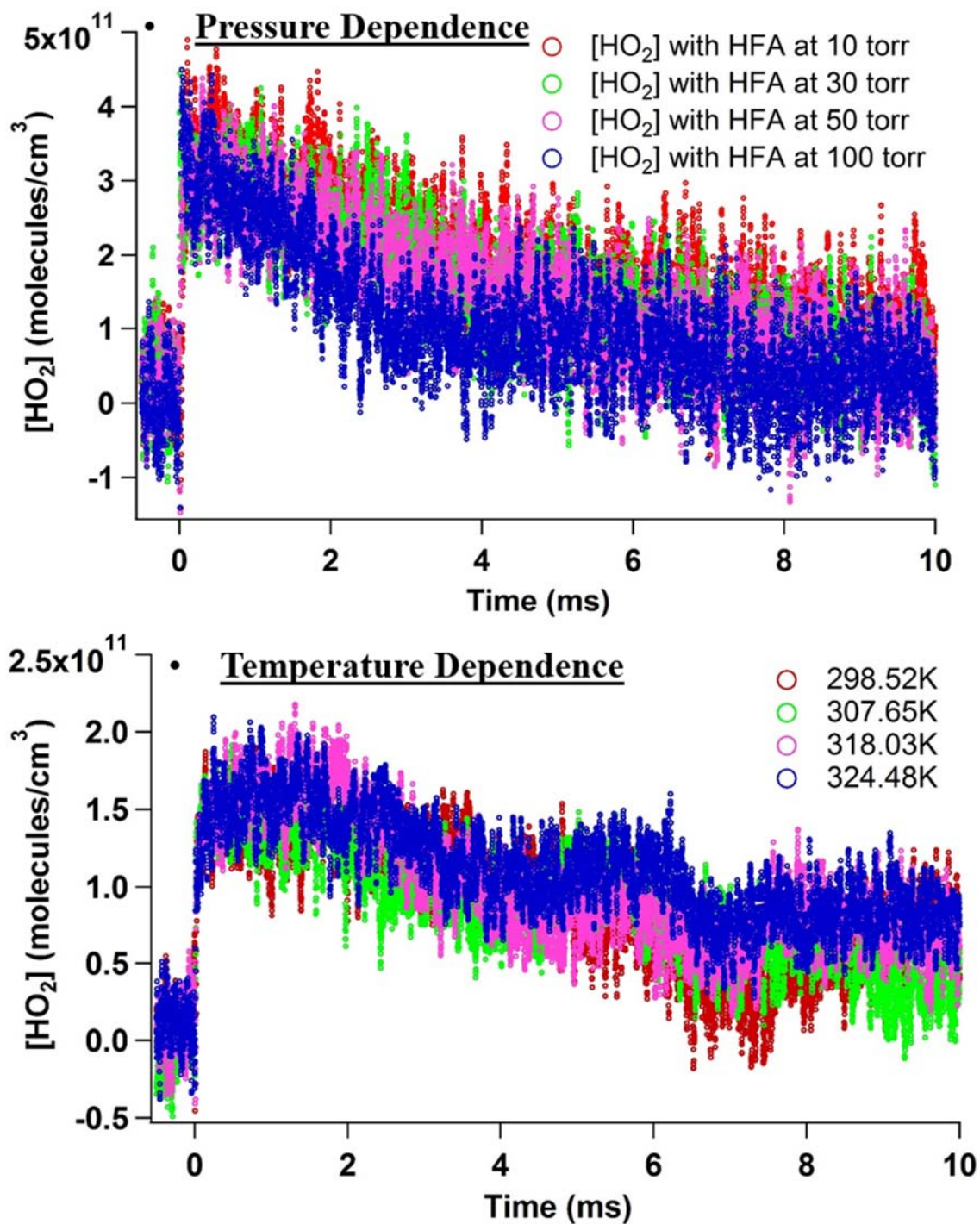


Figure 5. 6. Pressure and temperature dependent studies were done for systems with or without HFA. The HO₂ mechanisms without CH₂OO has shown no pressure or temperature dependence.

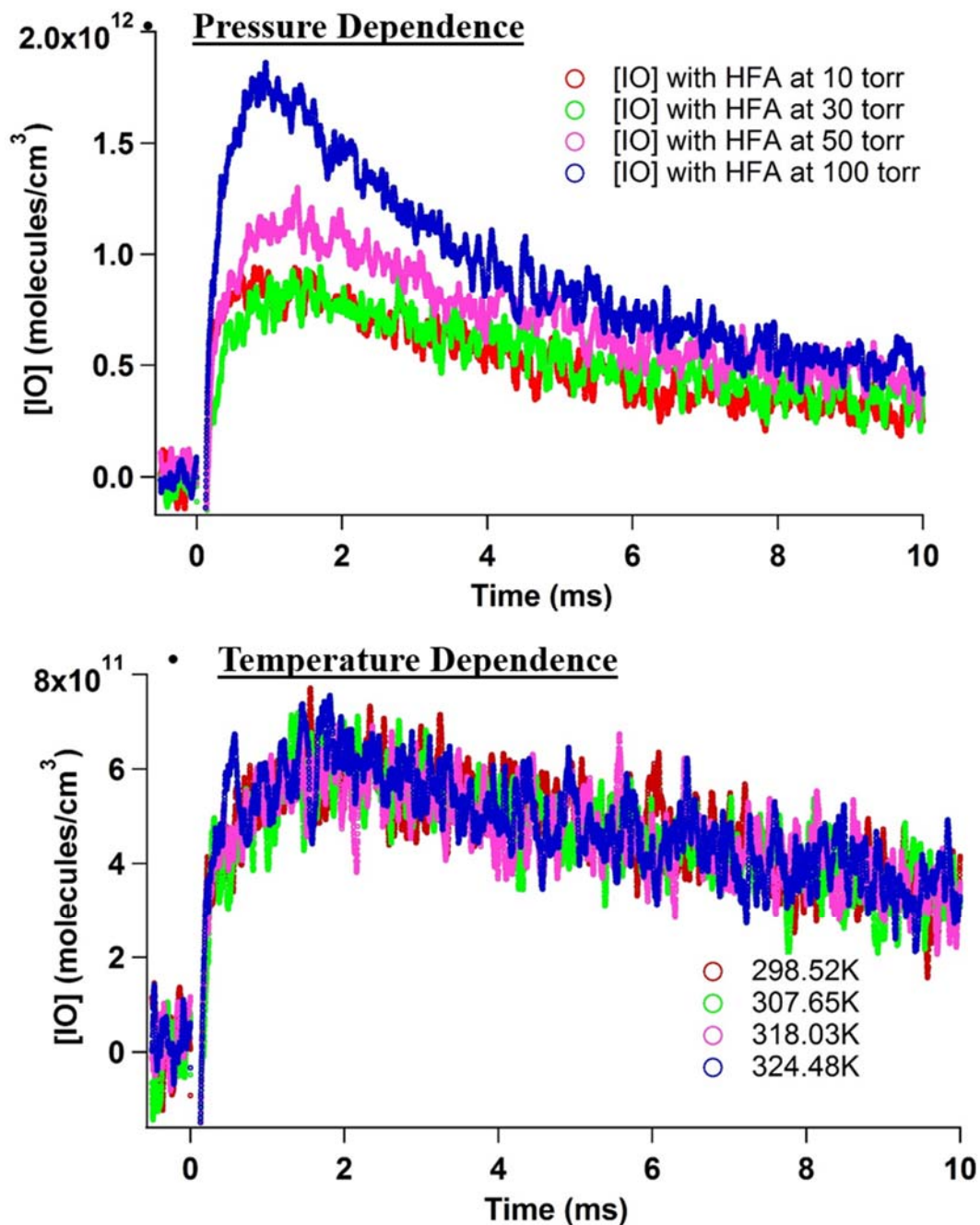


Figure 5. 7. Pressure and temperature dependence of the IO profile was also measured. There was no temperature dependence for the IO kinetics. There is a positive dependence for the IO production, indicating a negative pressure dependence for CH₂OO production, since the overall CH₂I + O₂ reaction is pressure independent.

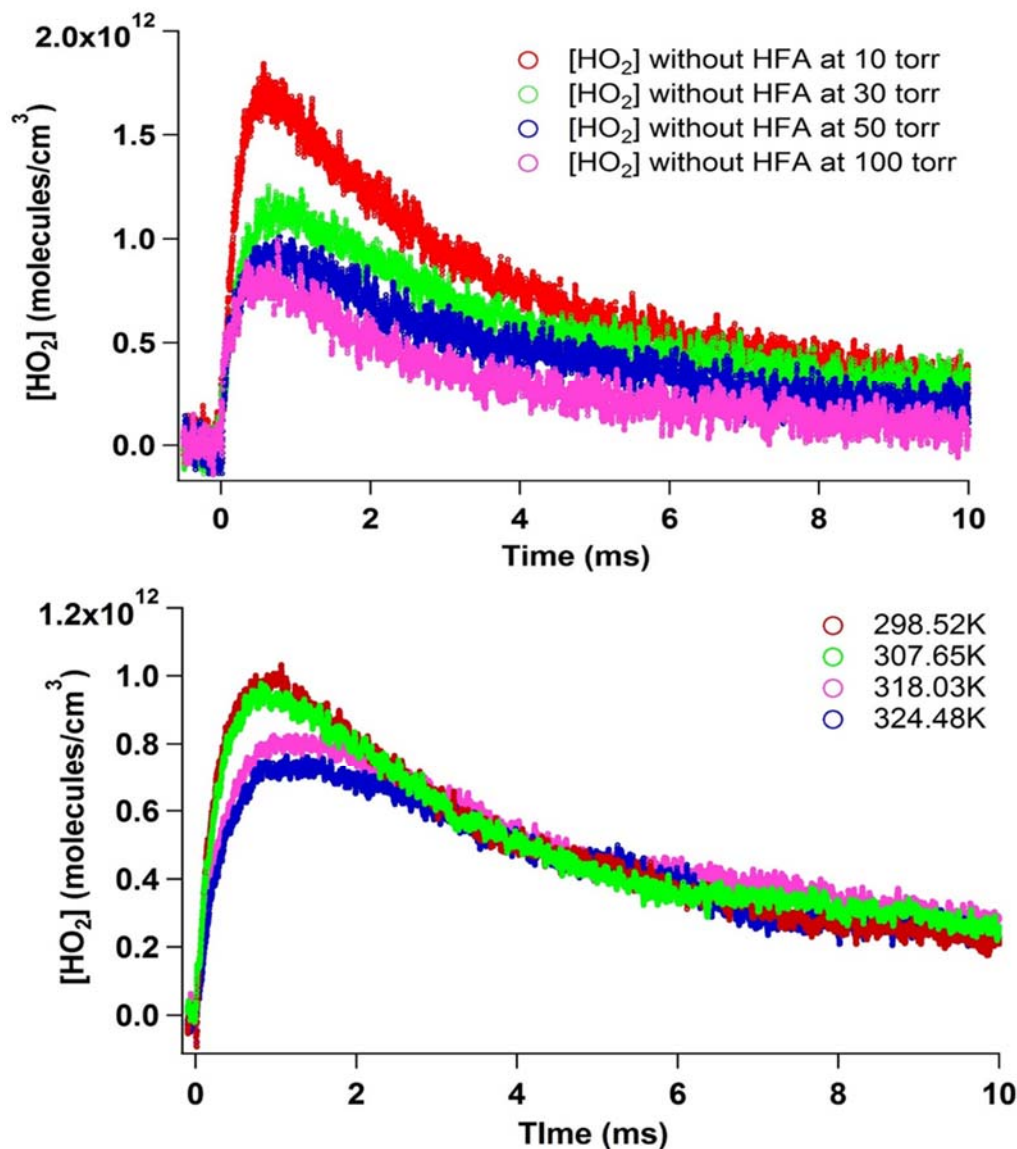
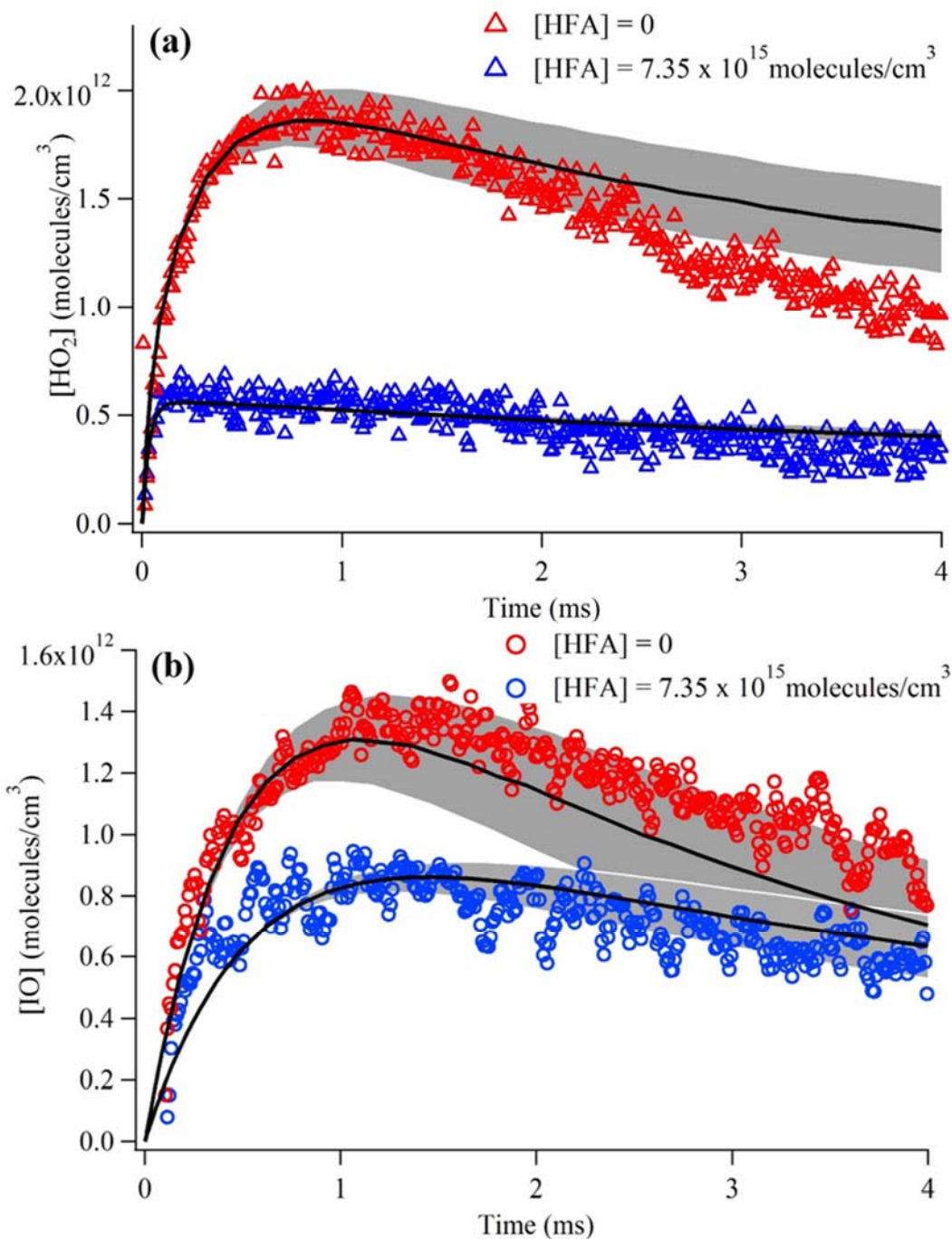


Figure 5. 8. Upper panel: Pressure dependence of HO₂ kinetics was measured between 10 and 100 torr. There is a negative pressure dependence in the HO₂ production, due to the branching ratio of CH₂I + O₂. The depletion of HO₂ is mainly due to the reaction with IO. The estimated CI decay rate was between 2000 and 3000 s⁻¹. Lower panel: Temperature dependence of the HO₂ kinetics was measured between 298 K and 325 K. There shows a slight negative temperature dependence. The reaction mechanism leading to this negative temperature dependence is still not clear.



- **Figure 5.9.** A full kinetics model was built to describe this chemical system to obtain CH₂OO decay rate as a function of pressure and temperature. The model can describe the HO₂ and IO kinetics well without the presence of CH₂OO. But the reaction mechanism with CH₂OO still presents challenges to constrain.

Table. 5. 1. Reactions included in the Kintecus model.

# A	T ^m	Ea	Reaction	Comments
#CH2I+O2				
4.00E-13	0	0	CH2I+O2==>HCHO+IO	Enami et al. 2004
1.60E-13	0	0	CH2I+O2==>CH2IO2	Masaki et al. 1995
9.00E-13	0	0	CH2I+O2==>I+CH2O2	Welz et al
#CH2O2 Reactions				
1.00E+03	0	0	CH2O2==>HCO+OH	Liu et al
5.20E-12	0	0	HCO+O2==>HO2+CO	JPL
3.33E-11	0	0	CH2O2+HFA==>CH2O2HFA	Liu et al
#Iodine Reactions				
1.23E-15	0	0	I+I==>I2	NIST Termolec
1.50E-11	0	1090	I+HO2==>HI+O2	JPL
1.80E-10	0	0	OH+I2==>HOI+I	JPL
3.00E-11	0	0	OH+HI==>H2O+I	JPL
8.40E-11	0	0	IO+HO2==>HOI+O2	JPL
4.00E-12	0	0	IO+IO==>I2+O2	JPL

2.40E-11	0	0	IO+IO==>OIO+I	JPL
5.20E-11	0	0	IO+IO==>I2O2	JPL
#HOx Reactions				
2.00E-12	0	0	OH+OH==>H2O2	JPL
1.10E-10	0	0	OH+HO2==>H2O+O2	JPL
8.50E-12	0	0	OH+HCHO==>H2O+HCO	JPL
1.80E-12	0	0	OH+H2O2==>HO2+H2O	JPL
4.40E-12	0	0	OH+CH2I2==>CHI2+H2O	Liu et al
1.40E-12	0	0	HO2+HO2==>H2O2+O2	JPL
7.90E-14	0	0	HO2+HCHO==>HOCH2O2	IUPAC
1.50E+02	0	0	HOCH2O2==>HO2+HCHO	IUPAC
1.00E-27	0	0	HO2+CO==>OH+CO2	NIST
#CH2I Reactions				
1.33E-10	0	0	I+CH2I==>CH2I2	NIST
4.00E-11	0	0	CH2I+CH2I==>CH2ICH2I	Sehested et al, 1994

2.00E-11	0	0	I+CH2IO2==>IO+HCHO+I	Gravestock et al, 2010
1.20E-10	0	0	CH2IO2+CH2IO2==>HCHO+HCHO+I+I+O2	Gravestock et al, 2010
3.32E-10	0	0	CH2I+I2==>CH2I2+I	NIST
#0.000000000468	0	7.57	CH2I2+I==>I2+CH2I	NIST
#Gussed Reactions				
1.00E-11	0	0	HO2+CH2O2==>X	Estimate
1.00E-13	0	0	HO2+CH2I2==>Y	Estimate